

https://dspace.org/

Development of a test facility for the study of cold gas dynamic spraying: Rig Characterisation.

Masitise, Martin Nare.

2011-10-12
http://hdl.handle.net/10539/10538

Downloaded from a DSpace repository. https://dspace.org/

Development of a test facility for the study of cold gas dynamic spraying:
Rig Characterisation

Martin Nare Masitise

A dissertation submitted to the Faculty of Engineering and the Built Environment, University of the Witwatersrand, Johannesburg, in partial fulfilment of the requirements for the degree of Master of Science in Engineering.

Johannesburg, 2011

Declaration

I, Martin Nare Masitise, declare that this research report is my own work. It is being submitted for the degree of Masters of Science in Mechanical Engineering in the University of the Witwatersrand, Johannesburg. It has not been submitted before for any degree or examination at this or any other University.

.....

.....day of....., 2011

Abstract

In this dissertation a facility for the study of Shock Wave Induced Cold Gas Spraying (SWICGS) is investigated. The objective of the study was to design, construct and test a shock tube rig that will be used to accelerate gas jets to velocities required for deposition in SWICGS applications. The testing of the rig involved using helium and air as gas drivers, and testing for different diaphragm configurations on the rig for best performance.

To understand the problem better a literature review on several aspects surrounding the field of SWICGS was conducted. This involved aspects such as particle critical velocity, deposition efficiency, shock wave production and several other topics. Based on the compiled literature, three conceptual rig designs were generated. Concept B was selected to be developed further into detailed design. The main contributing factors in the decision making with regards to the rig design were the safety of the design, the provision of undisturbed flow in the tube and ease of manufacture.

The final rig has a shock tube with an internal diameter of 5mm. The pressure reservoir of the rig is 0.377 litres, and the total length of the rig is 2 meters, with a safety factor of at least 10 for all components. The rig makes use of solenoid valves to work as diaphragms; the valves have an opening time of 100*ms* and a closing time of 100*ms*. The opening and closing of the valves is controlled by a programmed Moeller controller.

Significantly high jet velocities were obtained at room temperatures using the designed rig, with air as the gas driver jet velocities of up to 516.35 *m/s* were achieved and with helium as the gas driver jet velocities of up to 876.92 *m/s* were achieved within the tested range of 10 to 50 bars reservoir pressure. These high velocities can be achieved at a wave generation frequency of 5 Hz. The rig can generate high velocity jets even at higher frequencies of up to 20 Hz. The single valve arrangement showed to be generally performing better than the double valve arrangement within the tested range and conditions.

Acknowledgements

I would like to thank my supervisors, Dr. Ionel Botef and Professor Beric William Skews for their guidance and encouragement while I conducted the research presented in this dissertation.

I express my appreciation to Mr. Edwin Sanyangare for the meaningful discussions and his contribution to my knowledge of the Cold Gas Dynamic Spraying subject.

I would like to extend my deepest thanks to Miss Kgodiso Mokonyane for her continuous support at home while the research was conducted.

Finally, I would like to thank the workshop stuff, Mr. Smit, Mr. Muller and Mr. Cooper for their assistance in the construction of the test rig that was used in this research.

Contents

DECLARATION ..... **II**

ABSTRACT ..... **III**

ACKNOWLEDGEMENTS ..... **IV**

CHAPTER 1 INTRODUCTION **1**

1.1 BACKGROUND 1
1.2 MOTIVATION 2
1.3 OBJECTIVES 4
1.4 LITERATURE REVIEW 5
1.4.1 Cold Gas Spraying *5*
1.4.2 Shock Tubes and Gas Dynamic Principles *13*
1.4.3 KASIMIR Simulation Software *25*
1.4.4 Solenoid Valves *26*
1.4.5 Structural Analysis *27*

CHAPTER 2 SHOCK TUBE RIG DESIGN **29**

2.1 PRODUCT REQUIREMENTS SPECIFICATION 29
2.1.1 Requirements *29*
2.1.2 Constraints *29*
2.1.3 Criteria *30*
2.2 FUNCTIONAL ANALYSIS 30
2.2.1 The Transducer Ports: *30*
2.2.2 Valve Selection: *30*
2.2.3 Reservoir Construction: *30*
2.2.4 Tube Dimensions: *30*
2.3 CONCEPTS CONSIDERED 31
2.3.1 Concept A *31*
2.3.2 Concept B *32*
2.3.3 Concept C *33*
2.4 DECISION MATRIX 34
2.5 DETAILED DESIGN 35
2.5.1 Tube Length Decision *35*
2.5.2 Reservoir Size Decision *35*
2.5.3 Transducer Size and Attachment *36*
2.5.4 Stagnation Pressure Measurement *37*
2.5.5 Valve Selection *37*
2.5.6 Structural Analysis *37*
2.5.7 Control Circuit *39*
2.5.8 Programming *40*
2.6 DESIGN DESCRIPTION 43
2.7 POWDER FEEDER DEVELOPMENT 44
2.8 FINAL DESIGN 45
2.9 SHOCK TUBE RIG SPECIFICATIONS 46

CHAPTER 3 APPARATUS **47**

3.1 CONSUMABLES 47
3.1.1 Pressure Cylinder *47*
3.2 HARDWARE 47
3.2.1 Pressure Transducers *47*
3.2.2 Data Acquisition System *47*
3.2.3 Solenoid Valves *48*
3.2.4 Controller *48*

3.2.5 Pressure Transducer Identification ... *49*
3.2.6 Rig Assembly ... *50*
3.3 SOFTWARE ... 50

CHAPTER 4 METHODOLOGY ... 51

4.1 INVESTIGATION METHODOLOGY ... 51
4.1.1 Double Valve Arrangement: shock wave strength tests ... *51*
4.1.2 Single Valve Arrangement: shock wave strength tests ... *51*
4.1.3 Single Valve Arrangement: variable opening frequency test ... *51*
4.1.4 Single Valve Arrangement: gas pre-heating test ... *52*
4.1.5 Double Valve Arrangement: gas pre-heating ... *52*
4.2 PROCEDURE ... 53
4.2.1 Experimental Procedure ... *53*
4.2.2 Kasimir Simulations ... *54*
4.3 PRECAUTIONS ... 55

CHAPTER 5 RESULTS ... 56

5.1 SAMPLE CALCULATIONS AND PRESSURE MEASUREMENT ... 56
5.1.1 Theoretical Calculation of the Shock Strength: double valve arrangement ... *56*
5.1.2 Technique of Measuring the Shock Strength from Experiments ... *62*
5.1.3 Flow Velocity Behind the Compression Wave ... *64*
5.1.4 Impact Velocity Sample Calculation ... *65*
5.2 PLOTS OF RESULTS ... 66
5.2.1 Single Valve Arrangement ... *66*
5.2.2 Double Valve Arrangement ... *67*
5.2.3 Multiple Valve Opening Frequency ... *69*
5.2.4 Flow Substrate Impact Velocity ... *69*
5.2.5 Flow Pressure Pulses ... *70*
5.2.6 Double Valve Time Delay Diagnosis ... *74*
5.2.7 Gas Pre-heating ... *76*

CHAPTER 6 DISCUSSION ... 77

6.1 SHOCK VELOCITY AND VELOCITY OF THE GAS BEHIND THE SHOCK ... 77
6.1.1 Single Valve Arrangements ... *77*
6.1.2 Double Valve Arrangement ... *78*
6.2 MULTIPLE VALVE OPENING FREQUENCY TESTS ... 78
6.2.1 Single Valve Arrangement ... *78*
6.3 FLOW SUBSTRATE IMPACT VELOCITY: SINGLE AND DOUBLE ... 79
6.4 TUBE DOWNSTREAM STATIC PRESSURE ... 80
6.5 FLOW PRESSURE PULSES ... 81
6.6 GAS PRE-HEAT TEMPERATURE ... 82
6.7 PROCESS PHYSICS ... 83
6.8 PARTICLE TRAJECTORY ... 84
6.9 RIG PERFORMANCE ... 85

CHAPTER 7 CONCLUSIONS AND RECOMMENDATIONS ... 86

7.1 CONCLUSIONS ... 86
7.2 RECOMMENDATIONS ... 87

REFERENCE LIST ... 88

APPENDIX A ... 91

ENGINEERING DRAWINGS ... 91

APPENDIX B ... 117

7.3 TABLES OF RESULTS ... 117

7.3.1 Compression Wave and Flow Behind the Compression Wave Velocities 117
7.3.2 Change in Jet Impact Velocity with Change in Pressure 121
7.3.3 Impact Velocity Change with Change in Pressure and Frequency 122
7.3.4 Change in Down Stream Static Pressure with Change in Reservoir Pressure 124
7.3.5 Driver Gas Pre-heating 125

APPENDIX C 127

COMPONENTS SPECIFICATIONS 127

APPENDIX D 132

DRAG COEFFICIENTS FOR DIFFERENT REYNOLDS NUMBERS (MORSI ET AL, 1972) 132

APPENDIX E 133

SOLENOID VALVE TYPES 133

APPENDIX F 136

WAVE DIAGRAMS FROM KASIMIR SIMULATIONS 136

APPENDIX G 141

VALIDATION OF THE SHOCK TUBE LENGTH SELECTION 141

List of Figures

Figure 1: Schematic diagram of a Cold Gas Dynamic Spraying process 5
Figure 2: Schematic diagram of a Shock Wave Induced Cold Gas Spraying process 5
Figure 3: Deformation of aluminum particles with different impact velocities on a polished copper substrate (Papyrin, 2007). 8
Figure 4: Effect of the particle size, the feed-powder material and the carrier gas of the particle critical impact velocity for adhesion (Grugicic et al. 2003). 9
Figure 5: Deposition efficiency of aluminum, copper, and nickel powders sprayed on copper substrate versus the air jet stagnation temperature (Papyrin, 2007) 10
Figure 6: Deposition efficiency for aluminum, copper, and nickel powders accelerated by an air helium mixture (1-3) and by heating air (4-6) versus particle velocity (Papyrin, 2007) 11
Figure 7: Single diaphragm shock tube schematic 14
Figure 8: Pressure plot before and immediately after diaphragm rupture (Wright, 1961) 14
Figure 9: Representation of the instantaneous gas velocity inside the expansion chamber just before the shock wave exits the tube 15
Figure 10: Representation of the instantaneous gas temperature inside the expansion chamber just before the shock wave exits the..... 15
Figure 11: Multi diaphragm shock tube arrangement..... 16
Figure 12: Firing phase schematic of one pulse cycle 18
Figure 13: Filling phase schematic of one pulse cycle 19
Figure 14: An ideal shock wave diagram for a double valve arrangement showing the primary, reflected and secondary shock waves. 20
Figure 15: Moving primary normal shock wave between region one and region two 21
Figure 16: Reflected shock presented as a stationary shock..... 22
Figure 17: Schematic of a supersonic impinging jet flow field (Grugicic et al, 2003) 24
Figure 18: Pressure transducer orientation for different flow directions (Tropea et al, 2007) 25
Figure 19: X-t-diagram of waves in a shock tube calculated with KASIMIR 25
Figure 20: Concept A– Thick metal bar 31
Figure 21: Concept B – Transducer stands..... 32
Figure 22: Concept C – T-piece connectors 33
Figure 23: Pressure reservoir assembly 36
Figure 24: Transducer stand after tube insertion and welding..... 36
Figure 25: Stagnation pressure transducer stand 37
Figure 26: Side plate and rods pressure loading..... 38
Figure 27: Reservoir radial pressure loading..... 39
Figure 28: Valve control circuit diagram..... 40
Figure 29: Single valve arrangement program circuit diagram 41
Figure 30: Double valve arrangement program circuit diagram..... 42
Figure 31: Double valve arrangement setup..... 43
Figure 32: Single valve arrangement setup..... 43
Figure 33: Powder feeder design 44
Figure 34: Final design assembly drawing 45
Figure 35: Data acquisition system..... 47
Figure 36: Solenoid valves 48
Figure 37: Valves control circuit 48

Figure 38: Transducer Identification 49
Figure 39: Shock tube rig components assembly 50
Figure 40: Kasimir simulation tube specifications screen with two sections (1 and2)..... 54
Figure 41: Pressure history for transducers B and C, single valve arrangement at 5Hz and 30 bar pressure supply 63
Figure 42: Enlargement of a single cycle from figure 41. 63
Figure 43: Compression wave velocity change with the change in reservoir pressure: Single valve..... 66
Figure 44: Gas flow velocity behind the compression wave vs. reservoir pressure..... 67
Figure 45: Compression wave velocity vs. reservoir pressure: Double valve..... 68
Figure 46: Gas flow velocity behind the compression wave change with change in resevoir pressure: Double valve..... 68
Figure 47: Multiple valve opening frequency: 5Hz, 10Hz and 20Hz..... 69
Figure 48: Flow impact velocity with change in pressure..... 70
Figure 49: Pressure variation with change in time with air as the driver gas: 5Hz 71
Figure 50: Pressure variation with change in time with helium as the driver gas: 5Hz 71
Figure 51: Pressure variation with change in time with air as the driver gas: 10Hz 72
Figure 52: Pressure variation with change in time with helium as the driver gas: 10Hz 72
Figure 53: Pressure variation with change in time with air as the driver gas: 20Hz 73
Figure 54: Pressure variation with change in time with helium as the driver gas: 20Hz 73
Figure 55: Pressure traces with 100*ms* time delay in the shock generator: 5 bar reservoir..... 74
Figure 56: Pressure traces with 150*ms* time delay in the shock generator: 5 bar reservoir..... 75
Figure 57: Pressure traces with 200*ms* time delay in the shock generator: 5 bar reservoir..... 75
Figure 58: Pre-heated gas flow velocity: single valve arrangement..... 76
Figure 59: Pre-heated gas flow velocity: double valve arrangement..... 76
Figure 60: Air and helium static pressure pulses at 5Hz 81
Figure 61: Sectioned view of the Tube pinch solenoid valve..... 133
Figure 62: Sectioned view of the diaphragm solenoid valve..... 134
Figure 63: Sectioned view of the direct operated solenoid valve..... 134
Figure 64: Sectioned view of the lever type solenoid valve..... 135
Figure 65: 10 bar reservoir pressure with air as the gas driver..... 136
Figure 66: 10 bar reservoir pressure with helium as the gas driver..... 136
Figure 67: 20 bar reservoir pressure with air as the gas driver..... 137
Figure 68: 20 bar reservoir pressure with helium as the gas driver..... 137
Figure 69: 30 bar reservoir pressure with air as the gas driver..... 138
Figure 70: 30 bar reservoir pressure with air as the gas driver..... 138
Figure 71: 40 bar reservoir pressure with air as the gas driver..... 139
Figure 72: 40 bar reservoir pressure with helium as the gas driver..... 139
Figure 73: 50 bar reservoir pressure with air as the gas driver..... 140
Figure 74: 50 bar reservoir pressure with helium as the gas driver..... 140
Figure 75: Case A Shock wave diagram..... 142
Figure 76: Case B Shock wave diagram..... 143
Figure 77: Case C Shock wave diagram..... 143
Figure 78: Case D Shock wave diagram..... 143
Figure 79: Case E Shock wave diagram 144
Figure 80: Case F Shock wave diagram 144

List of Tables

Table 1: Values of Coefficient Y for $t \succ D/6$ 28
Table 2: Concepts comparizon and decision making 34
Table 3: Iterative process to find the conditions of the reflected shock 59
Table 4: Compression wave velocity with change in reservoir pressure: Air and He..... 117
Table 5: Flow velocity behind the compression wave with change in reservoir pressure: air ... 118
Table 6: Flow velocity behind the compression wave with change in reservoir pressure: He... 118
Table 7: Kasimir Flow Simulations for the shock velocity and flow velocity behind the shock: Air and He 118
Table 8: Compression wave velocity change with change in reservoir pressure: Air and He ... 119
Table 9: Flow velocity behind the shock change with change in reservoir pressure: air 119
Table 10: Flow velocity change with change in reservoir pressure: He..... 120
Table 11: Kasimir Flow Simulations for the shock velocity and flow velocity behind the shock: Air and He 120
Table 12: Flow velocity with change in pressure and frequency 121
Table 13: Flow impact velocity on substrate downstream of gun exit: Air..... 121
Table 14: Flow impact velocity on substrate downstream of gun exit: He 122
Table 15: Flow impact velocity on substrate downstream of gun exit: Air..... 122
Table 16: Flow impact velocity on substrate downstream of gun exit: He 122
Table 17: Flow impact velocity on substrate downstream of gun exit pulsating at 10 Hz: Air 123
Table 18: Flow impact velocity on substrate downstream of gun exit pulsating at 10 Hz: He .. 123
Table 19: Flow impact velocity on substrate downstream of gun exit pulsating at 20 Hz: He .. 123
Table 20: Summarized impact velocities table for the 5, 10 and 20 Hz frequencies..... 124
Table 21: Transducer B static pressure traces 124
Table 22: Transducer C static pressure traces 125
Table 23: Gas pre-heat velocities for the single valve arrangement..... 125
Table 24: Gas pre-heat velocities for the double valve arrangement 126
Table 25: Solenoid valve specifications 127
Table 26: Helium cylinder specifications 129
Table 27: Dry-air cylinder specifications 129
Table 28: PCB Pressure transducer – Model 113A21 129
Table 29: PCB Pressure transducer – Model 113A23 130
Table 30: PCB Pressure transducer – Model 113A24 130
Table 31: Moeller controller specifications 131
Table 32: Simulation results summary 142

List of Definitions and Abbreviations

SWICGS:	Shock Wave Induced Cold Gas Spraying.
CGDS:	Cold Gas Dynamic Spraying.
ASME:	American Society of Mechanical Engineers.
KASIMIR:	Is a German abbreviation for Shock tube simulation on a computer.
De Laval Nozzle:	A nozzle with a converging section followed by a diverging section also known as the converging/diverging nozzle.
Shock Tube:	A long tube usually divided into two parts by a diaphragm; the volume on one side of the diaphragm constitutes a compressed gas region and the other side is typically at atmospheric conditions.
Compression Chamber:	High pressure region in the shock tube
Expansion Chamber:	A low pressure region in the shock tube, usually at atmospheric conditions.
Diaphragm:	A layer separating the compression chamber from the expansion chamber. The layer will have to be first broken for compression waves to be generated.
Deposition:	It is the adhesion of fast moving powder particle onto a substrate to create a strong bond when they impact onto it.
Substrate Erosion:	It is the damaging of a substrate by fast moving powder particles when they impact onto it, in this case particles bounce off instead of adhering.
Critical Velocity:	The particle velocity above which substrate erosion stops to occur and coat formation begins.
Normal Shock Wave:	Is a strong compression wave with very large amplitude, propagating at a supersonic velocity in the direction perpendicular (at 90°) to the shock medium's flow direction
Bow Shock Wave:	A shock wave which occurs upstream of the front of a blunt object when the upstream velocity is supersonic.

Nomenclature

C_d : is the drag coefficient [Dimensionless]

ρ : is the air density [kg/m^3]

v_p : is the particle velocity [m/s]

μ : is the absolute viscosity coefficient of the gas [$Pa{\cdot}s$]

a : is the speed of sound at a particular temperature [m/s]

M : is the Mach number [Dimensionless]

σ_y : is the yield strength [Pa]

V_S : is the shock velocity [m/s]

d_p : is the particle diameter [m]

d_p : is the pipe internal pressure loading [Pa]

D: is the tube outer diameter [m]

t : is the tube thickness [m]

γ_1 : is the specific heat ratio [Dimensionless]

R_e : Relative Reynolds number [Dimensionless]

m_p : Particle mass [g]

Chapter 1 Introduction

1.1 Background

In this dissertation a test facility for the study of Cold Gas Dynamic Spraying (CGDS) is investigated. CGDS is a process of applying coatings by exposing a metallic or dielectric substrate to a high velocity (300-1200 m/s) jet of small (1-50 μm) particles accelerated by a supersonic jet of compressed gas (Papyrin, 2007). In the cold gas dynamic spraying process, powder particles are accelerated by the supersonic gas jet at a temperature that is always lower than the melting point of the material. This means that coat formation on the substrate occurs with powder particles being in a solid state, as opposed to thermal spraying techniques where particles are melted.

Gold gas dynamic spraying technology was first discovered in the early 1980s by Dr. Anatolii Papyrin and his colleagues at the Institute of Theoretical and Applied Mechanics of the Siberian Branch of the Russian Academy of Science (Papyrin, 2007). The discovery of the technology was made while studying models subjected to a supersonic two-phase flow (gas + solid particles) in a wind tunnel (Alkhimov et al, 1990). The research team worked on the design of high speed 're-entry vehicles' and during the experiments, using a supersonic wind tunnel with metal tracer particles, it was observed that sometimes the particles build up a coating on the target instead of eroding it (Steenkiste et al, 2003).

Outside of Russia, the cold spray process was presented first in the United States by Dr. Papyrin in 1994. At the present time, a wide spectrum of research is being conducted at several research centres around the world, and a number of publications have been made on the subject to date. A patent for the CGDS technology was issued in the United States in 1994 and Europe in 1995.

A new cold spraying technique (shock wave induced cold gas spraying; SWICGS) was developed at the University of Ottawa, Canada in 2001. SWICGS process is similar to the CGDS process, in that feedstock powder particles are accelerated to high impact velocities in both processes, and the intermediate temperatures are below the melting temperatures of

the feed stock (Jodoin et al, 2007). The fundamental difference between the two processes is that the CGDS process makes use of a nozzle (DeLaval nozzle) to accelerate feedstock particle flow, whereas the SWICGS process uses compression waves (which coalesce to form shock waves) generated in a shock tube set up (Jodoin et al, 2007).

1.2 Motivation

In the CGDS technique, the feedstock particles are accelerated by a supersonic gas flow beyond a material dependant critical velocity (Alkhimov et al, 1994). This critical velocity depends not only on the type of spraying and substrate material but also on the particle size and temperature upon impact (Schmidt et al, 2006). Studies have revealed that failure to accelerate the feed stock particles beyond the critical velocity results in substrate erosion instead of coating formation (Schmidt et al, 2006). In order to improve the coating quality and to also extend the range at which the CGDS technique can be used, it is desirable to increase the particles impact velocity (Luo et al, 2009).

In SWICGS, the feedstock powder particles are heated during their acceleration due to the compression induced by the shock waves (Villafuerte et al, 2009). The SWICGS is different from CGDS, in which the gas jet cools down as it expands in the diverging section of the DeLaval nozzle (Villafuerte et al, 2009). As a result of the particles being heated during flight in the SWICGS process, the critical particle velocity at which solid-state bonding takes place is effectively lowered (Villafuerte et al, 2009). This makes the SWICGS process able to achieve higher intermediate particle impact temperatures than the CGDS. Higher intermediate particle impact temperature achieved by the SWICGS results in lower critical velocities required for coat formation compared to CGDS.

The total combined kinetic and thermal energy of particles that the SWICGS process has, results in high deposition efficiencies (Villafuerte et al, 2009). Due to the high particle impact velocities offered by the SWICGS process, the spraying application can be extended to a wider range of materials including steels, cermets and titanium. The more efficient management of thermal energy at lower particle velocities, along with

intermediate gas flow, is a key factor in reducing energy and gas consumption when using the process (Villafuerte et al, 2009).

To experimentally prove the validity of obtaining jet velocities that are adequate for particle deposition (300-1200 m/s) under room temperature, a test rig has to be constructed. In spraying applications high jet velocities are required at very high frequencies. The rig construction is therefore necessary to demonstrate the practicality of generating strong compression waves repetitively at high frequencies. The investigation of the SWICGS process with an aid of a constructed test rig will help to understand the principles of gas dynamics involved.

1.3 Objectives

- Design and construct a shock tube rig that will accelerate driver gas flow to velocities required for particle's deposition in cold gas spraying applications.
- Use the shock tube rig to test for velocities which can be achieved when using a single diaphragm and a double diaphragm valve arrangement with air and helium as the driver gases.
- Use the shock tube rig to test for changes in driver gas flow velocity with the change in reservoir pressure for both valve arrangements (single and double) and both gas drivers (helium and air).

1.4 Literature Review

1.4.1 Cold Gas Spraying

The cold spraying processes can be classified into two categories, based on the flow driver mechanism; the CGDS process and the SWICGS process. The two figures below (fig 1 and 2) show the difference in operation of the two Cold Gas Spraying processes. In the CGDS process a converging-diverging nozzle also known as the De Laval nozzle is used to accelerate flow to velocities required for particle deposition. When flow is accelerated outwards, a rapid expansion occurs in the nozzle which lowers the temperature of the outgoing flow. Since the deposition of the particles depends on the before impact particle temperature among other factors; the cooling of the particles results in a higher critical velocity being required for particle deposition to occur.

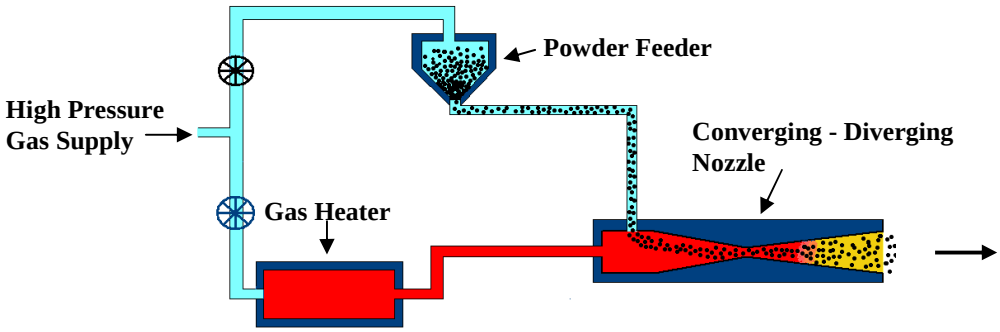

Figure 1: Schematic diagram of a Cold Gas Dynamic Spraying process

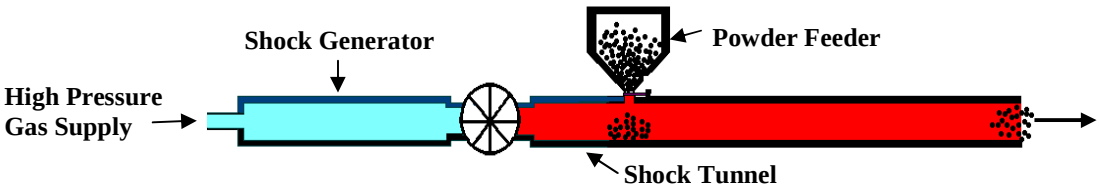

Figure 2: Schematic diagram of a Shock Wave Induced Cold Gas Spraying process

One of the major differences between the two processes is that the CGDS process is continuous and operates in a steady state; whereas the SWICGS operates with compression pulses that drive the spraying particles. The compression pulses are triggered one after the other. The shock generated is a moving one; and it is used to drive the flow instead of the flow moving across it. There is a flow

driver mechanism which uses the combination of both processes (CGDS and SWICGS) where the shock tube is fitted with a nozzle at the end. Work involving this kind of a driver mechanism has been done at the shock wave laboratory of RWTH Aachen University in Germany (Luo et al, 2009).

1.4.1.1 Coat Formation

Except for very thin coatings, the spray process can be considered as a process that consists of two stages: the spraying of the first layer of particles on a substrate, and the build-up of the coating (Papyrin, 2007). The fist coating layer in cold gas spraying is very vital for a successful coat. During the first stage, the particles interact with the substrate, and this process determines the quality of the boundary coat and the coating adhesion. The first stage of coat spraying turns out to be more complicated, because it depends on particle and substrate parameters such as roughness, hardness and temperature (Papyrin, 2007). The first stage also depends on the state of the surface, which changes as the number of particle impacts increases (Papyrin, 2007).

The nature of adhesion of metallic particles with velocities ranging from 400m/s to 1200m/s and temperatures much lower than the melting point of the particle material to the substrate is not yet properly defined in theory. The factors that complicate the study of this phenomenon are as follows (Papyrin, 2007):

- The size of the feed stock particles being very small ($d_p = 10^{-5} m$).
- The short time of particles interaction with the substrate ($t = 10^{-8} s$).
- The phase state of interacting objects in micro volumes near the contact boundary.

The process of adhesive particle-substrate interaction during cold spray can be considered within the framework of the approach widely used in gas-thermal spraying analysis (Papyrin, 2007). However, it should be noted that cold spray involves a much greater effect of kinetic energy of particles, leading to significant differences in interaction of cold particles and melted particles typical of gas thermal deposition techniques (Papyrin, 2007). The temperature of particles and substrate during contact depends on heat release in the zone of high plastic strains, in the cold spraying case. However, the heat release is not

important in the interaction of melted particles with the substrate in the case of thermal spraying processes.

1.4.1.2 Material Critical Impact Velocities

All particle/substrate materials have a critical particle impact velocity at which deposition will occur. There are two characteristic regions separated by the critical velocity which can be identified; the region below the critical velocity and the region above the critical velocity. At the region where particles velocity is below the critical velocity ($v_p < v_{ct}$) substrate erosion takes place. Substrate erosion is not desirable in Cold Gas Spraying since it damages the substrate instead of forming a coat. In the region above the critical velocity ($v_p > v_{ct}$) the coating process begins to take place. In this region, the deposition efficiency rapidly increases to around 50–70% as the particle velocity significantly exceeds the critical value (Papyrin, 2007). Studying the substrate surface has shown that all single particles with $v_p \leq v_{ct}$ whereby the $v_p \approx$ 250m/s are reflected on the substrate (Papyrin, 2007). As the velocity increases within the range $v_p \geq v_{ct}$, the character of particle-substrate interaction is drastically changed; and a rapidly growing coating is formed on the substrate surface when $v_p \approx$ 900m/s (Papyrin, 2007). The typical values of the critical velocities (v_{ct}) for various metals (Al, Cu, Ni, and Zn) are within 500–700 m/s (Papyrin, 2007).

Deformation of aluminum particles with different impact velocities on a polished copper substrate is shown on figure 3 below. Particle impact velocities of 625m/s, 730m/s and 850m/s where tested. The microphotographs of attached aluminum particles on a polished copper substrate, illustrate the character of particle deformation depending on the impact velocity (Papyrin, 2007). For v_p = 625m/s, there is no layer of crown-shaped outbursts that appears over the peripheral of attached particle. A thin layer of crown-shaped outburst appears over the peripheral of attached particles for v_p = 730m/s, and is more noticeable at v_p = 850m/s. The layer of the crown-shaped outburst over the peripheral indicates how

much the particle has deformed to fuse with the substrate and the thicker the layer the greater the fusion (deposition efficiency).

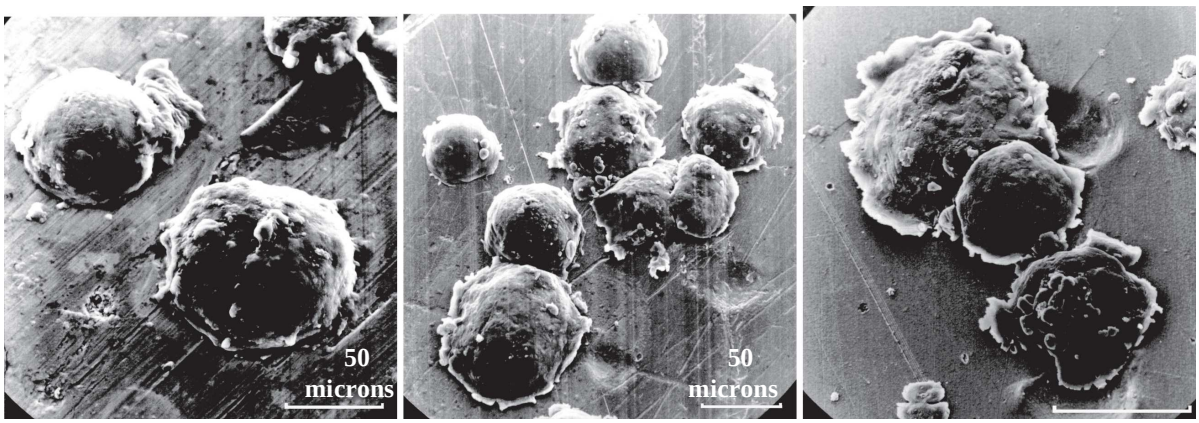

(a) v_p = 625m/s **(b)** v_p = 730m/s **(c)** v_p = 850m/s.

Figure 3: Deformation of aluminum particles with different impact velocities on a polished copper substrate (Papyrin, 2007).

The impact velocity of particles in cold gas spraying depends on a number of factors. The spraying feed-powder particle size, the spaying feed-powder material type and the type of a carrier gas being used dictate the impact velocity ranges that can be achieved. From figure 4 below it can be clearly seen that helium as a gas carrier yielded higher impact velocities compared to air. It is also important to note from the figure that different materials have different critical particle diameters where the highest impact velocities can be archived.

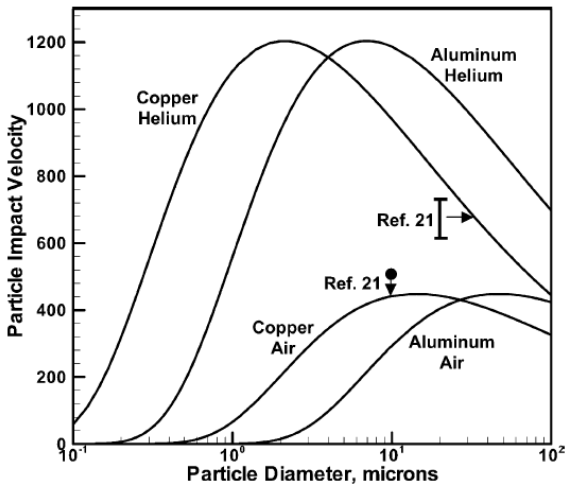

Figure 4: Effect of the particle size, the feed-powder material and the carrier gas of the particle critical impact velocity for adhesion (Grugicic et al. 2003).

1.4.1.3 Deposition Efficiency and Temperature Effects

In cold gas spraying processes the feedstock particles are in a solid state before their interaction with the substrate. This means that the cold spray method can be used for coating applications at room temperature. However, the use of a pure air jet at room temperature does not ensure formation of coatings for some of the materials. The before-impact temperature can be increased by pre-heating the powder feed stock. It is important to emphasize that the particle temperature under such pre-heating is always much lower than the melting point of the particle material, providing coating formation from particles in the solid state. Figure 5 below shows the results of measured deposition efficiencies for various metallic powders (aluminum, copper, and nickel) as a function of stagnation temperature of the driver jet. From the figure it is observed that the deposition efficiency of the particles increases with the increase in stagnation temperature.

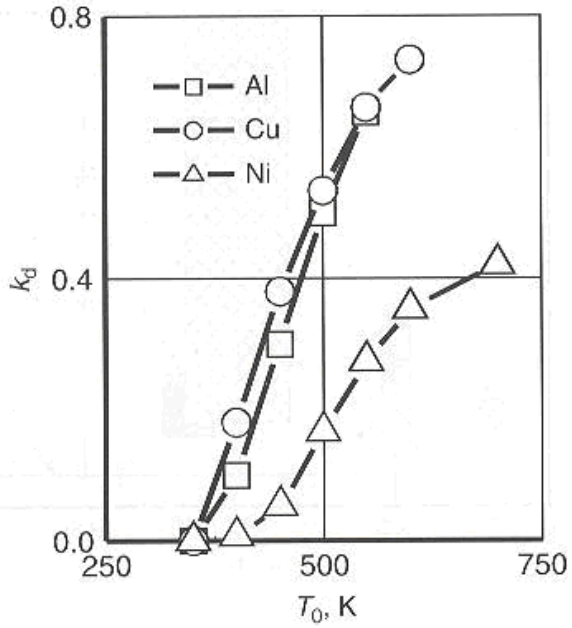

Figure 5: Deposition efficiency of aluminum, copper, and nickel powders sprayed on copper substrate versus the air jet stagnation temperature (Papyrin, 2007)

In figure 6 below curves 4, 5 and 6 show the data of figure 5 above for the aluminum, copper, and nickel powders, but the data is plotted versus the particle velocity used in the computations (with the corresponding temperatures of air heating). By comparing these dependences with those obtained with the use of an air-helium mixture as a driver gas at T_0 = 300K (curves 1–3), it can be concluded that the particle and substrate temperatures also have a significant effect on the spraying process; otherwise these two families of curves would coincide (Papyrin, 2007). The pre-heating of the air in the pre-chamber increases the particle temperature, which results in both an increases in particle velocity and particles substrate temperature. For that reason, the drastic increase observed for the deposition efficiency can be attributed to the growth of both the velocity of sprayed particles (which increases the pressure and temperature in the contact at the impact moment) and the temperatures of the sprayed particles and the substrate (which can lead to changes in their properties, increase in temperature in the particle–substrate contact, and hence, displacement toward lower values of the critical velocity (v_{cr}) (Papyrin, 2007). It can also be observed that slight preheating of the jet allowed for the decrease the critical

velocity and, as a consequence, to extend the range of sprayed materials with an air jet (Papyrin, 2007).

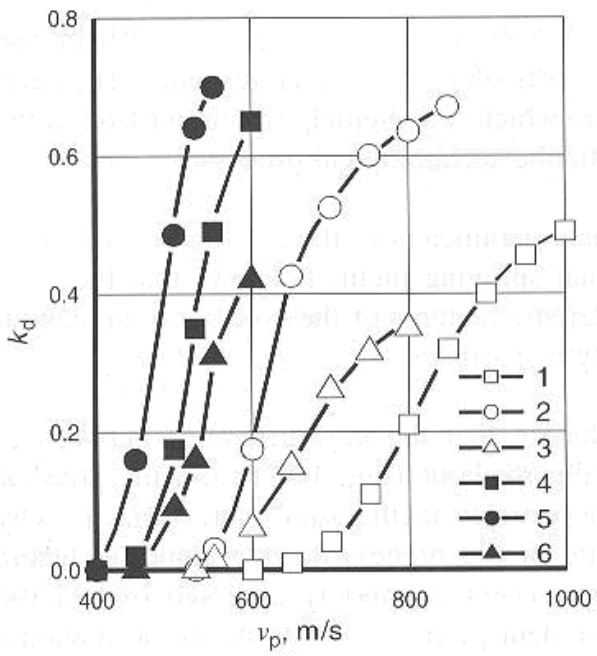

Figure 6: Deposition efficiency for aluminum, copper, and nickel powders accelerated by an air helium mixture (1-3) and by heating air (4-6) versus particle velocity (Papyrin, 2007)

The use of a supersonic jet of air-helium mixture and having a stagnation temperature of 300K and the use of a slightly preheated (T≤ 500 – 600K) supersonic air jet allowed for obtaining of coatings from most metals and many alloys (Al, Cu, Ni, Zn, Pb, Sn, V, Co, Fe, Ti, bronze, brass, etc.) with particles of the size d_p < 50 μm onto various metallic and dielectric substances (in particular, glass, ceramics, etc.) (Papyrin, 2007). The deposition efficiency of the powders reaches 0.5–0.8, which is extremely important from a practical point of view in the development of particular technological processes (Papyrin, 2007). The preheating capability increases the coating applications of cold gas spraying, and makes it more appealing when compared to other spraying processes such as thermal spraying.

1.4.1.4 Cold Gas Spraying Advantages and Applications

Eliminating the harmful effects of high temperature on coatings and substrates such as in thermal spraying offers significant advantages and new possibilities for cold gas spraying. These include (Papyrin, 2007):

- Avoiding oxidation and undesirable phases;
- Retaining properties of initial particle materials;
- Providing high density, high hardness, cold-worked microstructure;
- Spraying thermally-sensitive materials;
- Preparing the substrate minimally with surface preparation/masking, short standoff distance;
- Depositing many materials at high deposition rates and efficiencies;
- Collecting and re-using particles (powder utilization up to 100% with recycling);
- Increasing operational safety because of the absence of high-temperature gas jets, radiation, and explosive gases.

The above listed advantages make cold spray promising for producing and repairing a wide range of industrial parts. Examples include turbine blades, pistons, cylinders, valves, rings; and bearing components, pump elements, sleeves, shafts, and seals for many industries. Various coatings may add strengthening, hardening; wear resistance, corrosion resistance, electro-magnetic conductivity, thermal conductivity, and other properties (Papyrin, 2007). The process is also suitable for production of compact powder materials and for direct fabrication of parts.

1.4.1.5 Powder Feeder and Feedstock Particles

One of the important elements of the cold spray setup is the powder particles feeder, which should provide a uniform controlled supply of the powder into the spraying gun. Most powders used in cold spraying have sizes ranging from 1 to 50 μm and it is difficult to provide a uniform powder feed rate because of the powder's agglomeration. Many traditional powder feeders become ineffective working with such fine powders. It is also desirable in the cold spray process that the powder feeder is able to preheat powder particles to temperatures around 500K, for high deposition efficiencies. Due to the complexity and functional requirements of powder feeders; they are usually very capital intensive.

1.4.2 Shock Tubes and Gas Dynamic Principles

1.4.2.1 Normal Shock Waves

A normal shock wave is a strong compression wave with very large amplitude, propagating at a supersonic velocity in the direction perpendicular (at 90°) to the shock medium's flow direction.

The normal shock wave is an irreversible occurrence in one dimensional flow and is characterized by discontinuous changes in the flow properties of pressure, temperature and density (Skews, 2008). The occurrence of a true mathematical discontinuity hinges on the assumption that the fluid is a continuum (Skews, 2008). Since gases are composed of individual molecules, a true discontinuity cannot occur; however, the assumption of a true discontinuity is satisfactory and closely approximates what happens in real gases (Skews, 2008). Normal shock waves can be classified into; stationary normal shock waves and moving normal shock waves. The moving normal shock wave can use the same relations as the stationary one; this can be achieved by superimposing a reference velocity on the observer so that the moving shock appears stationary to the observer. Moving normal shock waves can be generated experimentally by making use of shock tunnels/tubes.

1.4.2.2 Shock Tube Design

Figure 7 below shows a shock tube schematic with a single diaphragm arrangement. The gas tight valve which acts as the diaphragm divides the shock tube into two regions; known as the compression chamber (region $4'$) and the expansion chamber (region $1'$). The compression chamber contains a gas at a pressure $P_{4'}$, which is greater than pressure $P_{1'}$ of the gas in the other half of the tube. When the valve separating the two regions opens a shock wave travels into the expansion chamber; and the expansion waves travel into the compression chamber. The expansion waves travelling into the compression chamber would eventually reduce the pressure in the chamber to atmospheric if the separating valve is opened for long enough.

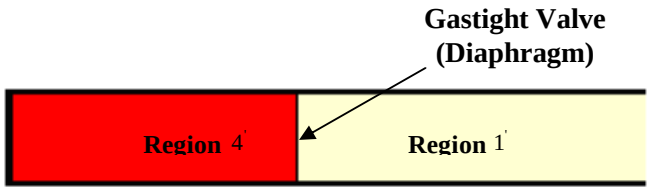

Figure 7: Single diaphragm shock tube schematic

Figures 8a and 8b below show the pressure distribution along the tube before and after the valve has been opened. The dotted line in figure 8b denotes the position of the gas which was originally at the valve before opening (Wright, 1961). The gas to the right of the dotted line has been compressed and heated by the shock wave but the gas to the left of the line has expanded from the compression chamber and has therefore been cooled (Wright, 1961). Across the dotted line there will therefore generally be a change in properties such as temperature and density, such a point is known as a contact discontinuity.

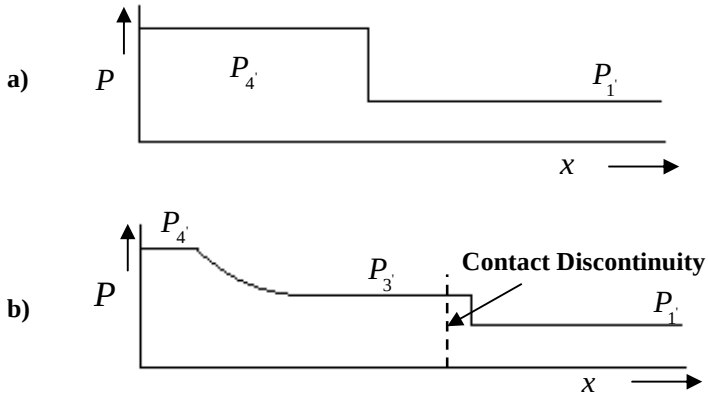

Figure 8: Pressure plot before and immediately after diaphragm rupture (Wright, 1961)

The immediate velocity and temperature distribution inside the expansion chamber when the valve is opened is shown in figures 9 and 10 below. The velocity and temperature distribution inside the tube are based on a one dimensional flow modelling. From the distribution plots it can be observed that the highest temperature and pressure occurs in the region immediately behind the shock front (region $2'$). This is the region that accelerates the powder particles in the spraying gun to high velocities.

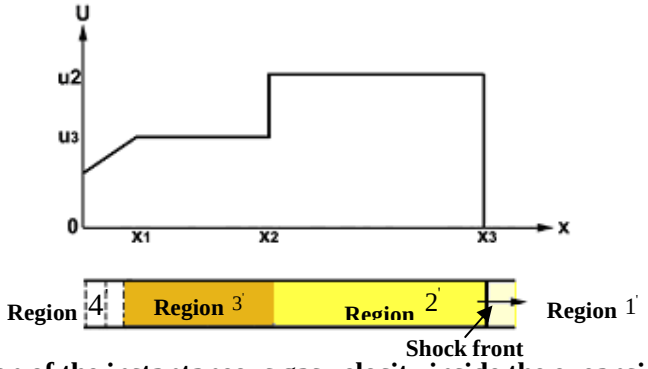

Figure 9: Representation of the instantaneous gas velocity inside the expansion chamber just before the shock wave exits the tube

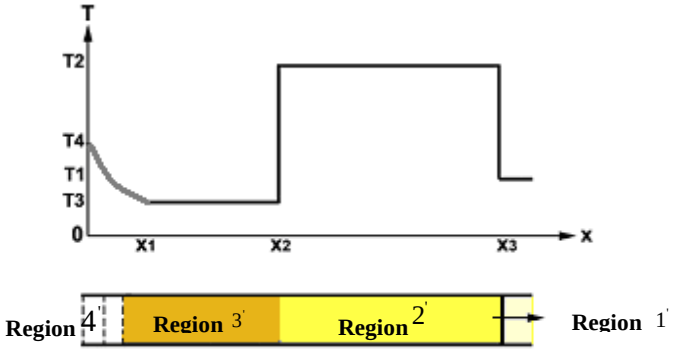

Figure 10: Representation of the instantaneous gas temperature inside the expansion chamber just before the shock wave exits the

1.4.2.3 Production of strong shock waves

1.4.2.3.1 The use of light driver gas

Sound has a higher speed when travelling through gases with a higher pressure/density ratio. The use of a gas with high sound speed is the basis of many important shock tubes to produce strong shock waves (Wright, 1961). The production of strong shock waves is based on the following formula:

$$M = \frac{\gamma_1 + 1}{\gamma_4 - 1}\frac{a_4}{a_1} \qquad (1)$$

Where M is the Mach number of the wave; a_4 is velocity of sound in the driver gas; and a_1 is the speed of sound in air. From the relationship it can be seen that the greater the speed of the driver gas, the greater the Mach number of the generated waves. Various methods of using the increase in shock strength with compression chamber sound speed are

widely used (Wright, 1961). The simplest method employs a light gas such as hydrogen or helium in the compression chamber. Of the two gases hydrogen has a higher sound speed, but the gas is very inflammable. This makes helium a more proffered alternative.

1.4.2.3.2 Gas pre-heating

Pre-heating of the gas driver increases its sound speed and hence the strength of the shock generated. Methods of heating the compression chamber gas suffers from the disadvantage that they tend to leave the compression chamber gas in a non-uniform condition and the shock wave is consequently attenuated as it propagates down the expansion chamber (Wright, 1961).

1.4.2.3.3 Multiple Diaphragm Shock Tube

Figure 11 below shows a multi diaphragm shock tube arrangement. The gas in the intermediate chamber is at a lower pressure than the compression chamber. The expansion chamber has the lowest pressure of the three regions, usually atmospheric.

The diaphragm between the compression and intermediate chamber is ruptured and the shock wave which travels down the intermediate chamber is reflected at the diaphragm between the intermediate and expansion chambers (Wright, 1961). The pressure behind the reflected shock is sufficient to rupture the second diaphragm but, before it has time to open fully; the reflected shock has travelled back leaving a hot, high-pressure region to act as a compression chamber gas which will drive a shock wave down the expansion chamber (Wright, 1961). Each additional chamber increases the shock strength by a factor of 12 or 16 according to whether the gas employed has a γ of 5/3 or 1.4 respectively (Wright, 1961).

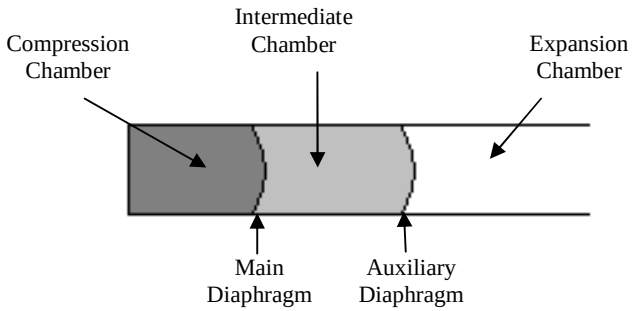

Figure 11: Multi diaphragm shock tube arrangement

Another advantage of using multi stage diaphragm is that even if the gas is pre-heated, it leaves the compression chamber in a uniform condition. All the preceding theory is based on the assumption that the time of rupture of the intermediate diaphragm is long compared with the time for the reflected shock to travel an appreciable distance (Wright, 1961).

1.4.2.4 SWICGS Flow Cycle

In this section the process that occurs in one pulse spray cycle of SWICGS in explained. One pulse cycles is divided into the firing phase (when the valve is opened to create a shock wave) and the filling phase (where the valve is closed to allow pressure build-up in the compression chamber).

1.4.2.4.1 Firing Phase

Figures 12a, b and c below show the process that occurs from the opening of valve B to the point where powder particles in the spraying gun are accelerated through the gun exit point. Before the valve opening, the shock tube is divided into two regions; which are region $1'$ (at atmospheric conditions) and region $4'$ (pressurized driver gas). Subsequent to the opening of valve B, a shock wave is generated. The shock wave moves downstream of the tube and overtakes the spraying powder particles, which it then accelerates to high velocities. The spraying particles are moved by the high temperature, high pressure and high velocity region immediately behind the shock wave (region 2). Region 2 and region 3 behind the shock wave are at the same pressure but different temperatures, with region 2 having a higher temperature.

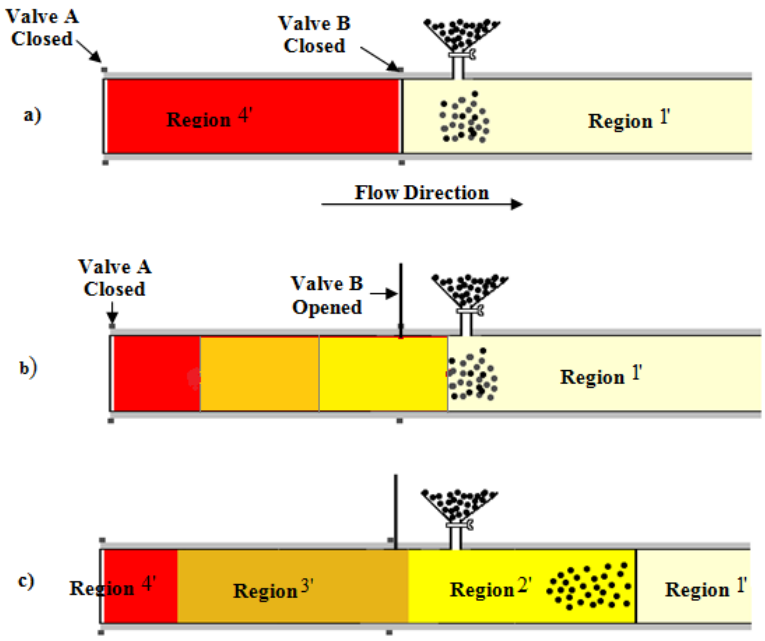

Figure 12: Firing phase schematic of one pulse cycle

1.4.2.4.2 Filling Phase

Assuming that valve B was opened for long enough, such that the conditions in the entire tube are now at atmospheric conditions (similar to region $1^{'}$). Figures 13a, b and c below show the process that occurs from the point that the tunnel is at atmospheric conditions to a point where it is re-filled and ready for the next firing phase. Once the compression waves have exited the spraying gun, valve B will be closed and valve A will be opened. Compressed gas will flow into the tunnel from the reservoir. The compressed gas will flow into the empty compression chamber, reflect on valve B and create a high temperature pressure zone in region $4^{'}$. Once the high pressure and temperature zone is created in region $4^{'}$ valve A will be closed and powder particles will be introduced into the tunnel and the tunnel will be ready for the next firing phase.

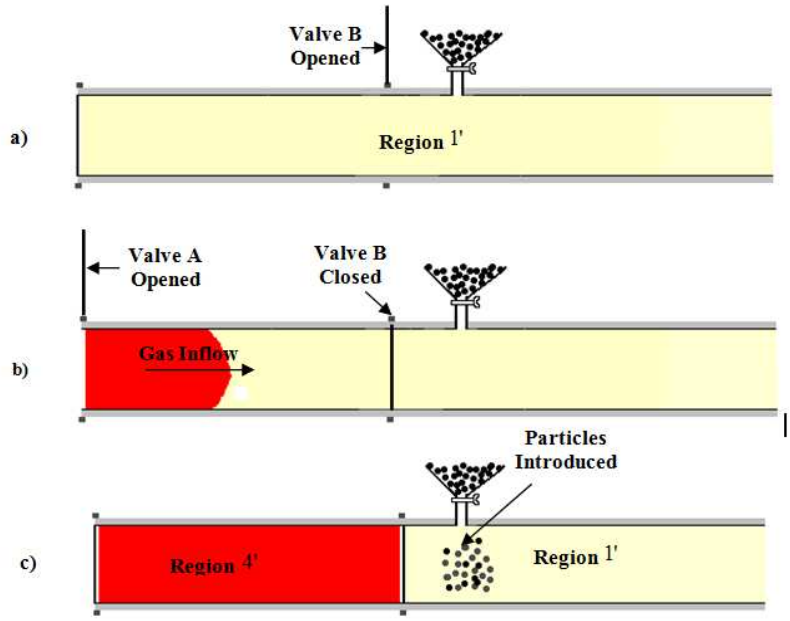

Figure 13: Filling phase schematic of one pulse cycle

1.4.2.4.3 SWICGS Cycle Shock Wave Diagram

The firing process mentioned above can also be represented in a form of a wave diagram as shown in figure 14. The wave diagram shows an ideal two stage shock wave generation (multi diaphragm arrangement) that occurs. When valve A is opened during the filling phase, a primary shock wave which reflects on valve B is generated. This reflected shock wave creates a high temperature high pressure region which is denoted by region $4'$. When valve B is opened during the firing phase a second shock wave is generated. The secondary shock wave is the shock wave that is shown driving the particles during the firing phase in figure 12. Region 4 represents conditions in the reservoir; and region 1 is at atmospheric conditions.

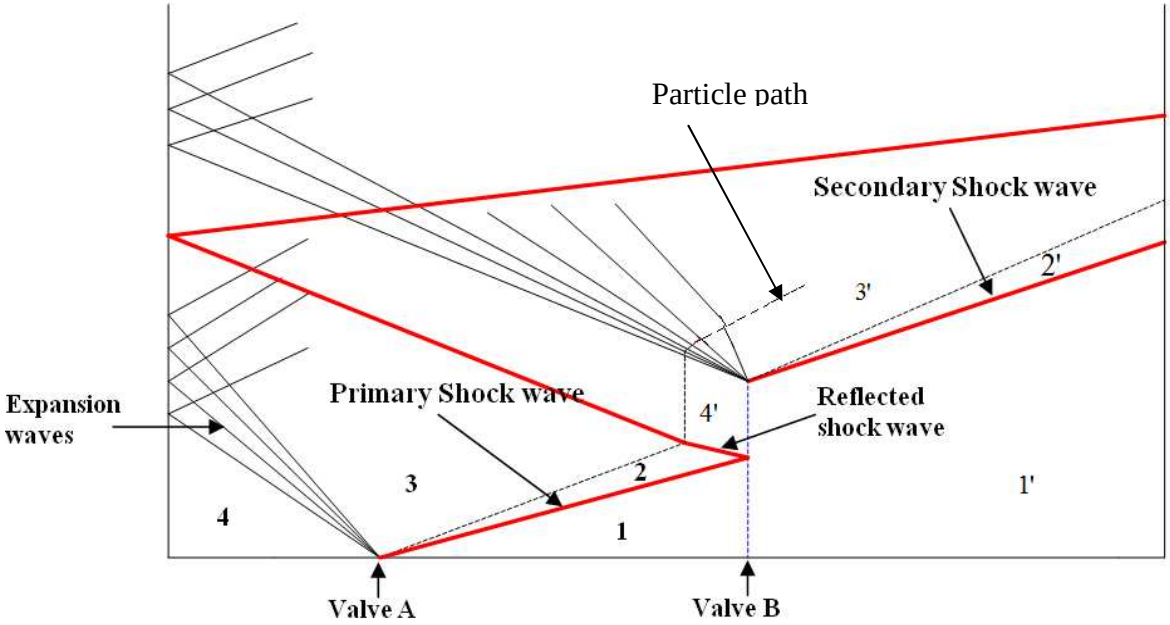

Figure 14: An ideal shock wave diagram for a double valve arrangement showing the primary, reflected and secondary shock waves.

1.4.2.5 Process Modelling

1.4.2.5.1 Primary Shock wave

The first stage is to determine the velocity of the primary shock wave; the known initial conditions are the pressure (P_1 and P_4), temperature (T_1 and T_4), and density (ρ_1 and ρ_4) for region 1 and region 4. The pressure (P_2), temperature (T_2) and density (ρ_2) of region 2, which is the region immediately behind the primary shock wave, can be calculated using equations 1, 2 and 3 respectively (Anderson, 1982). Due to the nature of the equations a solution will have to be found through an iterative process.

Pressure:

$$P_2 = P_4 \left[1 - \frac{(\gamma_4 - 1)\left(\frac{a_1}{a_4}\right)\left(\frac{P_2}{P_1} - 1\right)}{\sqrt{2\gamma_1\left\{2\gamma_1 + (\gamma_1 + 1)\left(\frac{P_2}{P_1} - 1\right)\right\}}} \right]^{\frac{2\gamma_4}{\gamma_4 - 1}} \qquad (2)$$

Temperature:

$$T_2 = T_1 \left[\frac{\frac{P_2}{P_1}\left[\left(\frac{\gamma+1}{\gamma-1}\right)+\frac{P_2}{P_1}\right]}{\left[1+\left(\frac{\gamma+1}{\gamma-1}\right)\frac{P_2}{P_1}\right]} \right] \quad (3)$$

Density:

$$\rho_2 = \rho_1 \left[\frac{\left[\left(\frac{\gamma+1}{\gamma-1}\right)\frac{P_2}{P_1}+1\right]}{\left[\left(\frac{\gamma+1}{\gamma-1}\right)+\frac{P_2}{P_1}\right]} \right] \quad (4)$$

In all three equations above, γ is the specific heat ratio of the gas medium and a is the speed of sound at the medium's temperature. Figure 15 below shows the primary moving normal shock wave with a gas of velocity V_2 moving behind it. The shock wave is propagating at velocity V_S into still air which is as atmospheric conditions. It should be noted that the velocity of the gas behind the shock is not the same as the velocity of the normal shock wave itself.

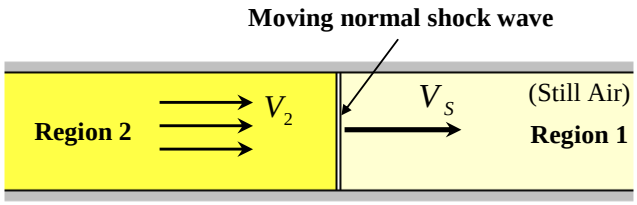

Figure 15: Moving primary normal shock wave between region one and region two

The primary normal shock wave velocity can be found using the following (Anderson, 1982):

$$V_S = a_1 \sqrt{\frac{\gamma+1}{2\gamma}\left(\frac{p_2}{p_1}-1\right)+1} \quad (5)$$

The shock wave velocity can also be expressed in terms of its Mach number and sound speed in the gas ahead of it and the relationship is

$$V_S = M_S \times a_1 \qquad (6)$$

Finally, the actual velocity of the gas behind the moving shock in region two is given by (Oosthuizen et al, 1997):

$$V_2 = \frac{2\left(M_S{}^2 - 1\right)}{(\gamma+1)M_S} a_1 \qquad (7)$$

1.4.2.5.2 Reflected Shock Wave

When the primary shock wave reflects on valve B, a region of higher temperature and pressure is generated. The moving reflected shock can be modelled as a stationary shock with gas flowing across it. In this modelling, the shock divides the flow across it into the **x** and **y** components. The x component is upstream of the shock and the y component is downstream of the shock. Conditions in the **y** component represent the high temperature and pressure conditions of the reflected shock. The reflected shock can be represented as shown in the figure 16 below. The pressure and temperature conditions of component x are similar to those of region 2. The velocity of component x is the sum of the reflected wave and that of region 2 . An iterative process will have to be followed and tables of compressible flow of air will have to be used to calculate conditions in component y.

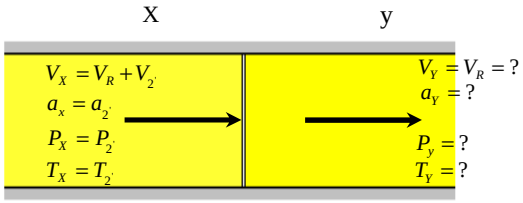

Figure 16: Reflected shock presented as a stationary shock.

1.4.2.5.3 Secondary shock wave

To find the strength of the secondary shock similar equations as in the primary shock will be used. The difference will be the initial conditions; which will be the conditions of the reflected shock in this case. The conditions of region $4'$ will be represented by the conditions of the reflected wave. Finally, the secondary shock wave will be formed, creating the region $2'$ in which the powder particles are going to be accelerated.

1.4.2.6 Particles Momentum Transfer

In general, gas/solid particle transport phenomena should be considered within the framework of the suspension flow in which the fluid/particle medium is taken as a single phase with its own particular properties (Sung at al, 1991). The drag coefficient of the particle C_D can be taken from.

$$C_D = a_1 + \frac{a_2}{R_e} + \frac{a_3}{R^2{}_e} \tag{8}$$

Where constants a_1, a_2 and a_3 apply for smooth spherical particles over a range of relative Reynolds numbers R_e (Morsi et al, 1972), See appendix C.

The relative Reynolds number (i.e. the particles Reynolds number) can be defined by:

$$R_e = \frac{\rho D_P \left| u_p - u \right|}{\mu} \tag{9}$$

The acceleration of the particle can be measured using the following:

$$\frac{d_v}{d_t} = \frac{\rho (v - v_p)^2 A_P C_D}{2 m_p} \tag{10}$$

1.4.2.7 Impinging Jet Flow

As shown in figure 17 the impinging jet flow field can be divided into three main regions (Donaldson et al, 1971). The first region represents the main jet column in which the flow is primarily inviscid and contains expansion and compression shock waves for non-ideally expanding jets (Grugicic et al, 2003). The second region, generally referred as the impinging zone, involves the region of jet impingement onto the substrate, which is characterized by large gradients which cause major changes in the local flow properties (Grugicic et al, 2003). The third region, known as the radial wall jet, includes the area outside the impingement zone which contains the jet flow, redirected laterally outward after impingement (Grugicic et al, 2003). When approaching the substrate a bow shock is developed and the primary jet is slowed down. Feed powder particles carried by the jet flow gain momentum during flight, and due to the momentum attained the feed powder particles are not slowed down as much as the jet flow. This enables the feed powder particles to impact the substrate at a reasonable higher speed.

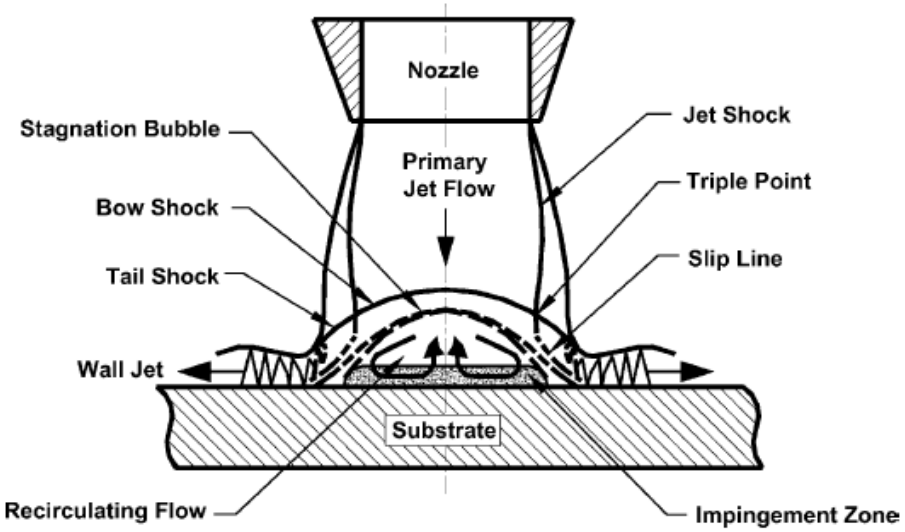

Figure 17: Schematic of a supersonic impinging jet flow field (Grugicic et al, 2003)

1.4.2.8 Pressure Measurement Techniques

Surface pressure measurements in short duration facilities require different approaches than for continuous running facilities (Tropea et al, 2007). Because the measurement time is short, pressure transducers with fast response time have to be used (Tropea et al, 2007). In addition to the fast response time, the susceptible area of the pressure transducers has to be installed close to the surface to minimize the filling time of the tubing system in front of the susceptible area (Tropea et al, 2007). Pressure gauges most commonly used in short-duration hypersonic ground-based test facilities are piezoelectric pressure transducers.

To achieve fast response times, the susceptible area of the pressure transducer has to be positioned as close as possible to the model surface. As shown in figure 18 (a) below, small holes are drilled in the model which act as pressure tappings (Tropea et al, 2007). The pressure transducer gauge is placed directly behind these tappings. This installation is not suitable for stagnation regions, where the flow may directly stagnate on the pressure transducer leading to high heat flux on the susceptible area. A stagnation installation is shown in figure 18 (b), where the susceptible area is protected by the stagnation plate (Tropea et al, 2007).

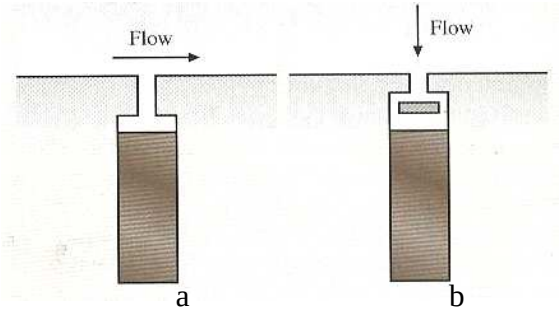

Figure 18: Pressure transducer orientation for different flow directions (Tropea et al, 2007)

1.4.3 KASIMIR Simulation Software

The name KASIMIR is a German abbreviation for 'Shock tube simulation on a computer'. The KASIMIR program simulates what physically occurs inside a shock tube tunnel in a relatively short space of time. The program calculates the complete x,t-wave plan which is displayed on the computer screen and provides information about the variables of state (e.g. pressure, temperature, density, shock velocity, chemical composition) at each position (Kasimir, 2009). The ability to simulate the phenomena inside a shock tube makes KASIMIR a powerful tool to design new shock tube experiments, to understand the experimental records, and to predict the gas dynamics inside the shock tunnel. Figure 19 below shows an example of a plot that can be obtained using the simulation software.

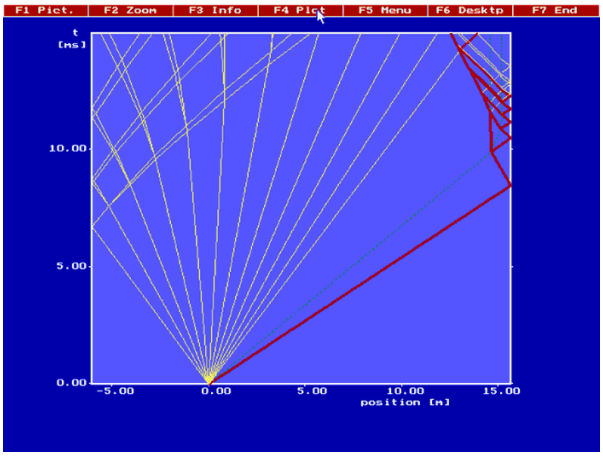

Figure 19: X-t-diagram of waves in a shock tube calculated with KASIMIR

The KASIMIR program is based on a one-dimensional code which takes into account high temperature effects assuming chemical and thermal equilibrium (Kasimir, 2009). The

program has several common gas models installed, and should the user want to define their own gas models not included in the code; they can do so.

1.4.3.1 Theoretical Basis of KASIMIR

The flow inside a shock tube is characterized by strong changes of the variables of state. The variables of state are calculated on the basis of statistical mechanics with the following assumptions (Kasimir, 2009):

- Thermochemical equilibrium.
- The flow in the shock tube is one-dimensional.
- Losses caused by the rupture of the diaphragm as well as the influence of the boundary layer are neglected.
- An exact Riemann solver is employed to reconstruct the wave plan and to determine the variables of state. Therefore, there is no numerical diffusion inherent in the solution.

1.4.4 Solenoid Valves

1.4.4.1 Valve Types and Characteristics

A solenoid valve is a combination of two functional units; a) a solenoid operator essentially consisting of a coil and spring, and b) a valve body containing an orifice in which a seal disc, diaphragm or piston is located, which is positioned according to the type of technology used. The valve is opened or closed by movement of the magnetic core which is drawn into a solenoid when the coil is energized; this makes the solenoid valve to have a very fast response time when opening and closing. Different types of solenoid valves which can be considered to act as a diaphragm in a shock tube are discussed in Appendix D.

1.4.4.2 The Effect of the Solenoid Valves on the Compression Waves

The purpose of the valves is to provide a gas tight seal between the compression and expansion chamber, which are to be opened and closed as required. There is usually a time delay in the opening of the valves before the valve can fully open. The compression waves may therefore have travelled several meters down the tube before a well defined shock is formed (Wright, 1961). When a diaphragm is used in a shock tube, the one dimensional

character of the shock tube flow tends to be destroyed. Under the initial differential pressure it tends to bow. As soon as it shatters the gas flow has a component towards the wall of the shock tube, rather than being directed purely along the axis (Wright, 1961). This effect results in transverse waves system being produced inside the shock tube.

Solenoid valves have a rigid internal orifice which will not tend to bow when there is a differential pressure between the compression and expansion chambers. However, valves such as the direct operated and lever type solenoid valve do not have a full bore flow valve but have a small curve through which flow has to travel. This curved path can result in a generation of transverse wave. There will also be a slight delay in the travelling of the flow, when compared to an ideal shock tube arrangement.

1.4.5 Structural Analysis

Several standards are used in industry for the analysis of pressurised pipes. The main standards which are used include ASME, DNV and ISO. These standards are based on the hoop stress and safety factor that is related with many other factors and best practices. In all of the norms for the above standards the design pressure in pipes is based on:

- Wall thickness
- Diameter
- Specified minimum yield strength

Safety factors are based:

- Material characteristics
- Environment
- Load
- Temperature
- Type of pipe manufacture
- Other integrated correction factors

For the structural analysis of the shock tube rig, the American standard ASME B31.13 is used. This standard is generally used for piping in industry. The straight pipe internal design pressure limit *pd* calculation equation is as follows (ASME B1.13, 2006):

$$t = \frac{pdD}{2[\sigma_Y + pdY]}\ ,\ (t \le D/6)\ ,\ \text{Y} = 0.4 - 0.7 \text{ and} \qquad (11)$$

$$(t \succ D/6)\ ,\ Y = \frac{d + 2c}{D + d + 2c}$$

Where *pd* is design pressure based on yield strength; *F* is safety factor; *t* is wall thickness; *D* is outside diameter; σ_y is yield strength; *d* is inside diameter; *c* is sum of mechanical allowances (corrosion, and erosion) and Y is a coefficient which depends on a number of factors.

Table 1: Values of Coefficient Y for $t \succ D/6$

	Temperature, °C (°F)					
Materials	≤ 482 (900 & Lower)	510 (950)	538 (1000)	566 (1050)	593 (1100)	≥ 621 (1150 & Up)
Ferritic steels	0.4	0.5	0.7	0.7	0.7	0.7
Austenitic steels	0.4	0.4	0.4	0.4	0.5	0.7
Other ductile metals	0.4	0.4	0.4	0.4	0.4	0.4
Cast iron	0.0	. . .	. . .	. . .	. . .	. . .

Chapter 2 Shock Tube Rig Design

The shock tube rig designed is to be used to accelerate gas flow to velocities required for particle's deposition in the cold gas spraying process. The rig should accommodate both the single (single valve arrangement) and double diaphragm (double valve arrangement) experimentation. It should also accommodate different gas drivers. The rig should accommodate the introduction of spraying gas particles at a later stage. The powder particles may range from 1 to 50 microns in size. The powder particles are to be introduced inside the shock tube at the expansion chamber. The induced shock wave generated downstream of where the particles are introduced will then accelerate the particles to a required velocity. The product requirements specifications are indicated in the section below.

2.1 Product Requirements Specification

2.1.1 Requirements

- The tube should have an internal diameter ranging from about 4mm to 5.5 mm.
- The structure should have a safety factor of at least 10.
- The reservoir should be large enough to create stagnation conditions
- Accelerate powder particles to a velocity of about 600m/s to 1200m/s.
- Have a pulsating system with a high shock generation frequency.
- Accommodate tests with both a single diaphragm and a double diaphragm arrangement.
- Accommodate air and helium as gas drivers.

2.1.2 Constraints

- Universities are not allowed to build pressure vessels with a diameter greater than 150mm without any authorization.
- The rig should fit in the CGS laboratory

2.1.3 Criteria

- Should not be expensive to build
- Should be easy to construct
- Readily available materials should be used
- Safe to operate (High safety factors)

2.2 Functional Analysis

The critical areas in the construction of the shock tube are as follows:

2.2.1 The Transducer Ports:

Ports for transducer attachments have to be created at various points of the shock tube. Due to the high pressures that will be experienced in the shock tube sealing at the connection point is very important. Proper care has to be taken when designing.

2.2.2 Valve Selection:

Shock tubes normally have diaphragms which rupture in a very short space of time. Using valves in the place of diaphragms will be challenging in that valves with a very fast opening time while able to contain very high pressures will be required. The orifice of the valves in relation to the tube size is also very important; the valve orifice cannot be smaller than the tube's internal diameter as this could cause choking.

2.2.3 Reservoir Construction:

The reservoir is to handle a pressure of 50 Bars, This is a very high pressure and proper care has to be taken when designing. The reservoir also has to be large in relation to the tube, in order for stagnation conditions to occur.

2.2.4 Tube Dimensions:

The length and diameter of the tube are important in determining whether generated compression waves coalesce to form a shock wave or not.

2.3 Concepts Considered

2.3.1 Concept A

As shown in figure 20 the tube is made from a thick metal bar with a bore in its centre, the bar has thick walls in order to accommodate transducer ports. The shock tube is made out of three metal bar sections with a bore: the gun, shock generator and the reservoir connector. The metal bar sections are threaded on their ends to allow for connection to the valves and the reservoir vessel.

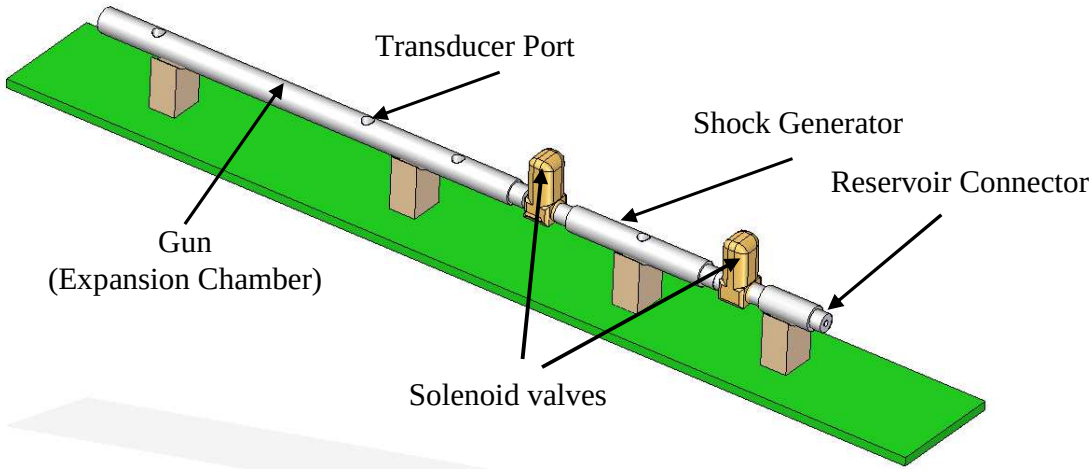

Figure 20: Concept A– Thick metal bar

Advantages

- Minimal shock tube flow disturbance at the point of transducer attachments.
- Fewer pipe sections used on the rig.
- Components are not fixed on one another (no welds), this will make the rig flexible when dismantling or assembling.

Disadvantages

- Due to the wall thickness the steel bar is not a standard part, it will be difficult to create a centre bore on the steel bar.
- The tapping points for transducer attachments are not on flat surfaces, this will be difficult to make.
- Creating threaded sections of the thick pipe for valve and reservoir attachment will be difficult.

2.3.2 Concept B

The shock tube consists of three pipe sections, the gun, shock generator and reservoir connector. There are four transducer stands on the rig. The transducer stands are made of steel blocks with a hole on their centre through which the pipe sections pass. The transducer stand blocks are tapped on the side at the point where the pipe passes them, the tapping is from the side through the pipe wall. The transducer blocks are welded to the pipe section to create a seal.

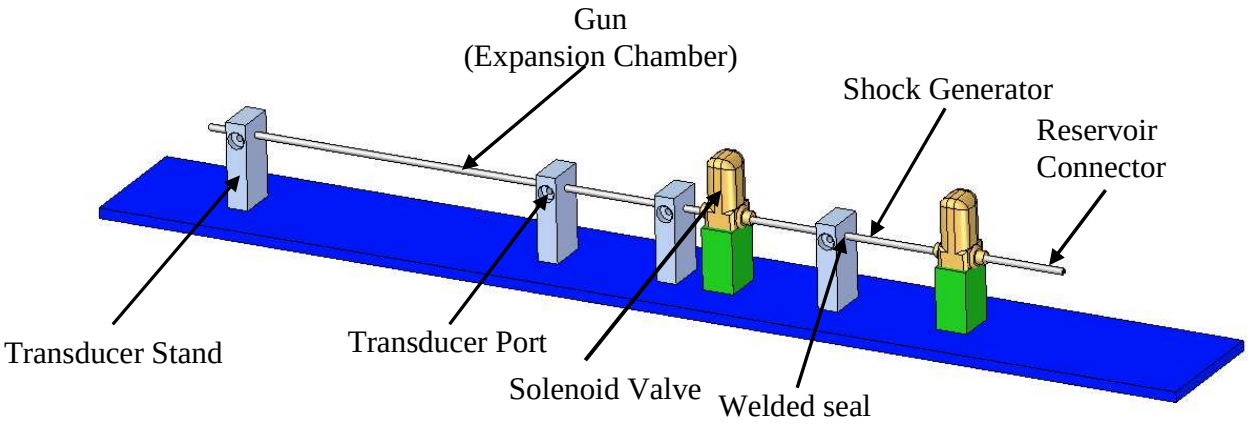

Figure 21: Concept B – Transducer stands

Advantages

- Flat sections transducer stands will make it easy to tap and accurately align the transducer with centre of the pipe.
- Standard pipe sections can be used.
- Minimal flow disturbance at the point of transducer attachments.

Disadvantages

- The pipe is welded to the transducer stands, which reduces the flexibility of the rig.

2.3.3 Concept C

In this concept the shock tube consist of seven pipe sections with t-pieces in between. The t-pieces connect to the pipe sections on two sides and house a pressure transducer on the threaded third side at the top. The shock generator consists of two short pipe sections and a t-piece in the middle. The pipe sections in the shock generator connect to the valves through fittings.

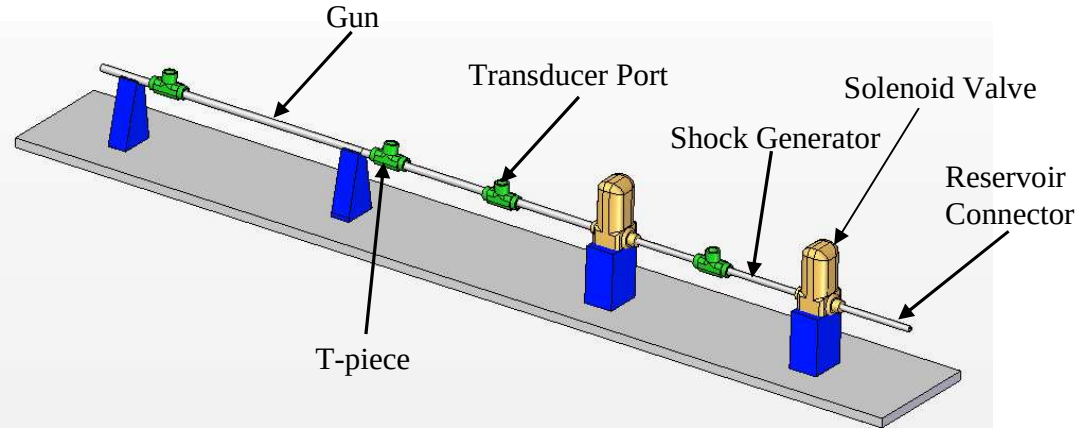

Figure 22: Concept C – T-piece connectors

Advantages

- Standard parts are used.
- Components are not fixed on one another (no welds), this will make the rig flexible when dismantling or assembling.

Disadvantages

- Large flow disturbance inside the tube at the transducer attachment points due to the t-piece sections.
- Many short pipe sections

2.4 Decision Matrix

Table 2: Concepts comparizon and decision making

Criteria	**Weighting**	**Concept A: Datum**	**Concept B**	**Concept C**
Safe to operate (High safety factors)	0.2	6	7	4
Handle Repeatability (handle repeatable experiments)	0.175	5	5	3
Use readily available material (standard parts)	0.15	2	4	5
Should be easy to construct (put together)	0.125	4	6	7
Should not be expensive to build	0.1	2	5	6
Provide undisturbed flow in the tube	0.25	4	7	2
Total	1	**4.075**	**5.875**	**4.05**

In the decision matrix the design criteria from the product requirements specifications (PRS) was used as a basis for a preferred design. Different criteria were allocated a fractional weighting out of 1, based on their importance. Different concepts were scored against the weighting, with a score level ranging from 1 to 10. In this case 1 represents low confidence and 10 represents high confidence.

From the above it was concluded that concept B is a more feasible design. High weightings in the decision making were given to provision of undisturbed flow, and safety of operation.

2.5 Detailed Design

2.5.1 Tube Length Decision

Inspired by the conducted literature review the following dimensions were selected for the shock tube using Kasimir simulation, see appendix G:

Shock generator length: **350mm**

Gun length: **750mm**

Reservoir connector length: **150mm**

Tube internal diameter: **5mm**

Tube outside diameter: **8mm**

2.5.2 Reservoir Size Decision

Inspired by the conducted literature review and Kasimir simulations (see Appendix G), the dimensions below were selected for the tube reservoir. The dimensions give the reservoir a total volume of 0.377 litres:

Reservoir length: **300mm**

Reservoir internal diameter: **40mm**

Reservoir outer diameter: **50mm**

With no net heat and work transfer between the test rig and its surrounding the reservoir will maintain stagnation conditions (Skews, 2008).

The reservoir assembly is shown in figure 23. The two side plates clamp the pipe section in between them using four threaded rods with nuts. O ring seals are used to seal between the pipe section and the reservoir stands. In order to accommodate pre-heating of the gas in the reservoir at a later stage a 20 mm clearance is allowed between the treaded rods and the pipe section. A transducer stand with a port is located at the centre of the reservoir. The stand is welded onto the reservoir pipe section.

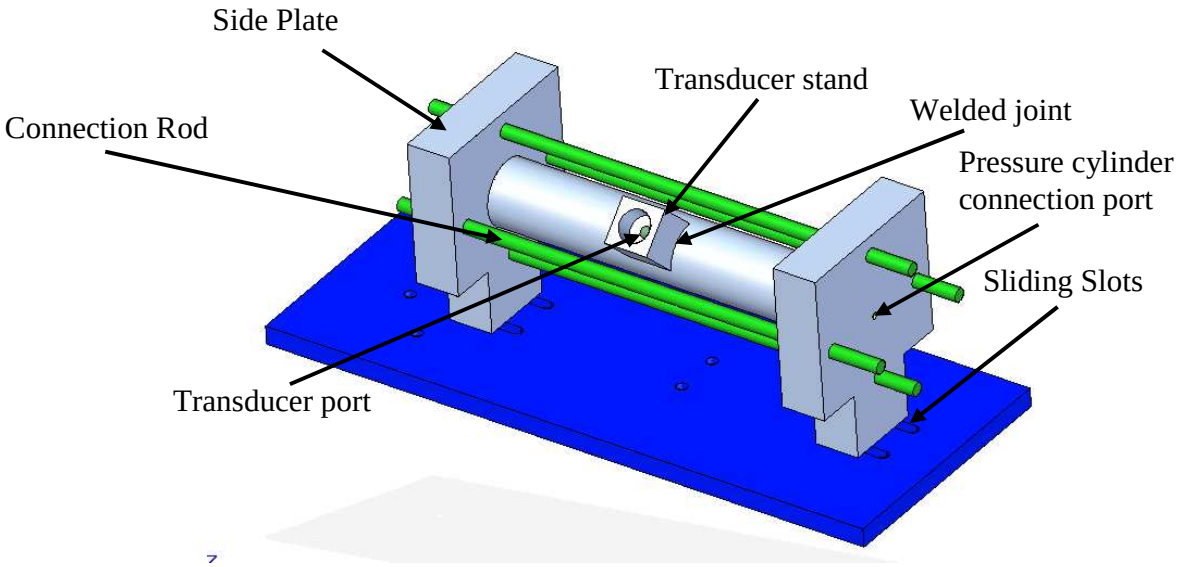

Figure 23: Pressure reservoir assembly

2.5.3 Transducer Size and Attachment

Considering the small internal diameter of the shock tube, pressure transducers with a very small sensing face have to be used. PCB pressure transducers with a sensing face of about 3 mm were selected. The transducers have an $M7\times0.75$ threaded section which connects to a mounting base of an M10 bolt size. As shown in figures 24 the tube will be inserted through the transducer stands and silver welded to avoid any damage to tube due to its small thickness

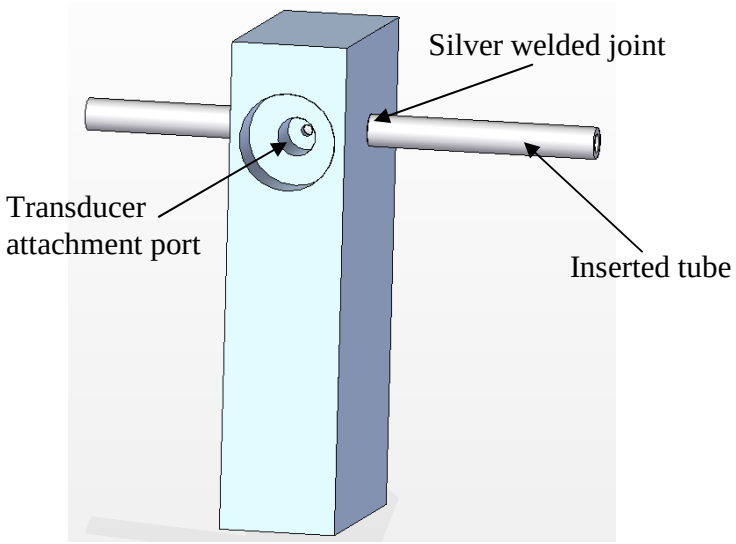

Figure 24: Transducer stand after tube insertion and welding

2.5.4 Stagnation Pressure Measurement

This will be achieved by directing flow into a fixed pressure transducer located at the gun exit facing the direction of the flow. The transducer will be attached to a stand as shown in figure 25 below, and the stand will be fixed onto the shock tube rig base.

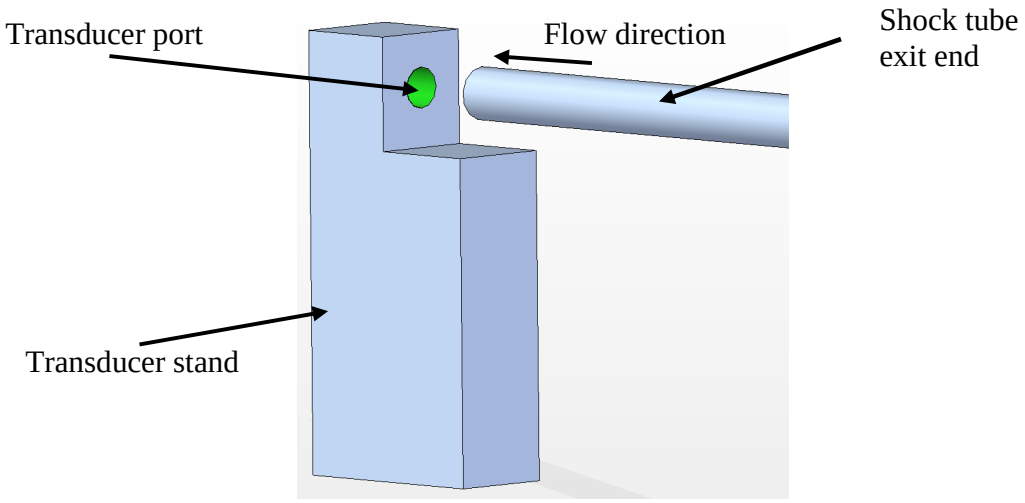

Figure 25: Stagnation pressure transducer stand

2.5.5 Valve Selection

Solenoid valves were selected to act as diaphragms in the rig due to their rapid opening reaction time. The selected valves have an orifice size of 6mm; this is 1mm larger than the tube itself. A bigger orifice will help facilitate faster flow through the valves. The specifications of the valves are attached in appendix B.

2.5.6 Structural Analysis

2.5.6.1 Reservoir Analysis

The analysis of the reservoir will be made at the design condition of maximum pressure loading, which is when the reservoir is subjected to 50 Bar of pressure loading.

a) Loading on the side plates (longitudinal loading)

As shown in figure 26 below the connection rods are subjected to tensile loading. The loading in each rod will be calculated as follows:

Reservoir side area = πr^2

= 0.007854 m^2

Reservoir side force = P×A

$= 50Bar \times 0.007854$

= 39270 N

It should be noted that there are four rods holding the reservoir side plates (reservoir stands) and the centre pipe together. Assuming that the rods share the load equally, each rod will be holding a force 9.8175 kN.

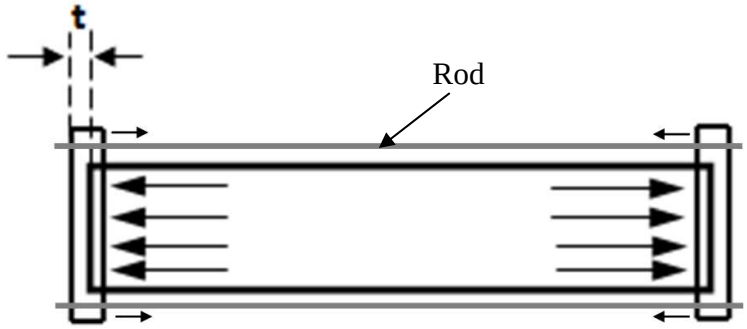

Figure 26: Side plate and rods pressure loading

Rod area = πr^2

= 0.0003142 m^2

Rod loading = 31.25 MPa

With yield strength of 350 Mpa, the rods have a safety factor of 11.2.

b) Radial loading

Using equation 11, $t = \frac{pdD}{2[\sigma_Y + pdY]}$, $(t \leq D/6)$, Y = 0.4 – 0.7 and

$(t \succ D/6)$, $Y = \frac{d + 2c}{D + d + 2c}$

A Y factor value of 0.4 from table 1 was found to be applicable.

$$t = \frac{5000000 \times 0.05}{2[350000000 + 5000000 \times 0.4]}$$

t = 0.355 mm

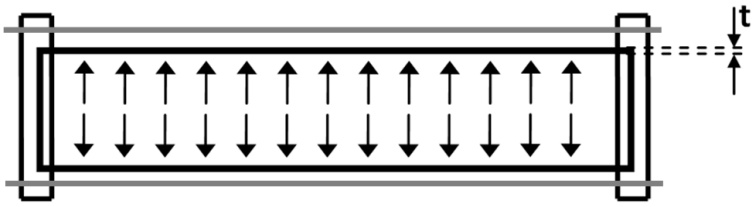

Figure 27: Reservoir radial pressure loading

A safe pipe thickness is 0.355 mm, however the pipe used in the design is 5 mm. This makes the structure to have a safety factor of 14.

2.5.6.2 Tube Analysis

The tube's D/6 value is less than the tube thickness, which makes the Y factor to be calculated as shown below.

$$t = \frac{pdD}{2[\sigma_Y + pdY]}\ ,\ (t \succ D/6)\ ,\ Y = \frac{d + 2c}{D + d + 2c}$$

Assuming mechanical allowances of 7.

$$Y = \frac{0.005 + 2 \times 7}{0.05 + 0.005 + 2 \times 7}$$

$$= 0.996$$

$$t = \frac{pdD}{2[\sigma_Y + pdY]}$$

$$t = \frac{5000000 \times 0.008}{2[350000000 + 5000000 \times 0.996]}$$

t = 0.056 mm

A safe pipe thickness is 0.056 mm, however the pipe used in the design is 1.5 mm. This makes the structure to have a safety factor of 26.6.

2.5.7 Control Circuit

A control circuit is required for the triggering of the solenoid valves. As shown in figure 28 the circuit diagram consists of the following components: a circuit breaker, a 24 Volts output transformer (power supply), a Moeller controller, a normally open switch and two solenoid valves. Detailed specifications of individual components are given in appendix B.

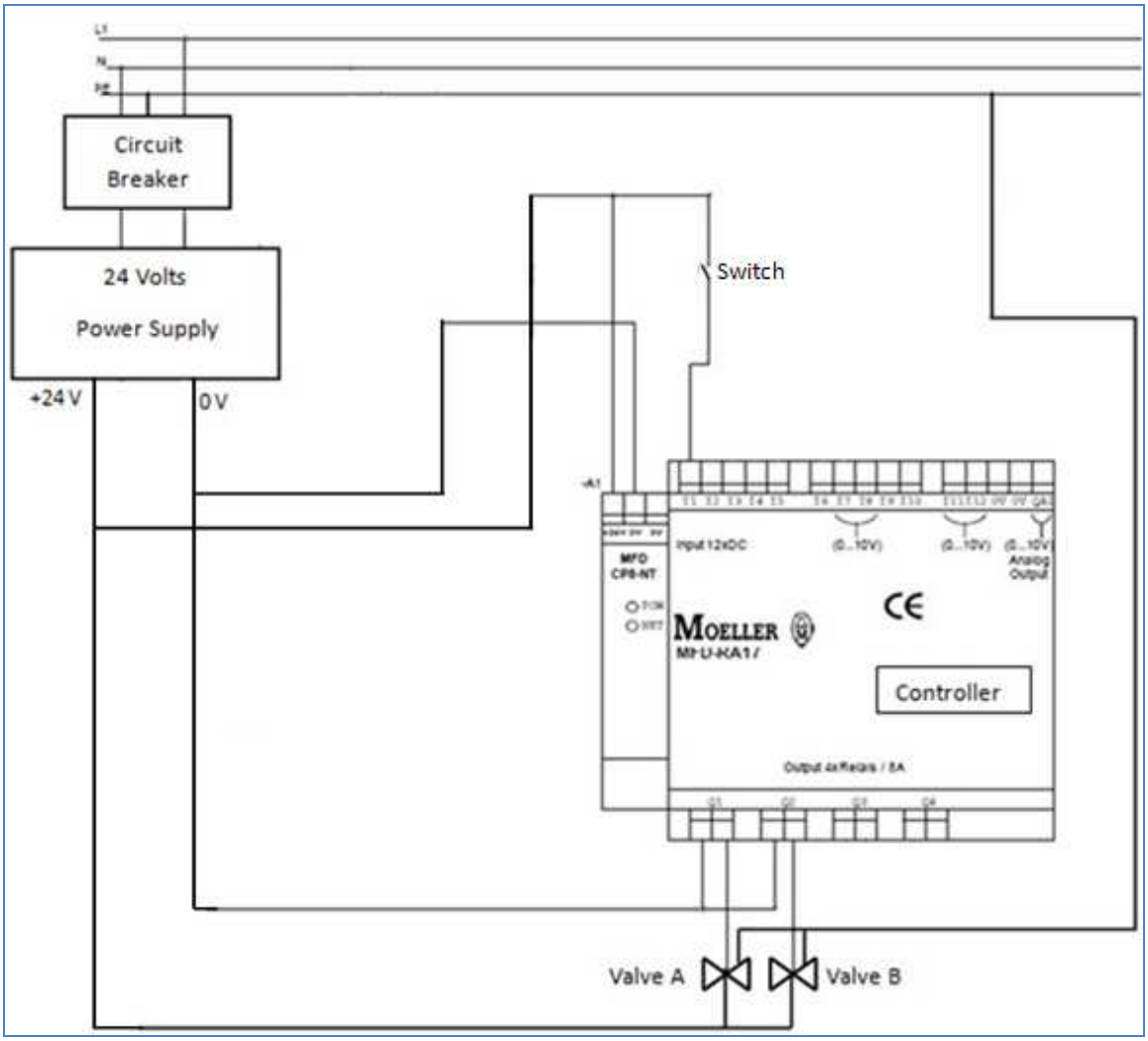

Figure 28: Valve control circuit diagram

2.5.8 Programming

The program makes use of two input basic units for both single and double valve arrangement programmes. One output basic unit is used for the single valve arrangement and two for the double valve, and a marker is used for each output. M markers also called marker bits or auxiliary relays are used to store the Boolean states 0 or 1. The program circuit diagrams also make use of a time relay. A timing relay can be used to simulate a timer function in which the switching times for the on and off switching of a switching contact can be changed.

In order for the timing relay to operate as a switch, it should be added in the circuit diagram as a contact (in the contact field). The timer function, i.e. the way in which a timing relay

controls the switching time, depends primarily on the mode configured. The time relay is used to set the opening and closing times of the solenoid valves. The configurable time relay delay times can be between 5 ms and 99 h 59 min. In the case where the valves have to open and close frequently, the flashing mode of the time relay function was used. The program circuit diagram for the single and double valve arrangements are shown in figures 29 and 30.

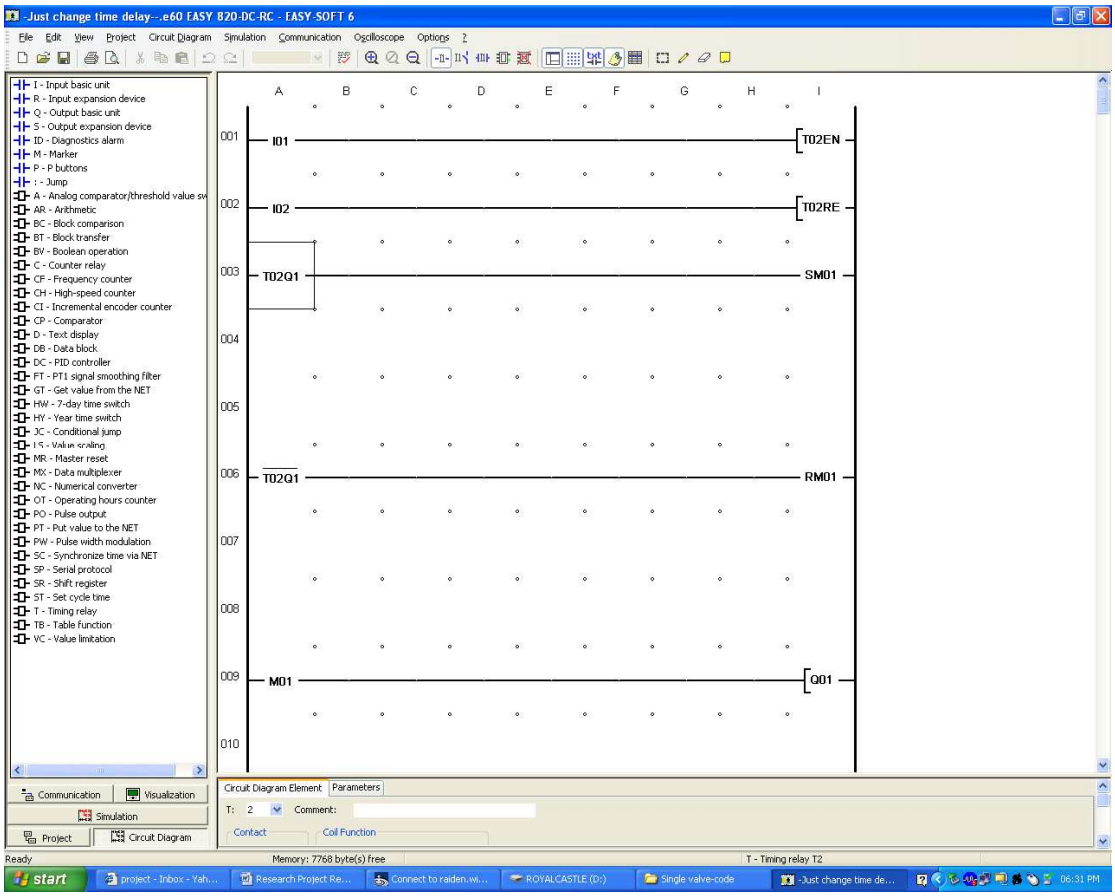

Figure 29: Single valve arrangement program circuit diagram

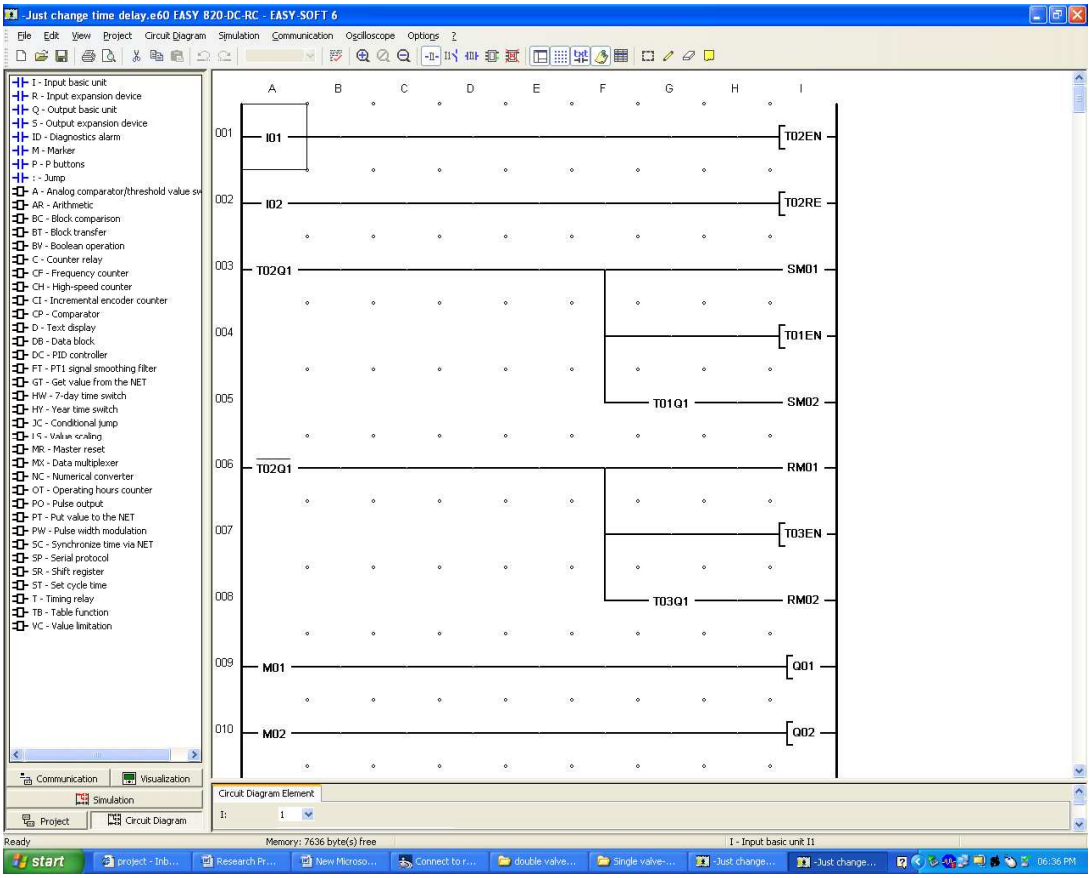

Figure 30: Double valve arrangement program circuit diagram

2.6 Design Description

The 5mm internal diameter shock tube is welded to transducer stands which are assembled on a thick base assembly plate. The thick base assembly plate, welded sections and the bolted transducer bases will give good rigidity to the rig. The rig accommodates both the single and double valve arrangements. For the single valve arrangement the shock generator, reservoir connector and the second valve of the rig are removed and replaced with one long single tube which extends from the first valve to the reservoir, as shown in the figures 31 and 32.

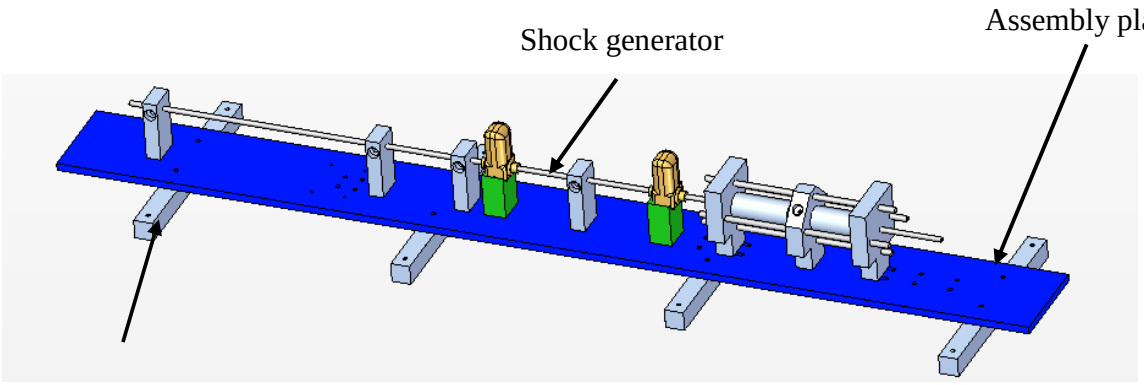

Figure 31: Double valve arrangement setup

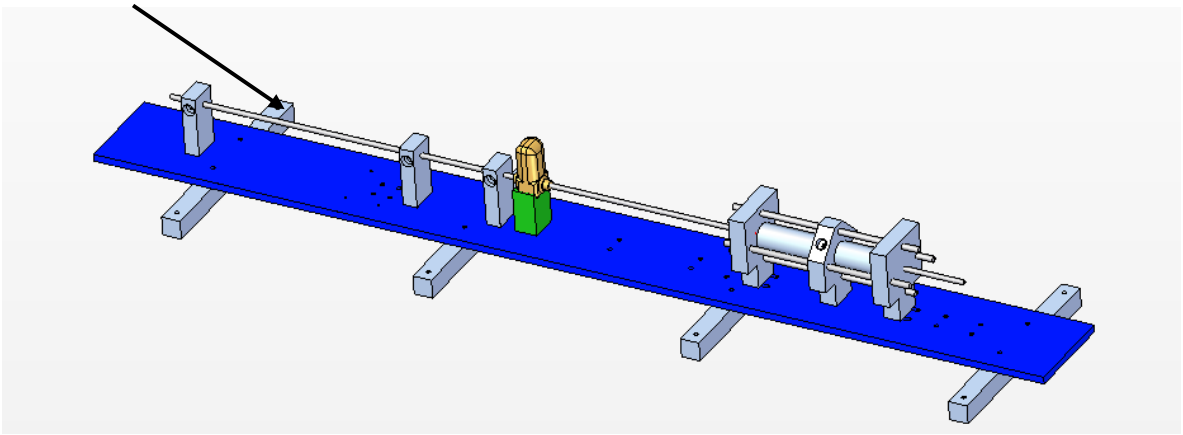

Figure 32: Single valve arrangement setup

2.7 Powder Feeder Development

Once the pulsing system is operational, powder will have to be introduced into the compression chamber. A proposed mechanism to introduce the powder is shown in figure 33. The powder feeder design consists of a hopper, a timing valve and a vibrating motor. The powder will be kept inside the hopper and transmitted into the shock tube through the timing valve. The vibrating motor is to help facilitate the flow of powder. Detailed drawings of the powder feeder are shown in appendix A. More development of the powder feeding mechanism will be conducted once the pulsing system is in operation.

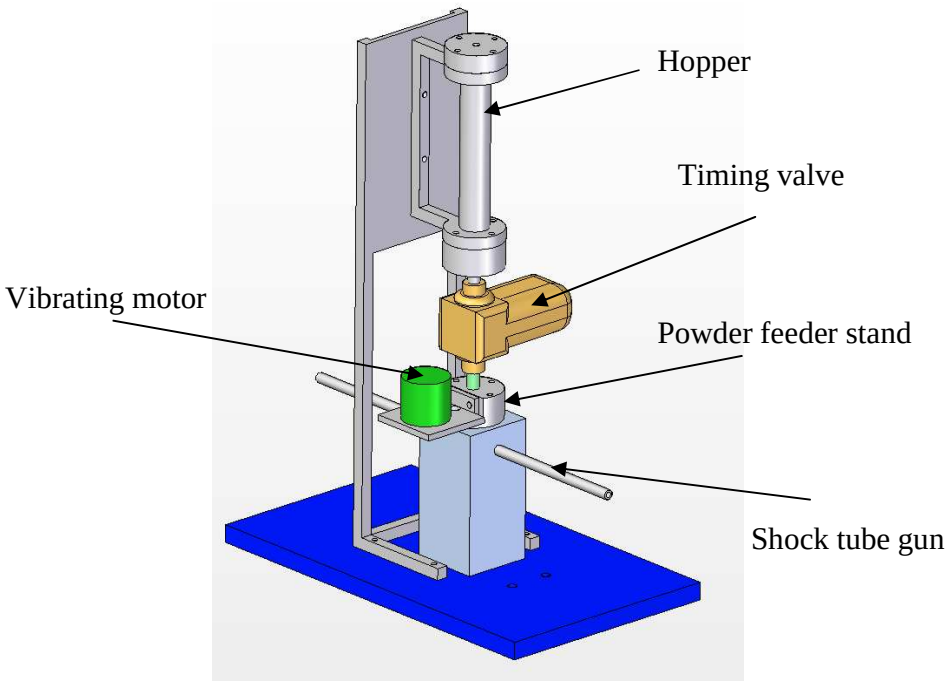

Figure 33: Powder feeder design

2.8 Final Design

The figure below shows an assembly of the final design. Components and sub assemblies are given in appendix A.

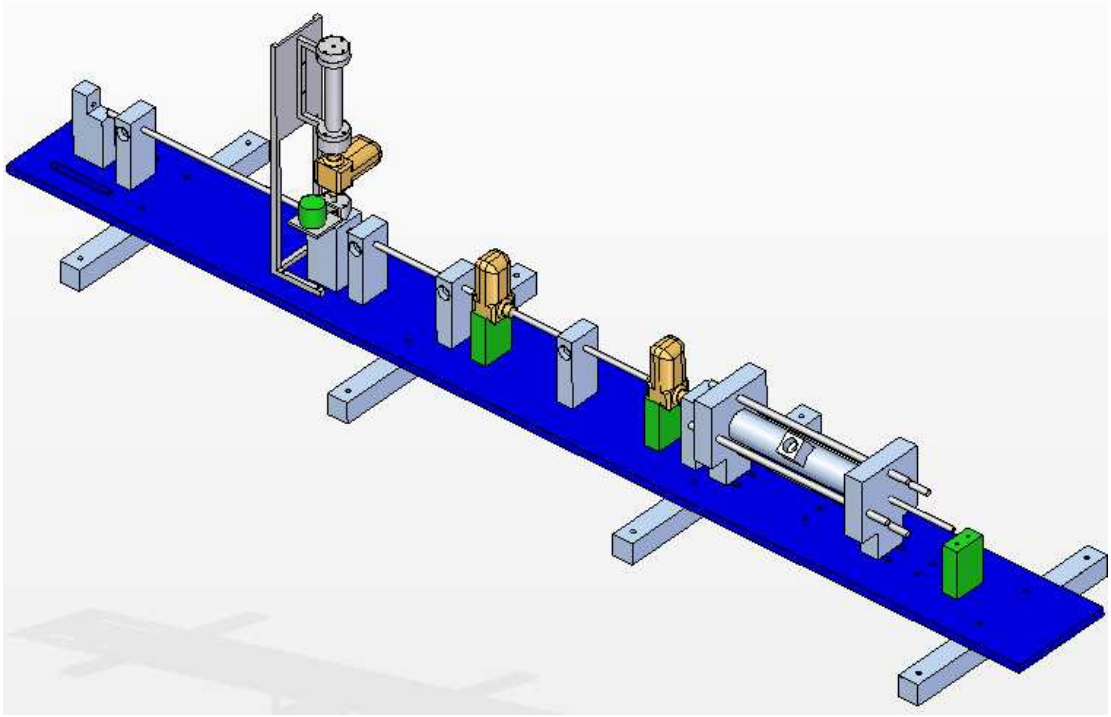

Figure 34: Final design assembly drawing

2.9 Shock Tube Rig Specifications

Reservoir volume: 0.377 liters

Shock generator volume: 6.872 *ml*

Gun Volume: 14.73 *ml*

Tube internal diameter: 5*mm*

Valves opening time: 100 *ms*

Valves closing time: 100 *ms*

Valves voltage supply: 24 V

Transducer connection ports sizes: M10×1

Shock generator length: 350 *mm*

Gun length: 750*mm*

Total length of shock tube: 1.4 *m*

Chapter 3 Apparatus

3.1 Consumables

3.1.1 Pressure Cylinder

Air and helium gas cylinder fitted with a pressure regulator are used. There is also a stop valve on the tube between the regulator and the reservoir. Gas cylinder specifications are shown in appendix B.

3.2 Hardware

3.2.1 Pressure Transducers

PCB pressure transducers were used to sense the static pressure in the shock tube. The following pressure transducers models were used: 113A21, 113A23and 113A24. The transducer specifications are shown in appendix B.

3.2.2 Data Acquisition System

The Graphtec data capturing system is used. The system consists of a data capturer and a laptop computer with the required software. Signals picked up by the transducers are first amplified before being send to the data capturer, the system is shown in figure 35. The pressure traces picked by the data acquisition system were saved as CSV files, which were further processed with Matlab software package.

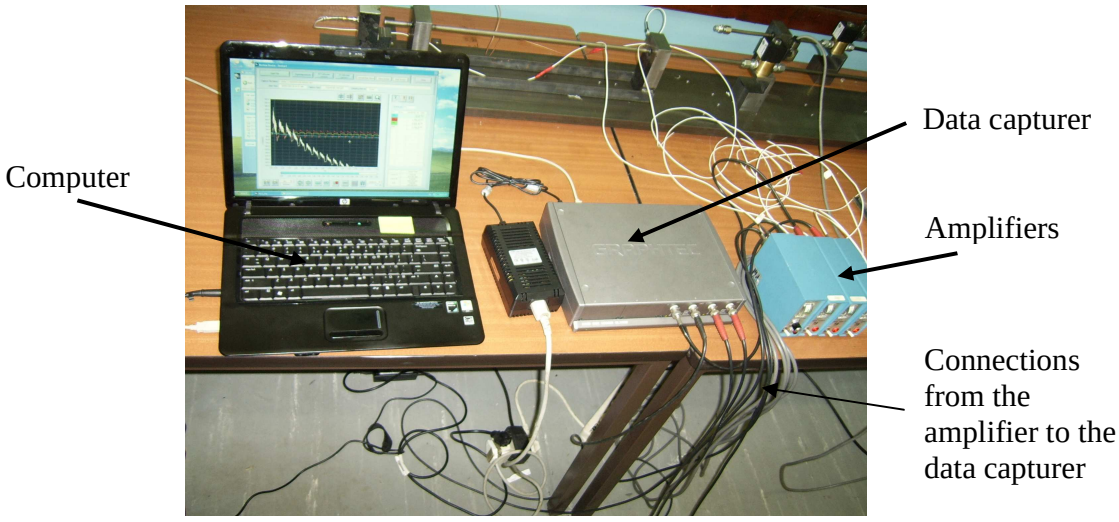

Figure 35: Data acquisition system

3.2.3 Solenoid Valves

Solenoid valves which are going to act as shock tube diaphragms are used. The solenoid valves have an orifice of 6mm and an opening and closing time of 100 *m*s. Valve specifications are shown in appendix B.



Figure 36: Solenoid valves

3.2.4 Controller

The opening and closing of the valves is to be controlled using a Moeller controller. The controller can be programmed from a desktop computer using the Easy Soft Ver. 6.20 Pro software. The Moeller controller specifications are shown in appendix B.

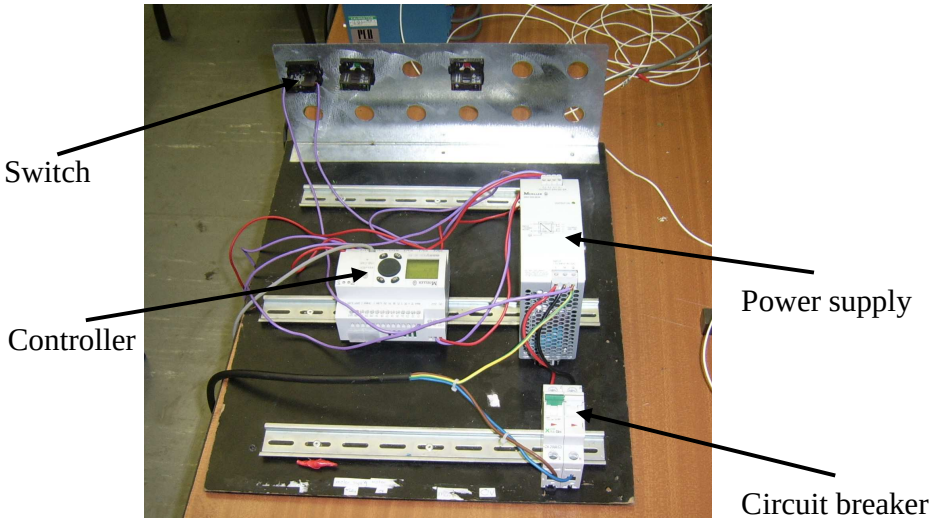

Figure 37: Valves control circuit

3.2.5 Pressure Transducer Identification

Four pressure transducers were used in the experiment: two 113A21, one113A23 and one 113A24.The transducers will be named and positioned as shown in figure 38. The pressure transducer traces were identified in the following way; the blue colour represents the shock generator pressure, the red colour is the transducer immediately after the second valve, the green colour is the transducer at the gun mouth exit and the white colour is the stagnation pressure as the exit.

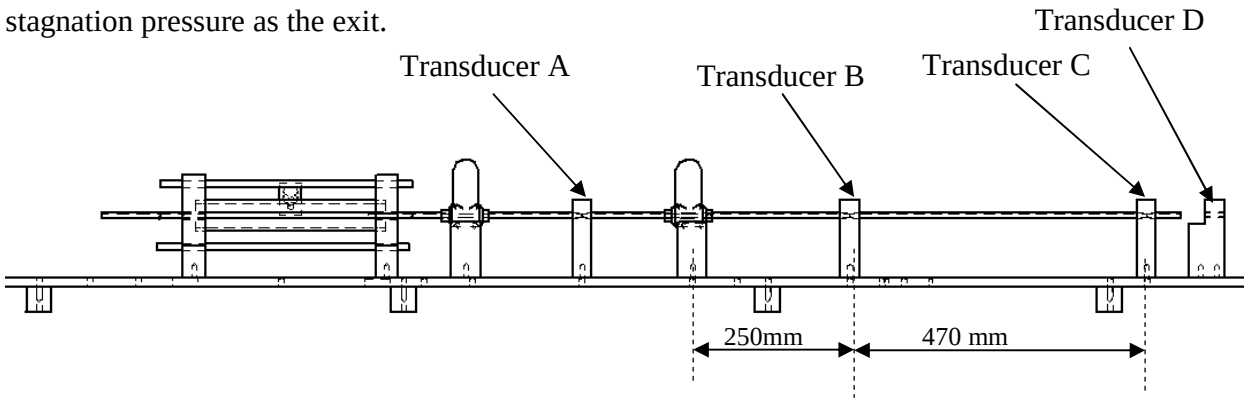

Figure 38: Transducer Identification

3.2.6 Rig Assembly

All of the components mentioned above are assembled and arranged as shown in figure 39.

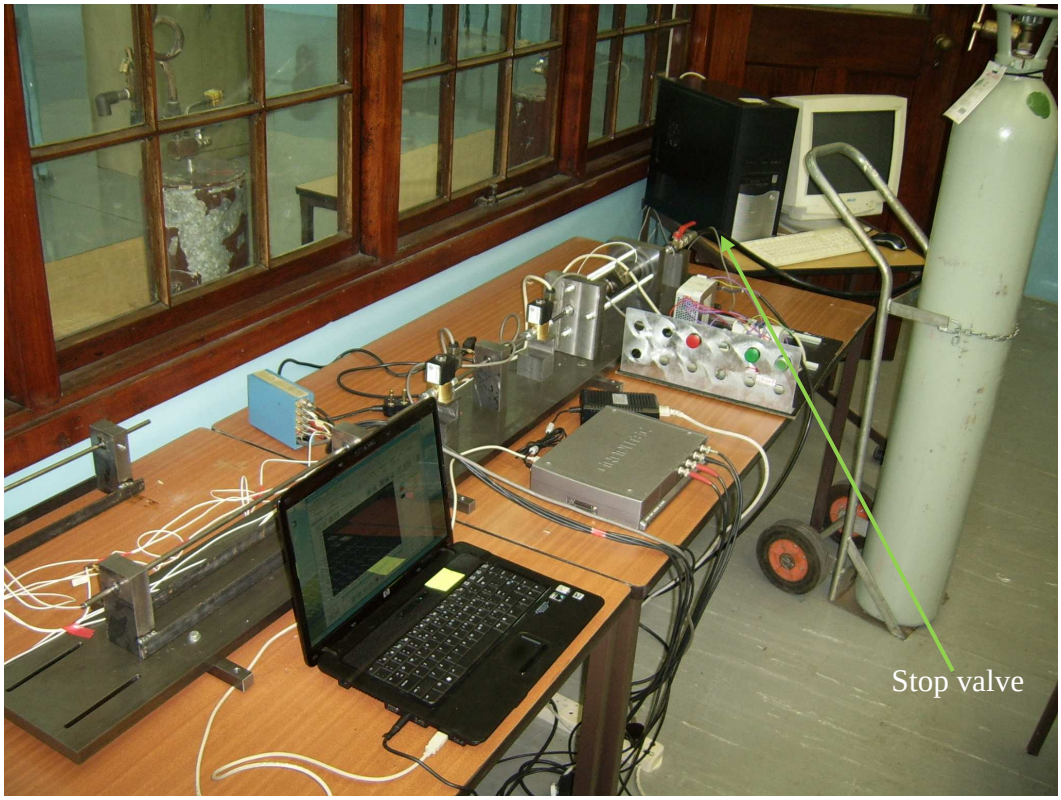

Figure 39: Shock tube rig components assembly

3.3 Software

a) Kasimir Software

The software is used for shock tube flow simulations

b) Easy Soft Ver. 6.20 Pro software

The software is used to control the opening and closing of the solenoid valves. The opening and closing frequency of the valves can also be adjusted.

c) Graphtec software

This is a data capturing software for the data acquisition system.

d) Matlab 7 software

The software is used for data processing.

Chapter 4 Methodology

4.1 Investigation Methodology

All tests were performed at room temperature over a reservoir pressure range of 10 and 50 bar in increments of 10 bar. The pressure reservoir will be tested at the pressure range of 10 to 50 bar increments of 10 bars. The analysis of the different valve arrangements and different gas drivers were done in the following order:

4.1.1 Double Valve Arrangement: shock wave strength tests

4.1.1.1 Analysis with Helium Gas as the Driver

a) Kasimir simulation (theory):
   - Assuming air is occupying the intermediate chamber

b) Experimental analysis

4.1.1.2 Analysis with Air gas as the Driver

a) Kasimir analysis (theory).

b) Experiment analysis

4.1.2 Single Valve Arrangement: shock wave strength tests

4.1.2.1 Analysis with Helium Gas as the Driver

a) Kasimir simulation (Theory)

b) Experimental analysis

4.1.2.2 Analysis with Air as the Driver

a) Kasimir simulation (Theory)

b) Experimental analysis

4.1.3 Single Valve Arrangement: variable opening frequency test

4.1.3.1 Analysis with Air as the Gas Driver

a) Experimental analysis

4.1.3.2 Analysis with Helium as the Gas Driver

a) Experimental analysis

4.1.4 Single Valve Arrangement: gas pre-heating test

4.1.4.1 Analysis with Air as the Gas Driver

a) Kasimir simulations (Theory)

4.1.5 Double Valve Arrangement: gas pre-heating

4.1.5.1 Analysis with Air as the Gas Driver

a) Kasimir simulations (Theory)

4.2 Procedure

4.2.1 Experimental Procedure

4.2.1.1 Shock Wave Strength Tests: Single and double valve arrangement

1) Firstly open the pressure cylinder valve slightly with every other valve closed (this is done so that the reading of the outgoing pressure on the regulator can be obtained).
2) Adjust the pressure regulator to a setting of 10 Bar.
3) Open the stop valve to fill up the reservoir
4) Take the pressure reading from the reservoir sensed by the first pressure transducer (This value should be the same as the pre set out put pressure on the pressure regulator).
5) Fire the tube:
    a) In the case of the single valve arrangement: open the valve (diaphragm), and close it after the tube has fired.
    b) In the case of double valve arrangement: open the entry valve of the shock generator; very shortly after that, open the exit valve.
    Very shortly after opening the exit valve and the tube has fired close the entry valve followed by closing the exit valve.
6) Record the peak pressure readings from the second, third and fourth pressure transducers.
7) The reservoir should have a continuous supply of pressure from the cylinder to ensure a constant set pressure in the reservoir; this is especially in the case where multi pulses are fired.
8) Close both the stop valve and the pressure cylinder valve.
9) The steps above should be repeated for all the different set pressures which are to be tested.

4.2.1.2 Wave Generation Frequency Testing: single valve arrangement

1) First set the valve opening and closing frequency at 5 Hz
2) Similarly to the testing procedure above, open the pressure cylinder valve slightly with every other valve closed.

3) Adjust the pressure regulator such that the outgoing pressure is at 10 Bar.
4) Open the stop valve to fill up the reservoir.
5) Take the pressure reading from the reservoir sensed by the first transducer
6) Open and close the isolation (diaphragm) valve for 1second.
7) Close both the stop valve and the pressure cylinder valve.
8) Repeat the above steps for the valve opening frequency of 10 Hz and 20 Hz.
9) The steps above should be repeated for all the different set pressures which are to be tested.

4.2.2 Kasimir Simulations

For the procedure followed when running simulations, refer to figure 40 below.

1) First enter the number of sections that the shock tube is divided into
2) Enter the end time of the simulation
3) Enter the initial conditions of the tube: a) compression chamber gas type, pressure, and temperature, b) expansion chamber gas type, pressure, and temperature.
4) Select the time triggered valve opening option and specify the triggering time.
5) Specify the dimensions of the tube: diameter, section lengths and the tube end type.
6) Finally enter the ambient pressure and temperature conditions surrounding the tube.

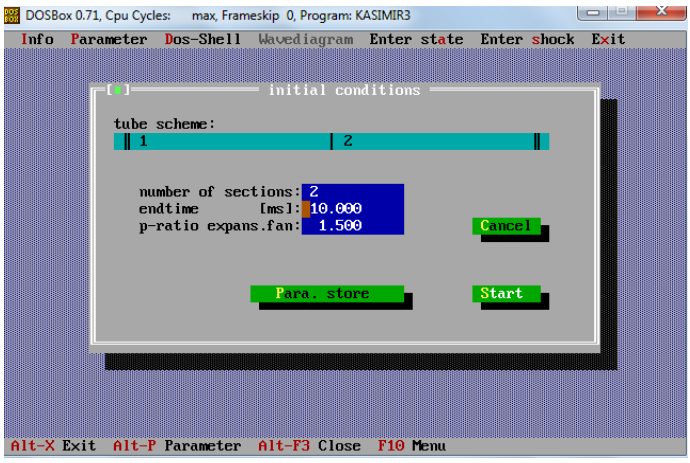

Figure 40**: Kasimir simulation tube specifications screen with two sections (1 and2)**

4.3 Precautions

The following precautionary measures should be adopted when conducting the experiments:

1) Pressure vessels should be kept in a dry cool and secure area. Ensure that cylinders are secured
2) Ensure that the pressure rating of the solenoid valve is not exceeded.
3) Ensure that the correct voltage and current are send to the valves and the controller to avoid burning them out.
4) Hearing protection should be worn at all times to avoid hearing loss due to the loud noise created by the jet exiting the gun.
5) There should be no obstruction in front of the gun exit.
6) Ensure that the transducers are kept safe and well protected on the rig.

Chapter 5 Results

5.1 Sample Calculations and Pressure Measurement

5.1.1 Theoretical Calculation of the Shock Strength: double valve arrangement

The sample calculations in this section are based on a case where there are two valves (diaphragms) in the shock tube, with one valve opening a short time after the other. In these calculations the high pressure and temperature obtained at the end of the primary shock wave are calculated. The obtained pressure and temperature conditions are then used as an input to quantify the further increase in temperature and pressure of the reflected shock. The conditions of the reflected shock are then used as initial conditions in the secondary shock wave. The secondary shock wave is what finally drives the spraying powder out of the spraying gun.

5.1.1.1 Generation of the Primary Shock Wave

The calculations were made using the following initial conditions with Helium as the gas driver:

Compression chamber

Medium: Helium gas	
Pressure (P_4)	30 Bar
Temperature (T_4)	294 K
Sound Speed ((a_4)	1008 m/s
Specific heat ratio (γ_4)	1.67

Expansion chamber

Medium: Air	
Pressure (P_1)	0.83 Bar (Atmospheric)
Temperature (T_1)	294 K
Sound Speed (a_1)	343.14 m/s
Specific heat ratio (γ_1)	1.4

Equation 2 is used to evaluate the static pressure in region two as shown in figure 12 above and equation 3 is used to calculate the static temperature of the region. Equations 6 and 7 are used to calculate the shock wave velocity and the gas velocity behind the shock respectively.

Pressure:

$$P_2 = P_4\left[1-\frac{(\gamma_4-1)\left(\frac{a_1}{a_4}\right)\left(\frac{P_2}{P_1}-1\right)}{\sqrt{2\gamma_1\left\{2\gamma_1+(\gamma_1+1)\left(\frac{P_2}{P_1}-1\right)\right\}}}\right]^{\frac{2\gamma_4}{\gamma_4-1}}$$

$$P_2 = 30\left[1-\frac{(1.67-1)\left(\frac{343.14}{1008}\right)\left(\frac{P_2}{0.83}-1\right)}{\sqrt{2(1.4)\left\{2(1.4)+((1.4)+1)\left(\frac{P_2}{0.83}-1\right)\right\}}}\right]^{\frac{2(1.67)}{1.67-1}}$$

P_2 **= 7.714 bar**

Temperature:

$$T_2 = T_1\left[\frac{P_2}{P_1}\frac{\left[\left(\frac{\gamma+1}{\gamma-1}\right)+\frac{P_2}{P_1}\right]}{\left[1+\left(\frac{\gamma+1}{\gamma-1}\right)\frac{P_2}{P_1}\right]}\right]$$

$$T_2 = 294\left[\frac{7.717}{0.83}\frac{\left[\left(\frac{1.4+1}{1.4-1}\right)+\frac{7.714}{0.83}\right]}{\left[1+\left(\frac{1.4+1}{1.4-1}\right)\frac{7.714}{0.83}\right]}\right]$$

T_2 **=736.6 K**

Shock wave velocity:

$$V_S = a_1\sqrt{\frac{\gamma+1}{2\gamma}\left(\frac{P_2}{P_1}-1\right)+1}$$

$$V_S = 343\sqrt{\frac{1.4+1}{2(1.4)}\left(\frac{7.714}{0.83}-1\right)+1}$$

V_S **= 977.1 m/s**

Gas velocity behind the shock wave:

$$V_2 = \frac{2\left(M_S{}^2 - 1\right)}{(\gamma+1)M_S}a_1$$

$$V_2 = \frac{2\left(2.85^2 - 1\right)}{(1.4+1)2.85}343.14$$

$V_2 =$ **714 m/s**

The following values were obtained for the given initial conditions.

Calculated Results

Pressure (P_2)	7.714 bar(gauge)
Temperature (T_2)	684 K
Gas velocity (V_2)	714 m/s
Shock velocity (V_S)	977 m/s

5.1.1.2 Reflected Wave Conditions

The calculation was made using final conditions of the initial (primary) shock wave as the initial conditions of the reflected shock.

Initial conditions

Medium: Air	
Pressure	7.714 bar
Temperature	684 K
Gas velocity (V_2)	714 m/s
Sound Speed @ 684K	524.24 m/s

The moving reflected shock can be modelled as a stationary shock with gas flowing across it. When modelled as stationary the reflected shock divides the flow across it into the x and y components. The x component is downstream of the shock and the y component is

upstream of the shock. Conditions in the y component represent the high temperature and pressure conditions of the reflected shock. The moving and stationary shocks are shown below.

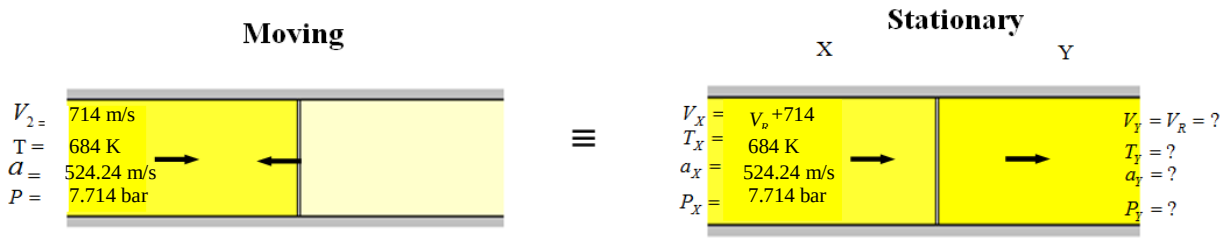

From the above, table 3 below is generated. The table shows Mach numbers for the x component obtained from the compressible flow tables and the Mach number obtained by calculations (using gas dynamic equations). The corresponding velocity ratio of the two components (x and y) will be found at the point where the two Mach numbers (from tables and calculations) converge. Once the velocity ratio is established conditions of component y can be calculated. Different values of reflected wave velocity (V_R) will be substituted (iterative process) until the Mach number values converge.

Table 3: Iterative process to find the conditions of the reflected shock

Number of Iterations	V_R	V_X	$\frac{V_Y}{V_X} = \frac{V_R}{V_R + 777}$	From tables: M_X	Calculated: $M_X = \frac{V_X}{a_X}$
1	200	914	0.2188	4.00	1.7435
2	250	964	0.2593	3.00	1.8353
3	270	984	0.2743	2.79	1.8734
4	280	994	0.2817	2.69	1.8961
5	300	1014	0.2959	2.54	1.9533
6	340	1054	0.3225	2.31	2.0105
7	360	1074	0.3352	2.23	2.0486
8	380	1094	0.3474	2.15	2.0868
9	390	1104	0.3532	2.12	2.1059
10	393	1107	0.3550	2.11	2.1116
11	395	1109	0.3561	2.10	2.1154
12	400	1114	0.3591	2.09	2.1249

From the above table the M_X value is 2.11 and the corresponding M_Y value is 0.5598. Using the temperature and pressure ratios at the point the following pressure and temperature conditions were obtained on the reflected shock:

$$\frac{T_Y}{T_X} = 1.7789 \qquad \frac{P_Y}{P_X} = 5.0274$$

Final conditions of the reflected shock

Pressure ($P_{4'}$)	38.78 bar
Temperature ($T_{4'}$)	1216.76 K

5.1.1.3 Generation of the Secondary Shock Wave

Once again the final conditions of the reflected shock are used as the initial conditions when generating the secondary shock (final shock).

Initial conditions

Medium: Helium

Pressure ($P_{4'}$)	38.78 bar
Temperature ($T_{4'}$)	1216.76 K
Specific heat ratio (γ_4)	1.67

Once again equation 2 is used to evaluate the static pressure in region two and equation 3 is used to calculate the static temperature of the region. Once the strength of the secondary shock is found, the velocity behind the shock is found using equation 7.

Pressure:

$$P_2 = P_4 \left[1 - \frac{(\gamma_4 - 1)\left(\frac{a_1}{a_4}\right)\left(\frac{P_2}{P_1} - 1\right)}{\sqrt{2\gamma_1\left\{2\gamma_1 + (\gamma_1 + 1)\left(\frac{P_2}{P_1} - 1\right)\right\}}} \right]^{\frac{2\gamma_4}{\gamma_4 - 1}}$$

$$P_2 = 38.78 \left[1 - \frac{(1.67 - 1)\left(\frac{343.14}{1008}\right)\left(\frac{P_2}{0.83} - 1\right)}{\sqrt{2(1.4)\left\{2(1.4) + ((1.4) + 1)\left(\frac{P_2}{0.83} - 1\right)\right\}}} \right]^{\frac{2(1.67)}{1.67 - 1}}$$

P_2 = **8.602 bar**

Temperature:

$$T_2 = T_1\left[\frac{\frac{P_2}{P_1}\left[\left(\frac{\gamma+1}{\gamma-1}\right)+\frac{P_2}{P_1}\right]}{\left[1+\left(\frac{\gamma+1}{\gamma-1}\right)\frac{P_2}{P_1}\right]}\right]$$

$$T_2 = 294\left[\frac{\frac{8.602}{0.83}\left[\left(\frac{1.4+1}{1.4-1}\right)+\frac{8.602}{0.83}\right]}{\left[1+\left(\frac{1.4+1}{1.4-1}\right)\frac{8.602}{0.83}\right]}\right]$$

T_2 =**789.15 K**

Shock wave velocity:

$$V_S = a_1\sqrt{\frac{\gamma+1}{2\gamma}\left(\frac{P_2}{P_1}-1\right)+1}$$

$$V_S = 343\sqrt{\frac{1.4+1}{2(1.4)}\left(\frac{8.602}{0.83}-1\right)+1}$$

V_S = **1030.49 m/s**

Gas velocity behind the shock wave:

$$V_2 = \frac{2\left(M_S{}^2-1\right)}{(\gamma+1)M_S}a_1$$

$$V_2 = \frac{2\left(3^2-1\right)}{(1.4+1)3}343.13$$

V_2 = **762.51 m/s**

The following values were obtained for the given initial conditions.

Calculated Results

Pressure ($P_{2'}$)	8.602 bar
Temperature ($T_{2'}$)	789.15 K
Gas velocity ($V_{2'}$)	762.51 m/s
Shock velocity (V_S)	1030.49 m/s

NB: Velocities for different pressure ranges are simulated using Kasimir. The simulations give the theoretically expected values for the different compression chamber pressures. The simulations are run for both the single and double valve arrangements. The Kazimir wave diagrams for different pressures are shown in appendix E.

5.1.2 Technique of Measuring the Shock Strength from Experiments

The velocity of the shock is calculated using transducers B and C as explained in section 3.2.5. The pressure trace of transducer B is shown by the blue colour and the pressure trace of transducer C is shown by the green colour. The dotted line in figure 41 denotes a single pulse created by a shock wave travelling across the transducers, in a single valve arrangement tube. In this case the frequency was set a 5 Hz and the reservoir pressure was set at 30 Bar.

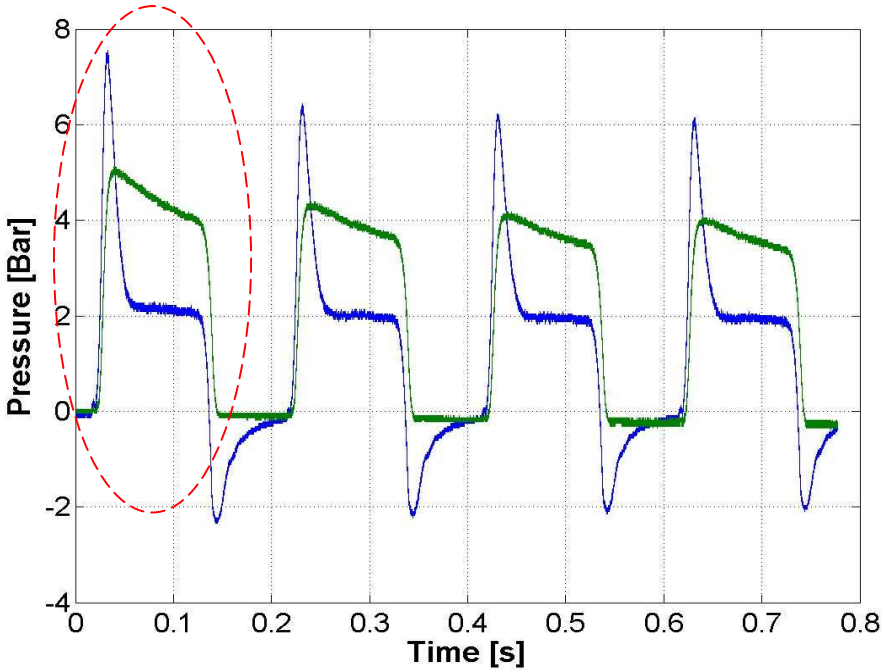

Figure 41: Pressure history for transducers B and C, single valve arrangement at 5Hz and 30 bar pressure supply

Zooming into the figure to show one pulse, the rise time of the transducers can clearly be seen. During the rise time (denoted by the dotted line in figure 42 below) the curves have certain gradients. Using the gradients of the curves the point of inflection can be located. The point of inflection on the curves is the point where the gradient reaches its maximum value and starts to decrease. The point of inflection represents the time when the pressure transducers experience maximum flow, which is the time when the shock wave travels across it.

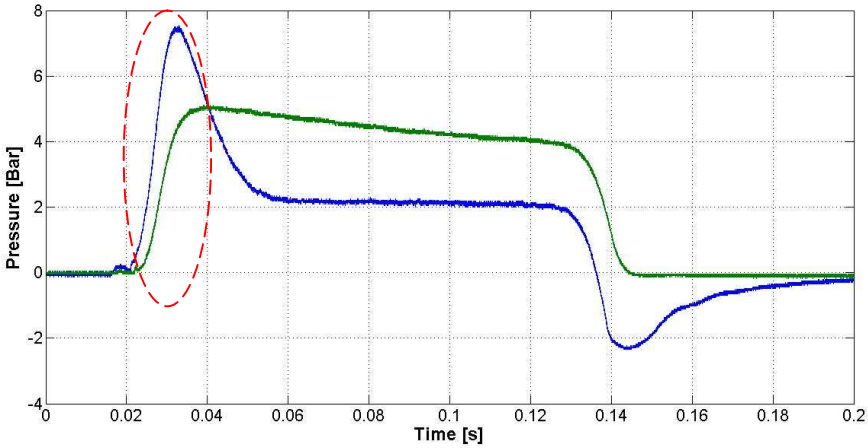

Figure 42: Enlargement of a single cycle from figure 41.

5.1.3 Flow Velocity Behind the Compression Wave

The flow in the tube is isentropic, at 30 bar reservoir pressure, single valve arrangement

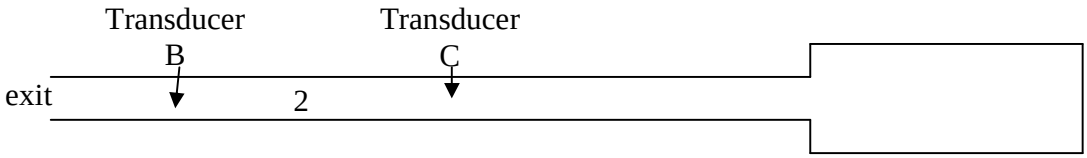

Calculating the pressure and Mach number at position 2 (Skews, 2008)

$$\frac{P_2}{P_1} = \left(\frac{T_2}{T_1}\right)^{\frac{\gamma}{\gamma-1}}$$

$$\frac{P_2}{6.045} = \left(\frac{T_2}{297}\right)^{\frac{1.4}{0.4}}$$

$$p_2 = p_{static+}\, p_{dynamic}$$

$$p_2 = \frac{5.07 + 7.02}{2} + \frac{1}{2}\rho_2 (522.94)^2$$

$$p_1 = \rho_1 R T_1$$

Reservoir pressure [Bar]	Compression Wave Velocity	P_2	T_2	ρ	γ
30	552.94	16.13	390.4	7.265	1.4

Mach number of the compression wave (Skews, 2008)

$$\frac{P_0}{P} = 2.61$$

$$M_2 = 1.25$$

$$a_2 = \sqrt{1.4 \times 287.1 \times 390.4}$$

= 396.13 m/s

$$v_2 = 1.25 \times 396.13$$

= 495.16 m/s

Reservoir pressure [Bar]	Compression Wave Velocity	Mach Number	P_2	T_2	Flow Velocity
30	552.94	1.25	16.13	390.4	495.16

5.1.4 Impact Velocity Sample Calculation

The transducer located 30 mm downstream of the gun exit facing the flow was used to read the stagnation pressure at the point. The stagnation pressure is then used to calculate the flow impact velocities. Calculations for both the below and above sonic conditions are shown below. The assumption made is that the pressure upstream of the bow shock is ambient. The flow Mach number upon impact is calculated by finding the ratio of the stagnation pressure and the ambient pressure.

$$v = \sqrt{\gamma R T_2 M^2}$$

$$v = \sqrt{1.4 \times 287.1 \times 300.92 \times 1.02^2}$$

$$v = 354.74 \text{m/s}$$

Reservoir pressure [Bar]	Voltage[V]	P_0	$\frac{P_0}{P}$	M	$\frac{T_2}{T_1}$	Impact Velocity
30	0.525	160.58	1.935	1.02	1.0132	354.74

5.2 Plots of Results

Tables of observations and results for tests on different valve arrangements and valve opening frequency are shown in appendix B. The tables of observations and results are for both the experimental data and Kasimir simulations for Air and He as gas drivers. The results obtained are plotted in this section.

5.2.1 Single Valve Arrangement

The figures below show the change in compression wave velocity, velocity of the flow behind the compression and the flow impact velocity with the change in reservoir pressure for the single valve arrangement.

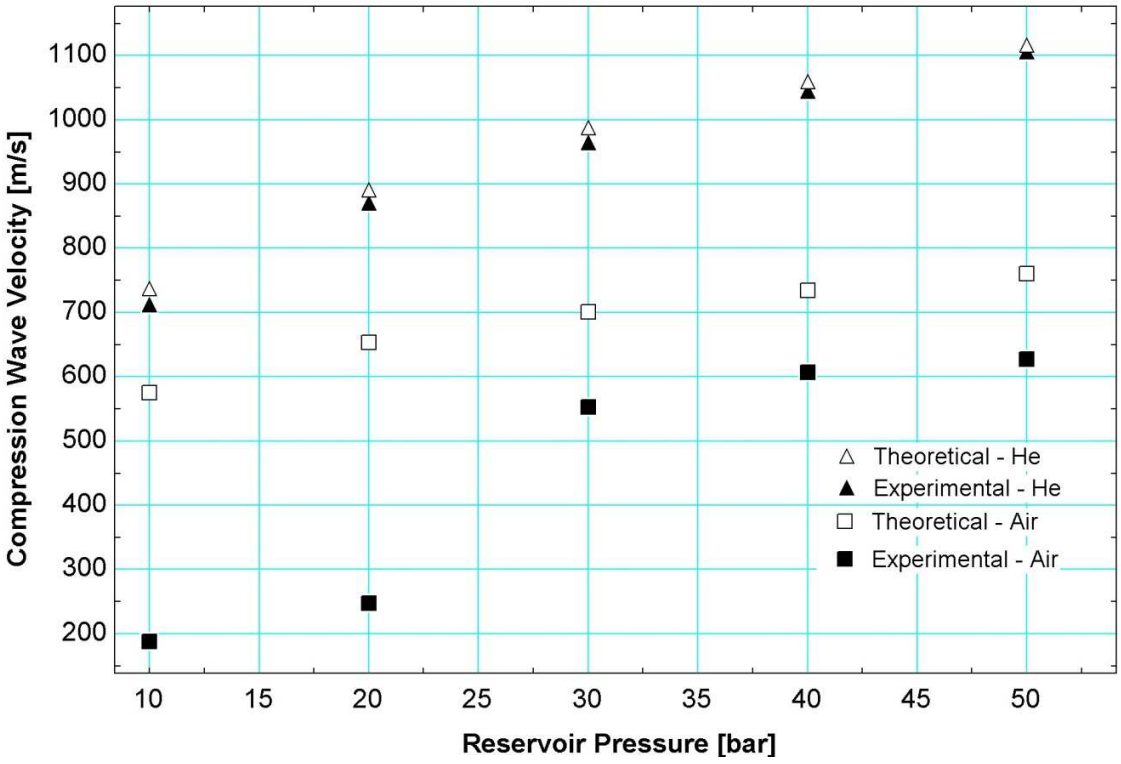

Figure 43: Compression wave velocity change with the change in reservoir pressure: Single valve

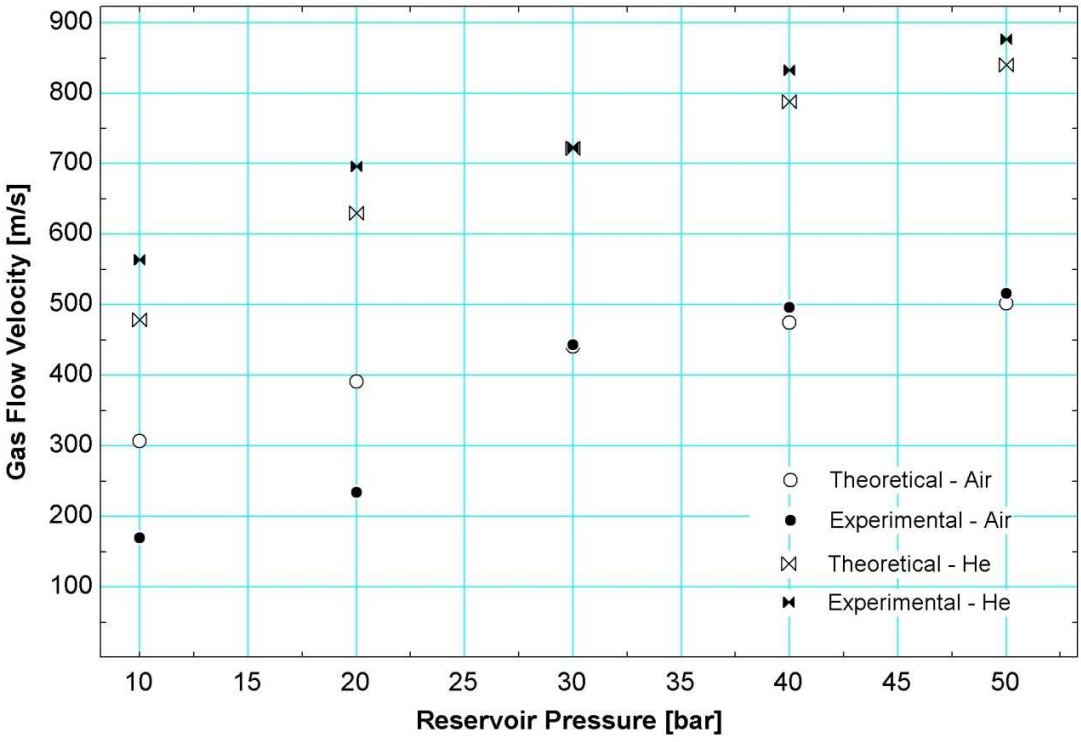

Figure 44: Gas flow velocity behind the compression wave change with change in reservoir pressure

5.2.2 Double Valve Arrangement

The figures below show the change in compression wave velocity and the velocity of the flow behind the compression wave with the change in reservoir pressure for the double valve arrangement.

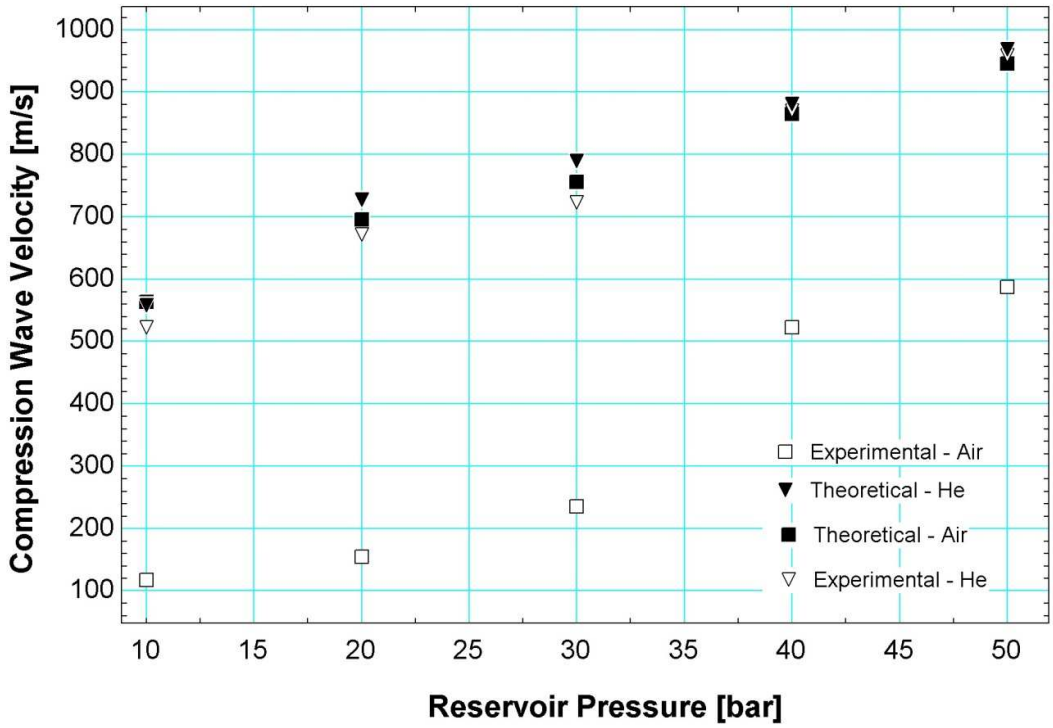

Figure 45: Compression wave velocity change with the change in reservoir pressure: Double valve

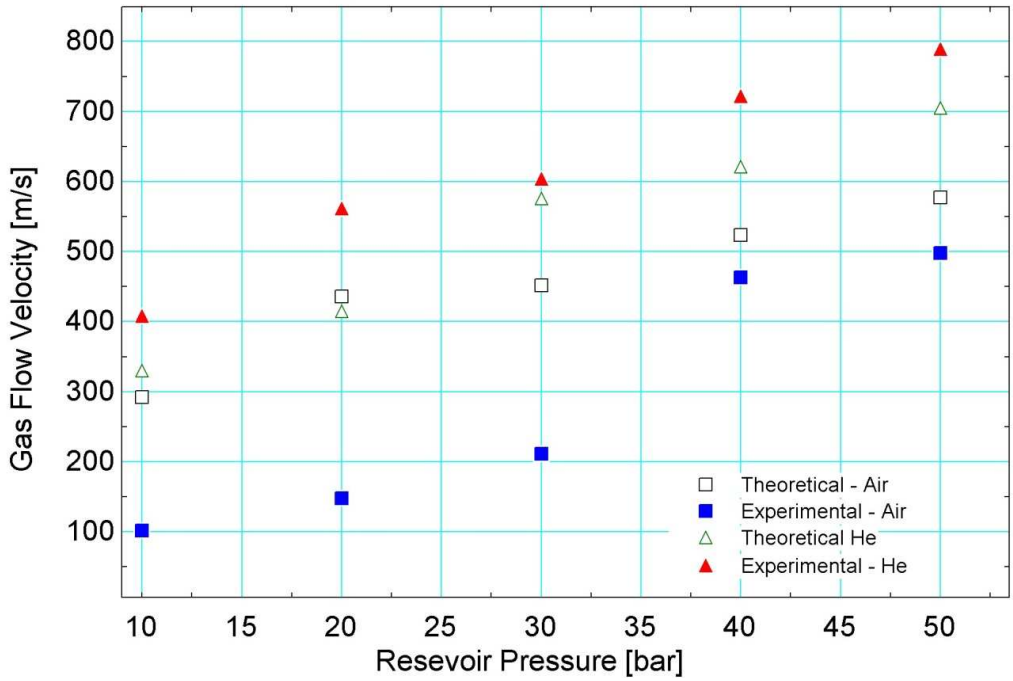

Figure 46: Gas flow velocity behind the compression wave change with change in: Double valve

5.2.3 Multiple Valve Opening Frequency

The figure below shows the change in velocity of the flow behind the compression wave with the change in reservoir pressure for the single valve arrangement. The plot shows the flow velocities for valve opening frequencies of 5, 10 and 20 Hz.

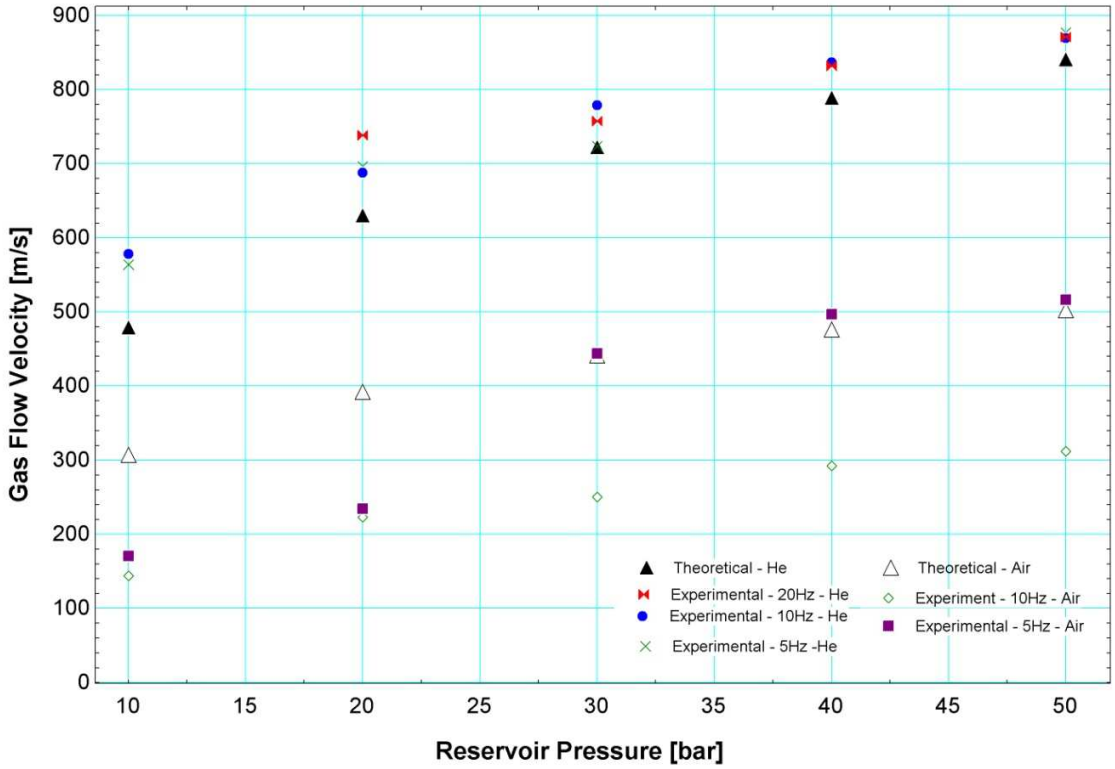

Figure 47: Multiple valve opening frequency: 5Hz, 10Hz and 20Hz.

5.2.4 Flow Substrate Impact Velocity

The figure below shows the change in flow impact velocity at the exit of the tube with the change in reservoir pressure for both the single and double valve arrangement. The single valve arrangement plots show the flow velocities for valve opening frequencies of 5, 10 and 20 Hz.

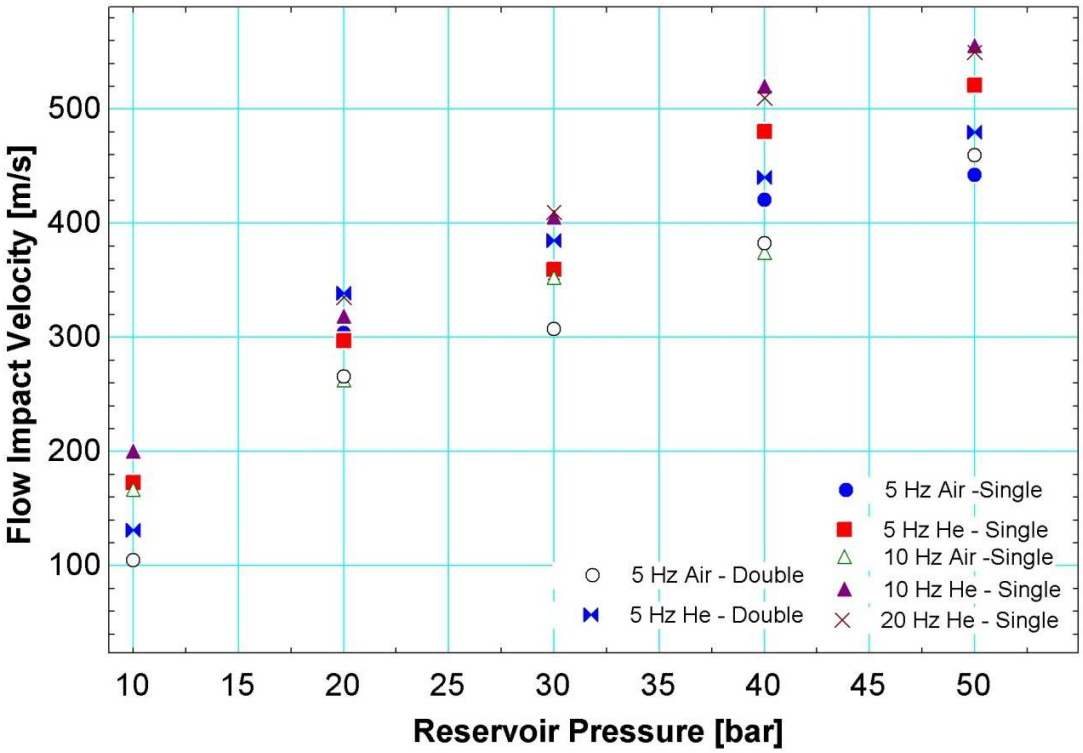

Figure 48: Flow impact velocity with change in pressure

5.2.5 Flow Pressure Pulses

The figures below show flow pressure variations from transducers B and C generated at 5, 10 and 20 Hz frequencies. The pressure traces are for a reservoir pressure of 30 Bars.

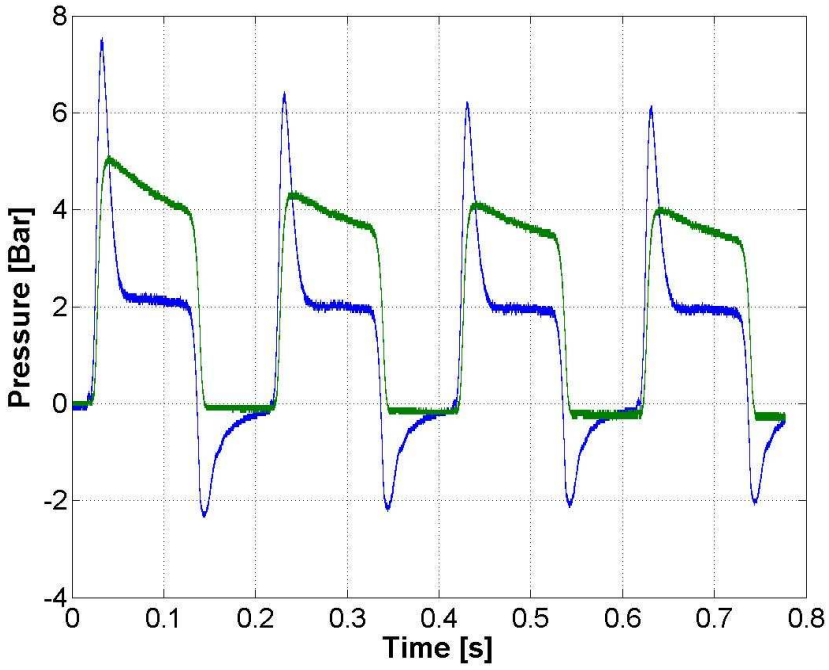

Figure 49: Pressure variation with change in time with air as the driver gas: 5Hz

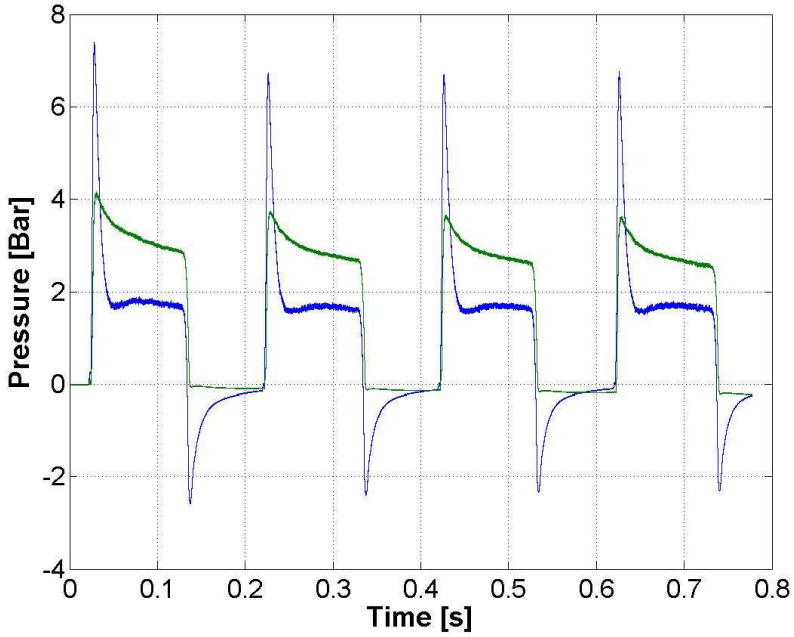

Figure 50: Pressure variation with change in time with helium as the driver gas: 5Hz

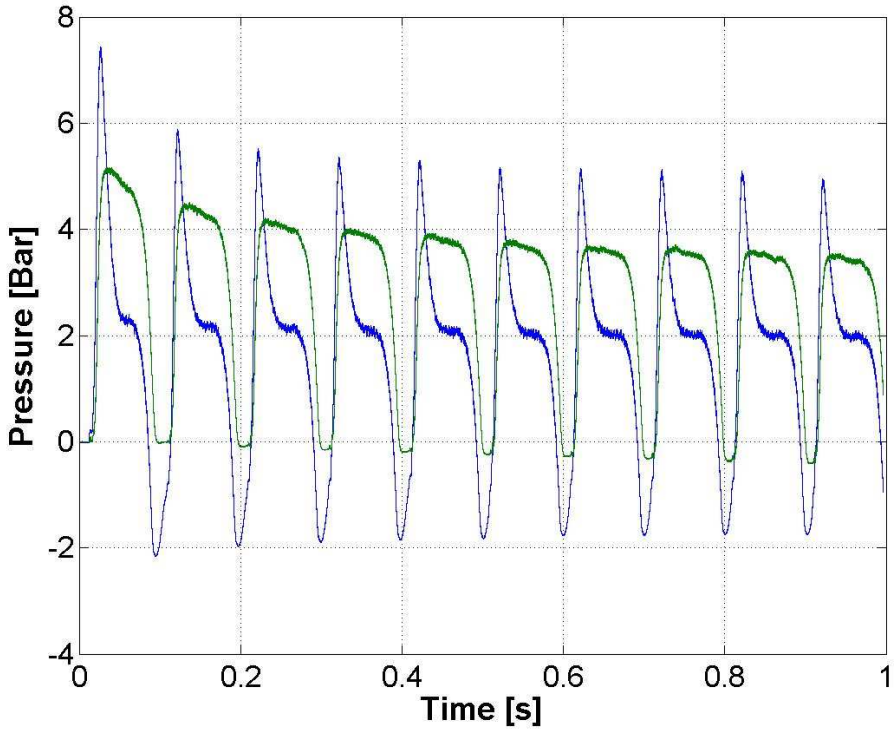

Figure 51: Pressure variation with change in time with air as the driver gas: 10Hz

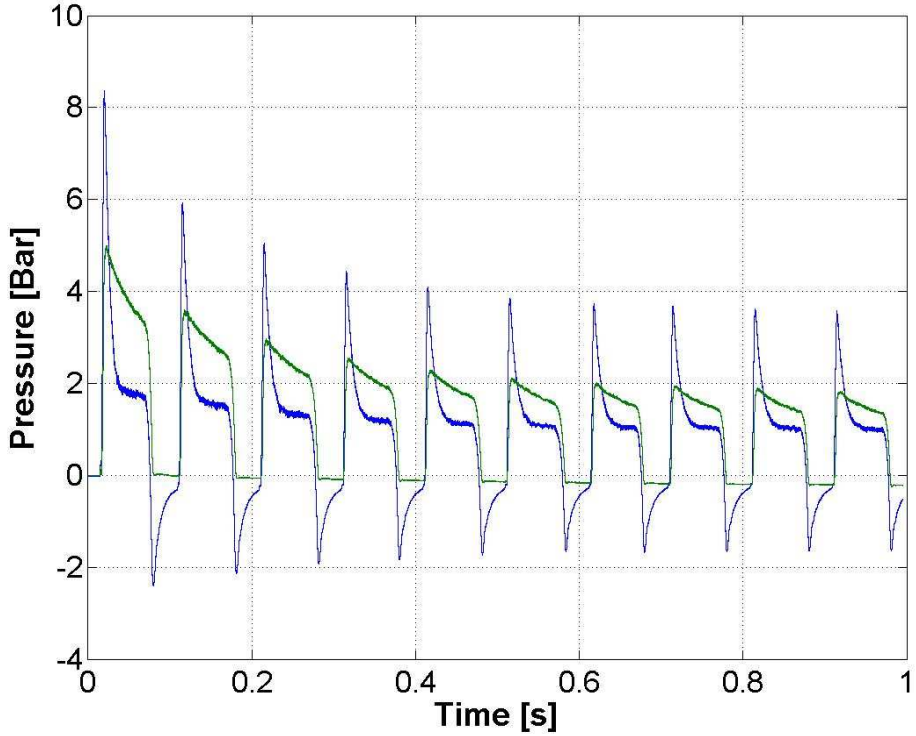

Figure 52: Pressure variation with change in time with helium as the driver gas: 10Hz

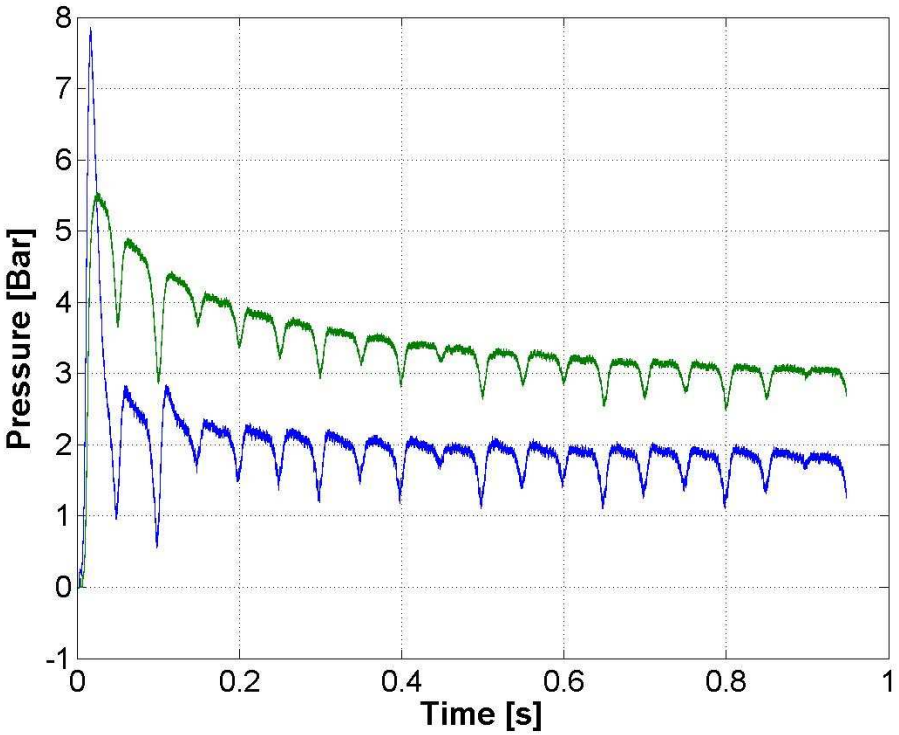

Figure 53: Pressure variation with change in time with air as the driver gas: 20Hz

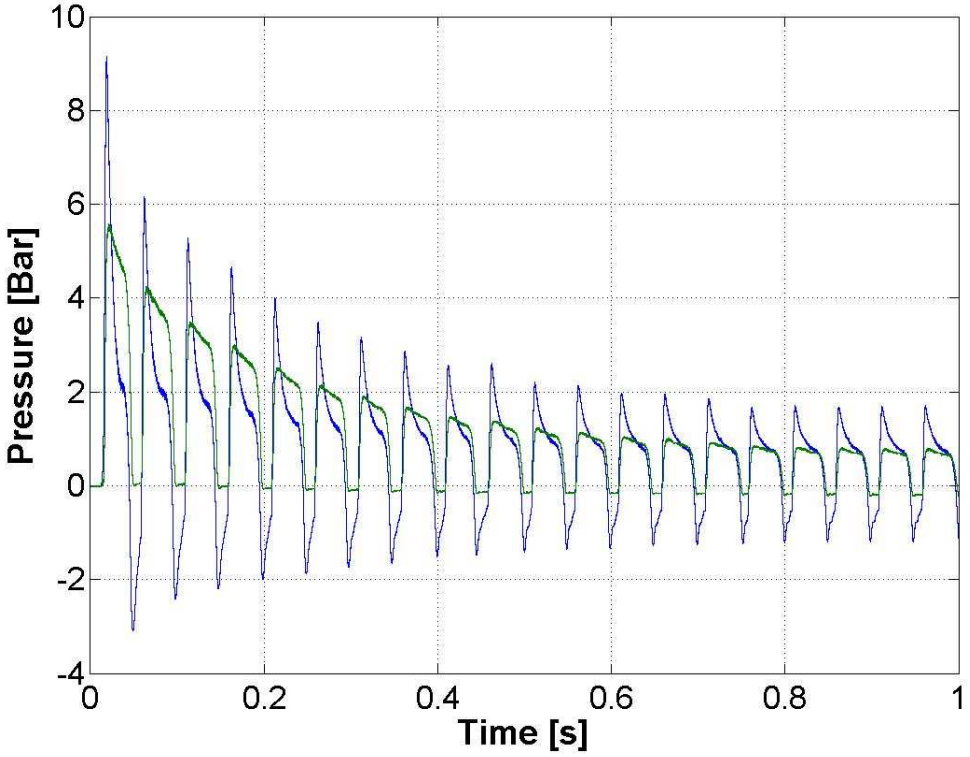

Figure 54: Pressure variation with change in time with helium as the driver gas: 20Hz

5.2.6 Double Valve Time Delay Diagnosis

During the testing it was suspected that the double valve arrangement's time delay of the second valve opening was not responding as required. The time delay dictates how long it will take before the second valve opens after the first one. The set time delay should show on the pulses detected by pressure transducers. As indicated previously, the blue colour represents the shock generator pressure, the red colour is the transducer immediately after the second valve, the green colour is the transducer at the gun mouth exit and the white colour is the stagnation pressure as the exit.

Tests were performed at a reservoir pressure of 5 bars to confirm if the suspicion was true or not and the results are shown in the figures below. Time delays of 100ms, 150 ms and 200ms were set. In all the cases there is supposed to be a time delay between the rise in pressure of the shock generator and the rise in pressure of the transducers downstream of the second valve. However, what is observed is that the pressure rise in the shock generator occurs almost instantaneously as the pressure rise in the downstream pressure transducers, irrespective of the time delay. This means that the second valve is opening before the time delay elapses.

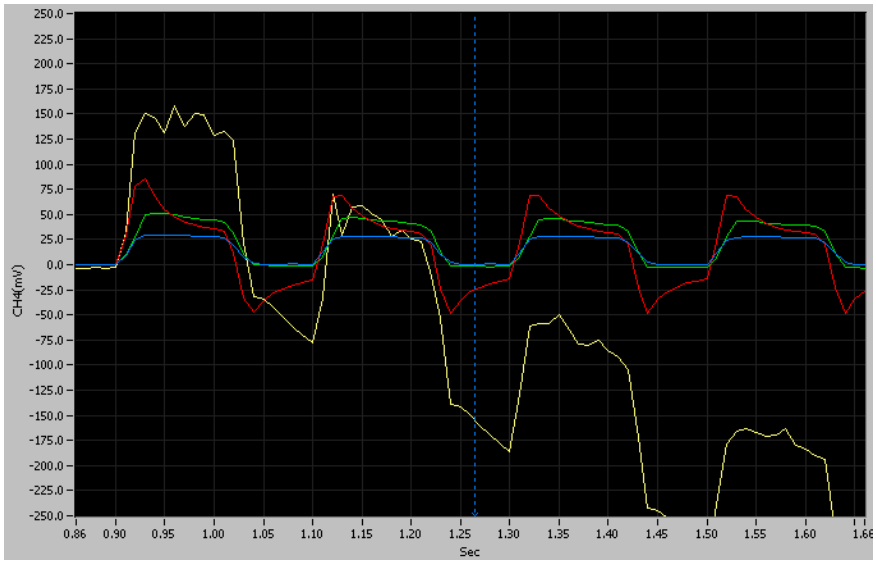

Figure 55: Pressure traces with 100*ms* time delay in the shock generator: 5 bar pressure reservoir

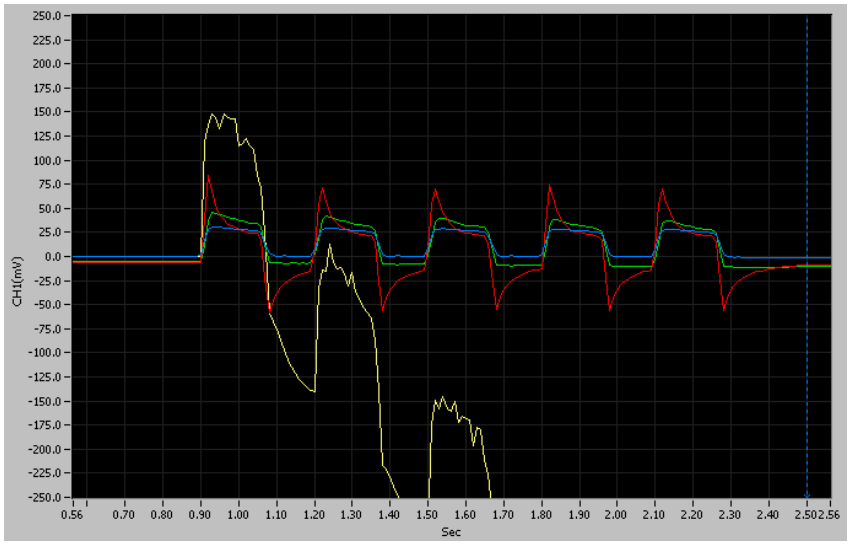

Figure 56: Pressure traces with 150*ms* time delay in the shock generator: 5 bar pressure reservoir

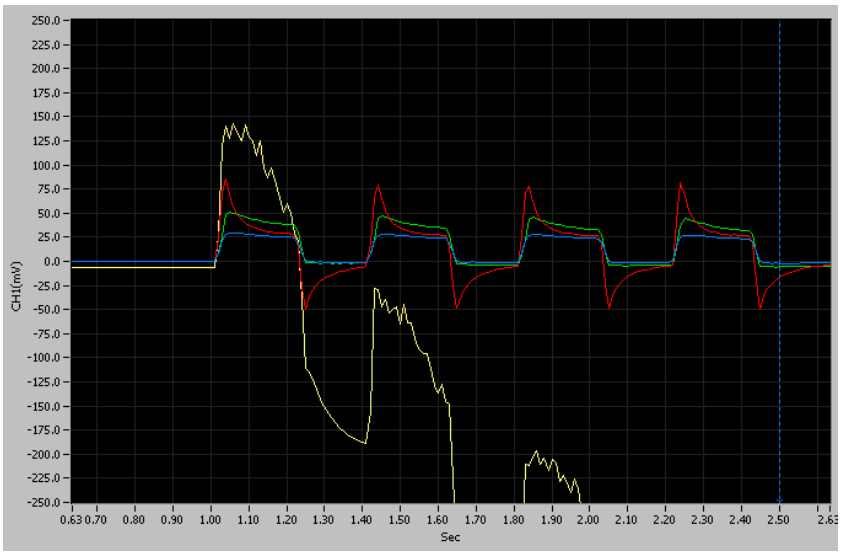

Figure 57: Pressure traces with 200*ms* time delay in the shock generator: 5 bar reservoir

5.2.7 Gas Pre-heating

Kasimir simulations were run with different gas pre-heat temperature, room temperature velocities were compared to a preheat temperatures of 200 ^{o}C and 400 ^{o}C. The pre-heat tests were done for both the single and double valve arrangement. The results obtained from the Kasimir simulations are given in figures 58 and 59:

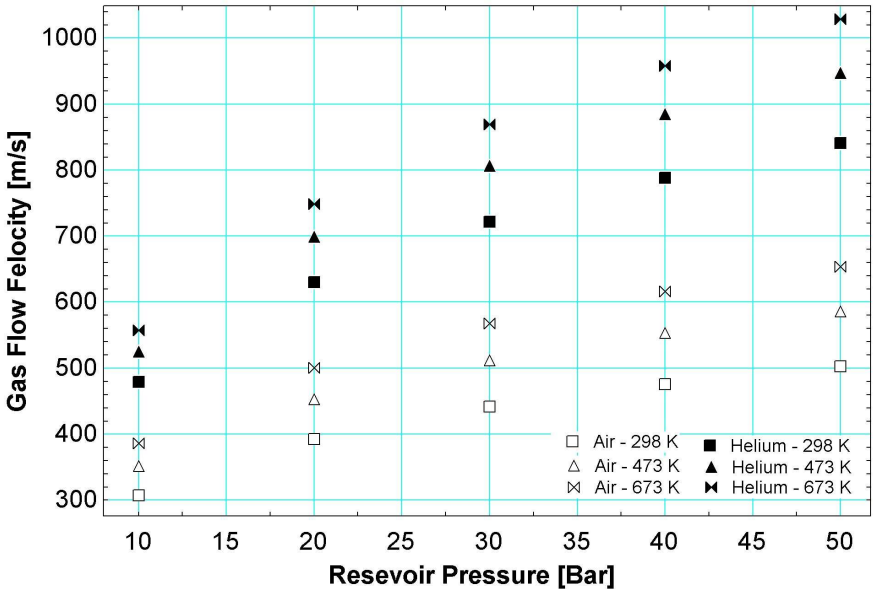

Figure 58: Pre-heated gas flow velocity: single valve arrangement

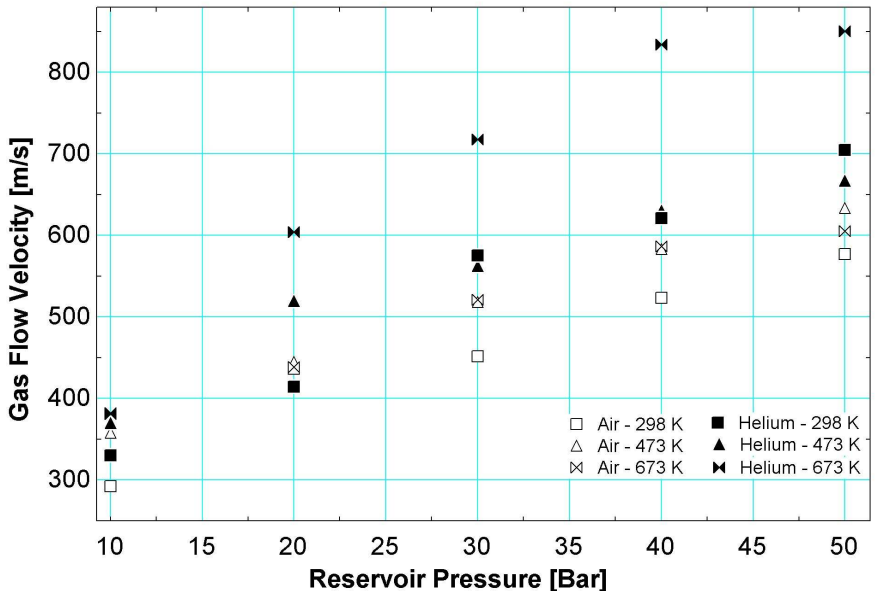

Figure 59: Pre-heated gas flow velocity: double valve arrangement

Chapter 6 Discussion

6.1 Shock velocity and velocity of the gas behind the shock

6.1.1 Single Valve Arrangements

Figures 43 and 44 show the variation in compression wave and gas flow velocity with changes in reservoir pressure for the single valve arrangement. The plots compare the theoretical values with the experimental ones obtained when one pulse is fired with valve opening and closing times of 100 *ms*. Theoretically (ideal conditions) for all the reservoir pressures within the tested range (10 to 50 bar) a shock wave should be formed for a helium gas driver. In the experiments supersonic compression waves were generated for all the helium cases, 10 to 50 bars of reservoir pressure. The compression wave velocities for helium were close to the theoretical values. Experimental compression wave velocities (Table 4) ranging from 712 *m/s* at 10 bar reservoir pressure to 1105 *m/s* at 50 bar were obtained. This is very close to the theoretical velocities (Table 7) of 736 *m/s* at 10 bar and 1116 *m/s* at 50 bar. Gas flow velocities behind the compression wave (Table 6) ranging from 563.84 *m/s* for 10 bar to 876.92 *m/s* for 50 Bars were obtained, which is also very close to the theoretical values (Table 7) of 478 *m/s* at 10 Bars and 840 *m/s* at 50 bar.

Theoretically, with air as the gas driver shock waves are expected to form over the tested range, shock wave velocities (Table 7) ranging from 574 *m/s* at 10 bar to 760 *m/s* at 50 bar were expected. However, in the experiment supersonic compression waves were only generated for reservoir pressures of 30, 40 and 50 bar, with the 50 bar reservoir pressure generating a shock wave velocity (Table 4) of 626 *m/s*. In the experiment jet flow velocities for the 10 and 20 bar reservoir pressures were below sonic conditions, with flow velocities (Table 5) of 170.36 *m/s* and 234.64 *m/s* respectively. The gas flow velocities behind the compression wave ranged from 170.36 *m/s* at 10 bar to 515.34 m/s at 50 bar, gas flow velocities were reasonably close to the theoretically expected values at higher reservoir pressures.

6.1.2 Double Valve Arrangement

Figures 45 and 46 shows the change in compression wave and gas flow velocity behind the compression wave with change in reservoir pressure for the double valve arrangement. The Kasimir simulations show the shock velocities for air and helium to be very close to one another, which is very different when compared to the single valve arrangement case. Shock velocities (Table 11) ranging from 563 *m/s* to 945 *m/s* were obtained for air and velocities ranging from 558 *m/s* to 969 *m/s* were obtained for helium when running the simulations at 10 to 50 bar of pressure. The greatest margin between the two gases is 4.6% at 20 bar, with helium having a slightly higher velocity.

Experimental jet velocities for helium deviate slightly from the theoretically expected values. The shock velocities are within 91.5% of the theoretical values. However, this is not the case with air jets, which are significantly lower than the theoretical values. The marginal difference for the air jets gets up to 500% (10 bar flow) from the theoretical values.

From the double valve arrangement diagnosis it was established that the second valve is opening almost instantaneously after the first valve irrespective of the set time delay. This means that the primary shock wave generated by the first valve forces the second valve to open. This is despite the maximum pressure rating of the valve (200 bar) being 40 times the tested pressure of 5 bar. The un-planned opening of the valve has to do with the valve design. The valves are normally closed single acting solenoid valves. This means that the solenoid opens the valve seat when activated and when not activated a spring acts on the valve seat to seal the valve. Under shock loading the spring is forced to open even if the design pressure rating of the valves is significantly higher that the tested pressure range.

6.2 Multiple Valve Opening Frequency Tests

6.2.1 Single Valve Arrangement

Figure 47 shows the change in gas flow velocity with reservoir pressure for different valve opening frequencies. The theoretical expected values are compared with the values

obtained during experimentation. Three opening frequencies of the valves were tested (5, 10 and 20Hz).
Helium experiments closely follow the theoretical values. These experiments are always within (Table 12) 85% of the theoretical value. This shows the experimental helium jets to be behaving almost as in the ideal shock tube for all three tested frequencies.

The figure only shows two frequencies for air (5 and 10 Hz) compared with the theoretical values, instead of three. This is because a different behaviour with air is observed for the three tested frequencies. The experimental jets (Table12) seem to be getting closer to the theoretically expected with the decrease in frequency, 5Hz frequency tests are always within 56% of the theoretical value and 10 Hz frequency tests are always within 47 % of the theoretical value. At 20 Hz the air jets do not have distinct pulses and the flow is almost continuous, hence the values for 20 Hz could not be obtained.

A valve opening frequency of 5 Hz coincides with the fastest time that the valves can be fully opened (100*ms*) and fully closed (100 *ms*). Increasing the frequency beyond the maximum designed time means that the valves do not fully open and close. Further reducing the frequency from 5 Hz will not affect the time of the valves opening and closing. At 10 Hz they open in 50*ms* and close in 50 *ms*, and this is further reduced to 25ms for 20 Hz. For this reason, fast moving air jets could not be formed since air flow is slower when compared to helium. Due to this fastness of helium, its jets are not affected by the reduced opening and closing times of the solenoid valves, however, air jets are significantly affected.

6.3 Flow Substrate Impact Velocity: single and double

Figure 48 shows the substrate impact velocity of the gas jet for different reservoir pressures, different valve arrangements and different gas drivers at different frequencies. Flow impact velocities obtained ranged from (Table 15 and 20) 105.31 *m/s* to 555.13 *m/s* for both single and double valve arrangement. At **5 Hz** of valve opening frequency the **single valve** arrangement velocities (Table 20) ranged from 172.75 m/s to 450.2 m/s for air and 172.8 m/s to 520.9 m/s for helium. This shows impact velocities of helium to be

always slightly higher than those of air. The difference in impact velocities of air and helium is much smaller in comparison with jet flow velocity difference inside the tube. This means that the helium jet gets significantly decelerated at the gun exit. The deceleration is attributed to helium having a lower density, which makes it easy for its gas particle to lose their momentum.

With a valve opening frequency of **5 Hz** the **double valve** arrangement velocities ranged from (Table 15) 105.31 m/s to 460.06 *m/s* for air and (Table 16) 131.29 *m/s* to 480 *m/s* for helium. The helium impact velocities were slightly higher than those of air, similar to the single valve arrangement case. When comparing the single valve arrangement to the double valve arrangement, the single valve substrate impact velocities were generally higher than those of the double valve arrangement.

Impact velocities were also tested for the single valve arrangement at different valve opening frequencies. Flow impact velocities (Table 20) for air ranged from 166.7 *m/s* to 461 m/s at 10 Hz and no defined wave could be obtained at 20 Hz. Flow impact velocities (Table 21) for helium ranged from 200.36 *m/s* to 555.13 *m/s* at 10 Hz and reached up to 549 *m/s* at 20 Hz. The flow impact velocity slightly decreases with an increase in valve opening frequency for air. The flow impact velocity for helium is almost constant for the different frequencies.

In accordance with many previous experimental and computational analyses it has been shown that the gas flow is subsonic in the stagnant region at the tube exit and that the component of the gas velocity normal to the substrate surface is quite small in comparison with the gas and particle exit velocity (Grujicic et al, 2004). This is also observed in the experimental results,

6.4 Tube Downstream Static Pressure

Tables 21 and 23 show static pressure readings downstream at transducer B and transducer C locations. Transducer B is 250mm from the solenoid valve and transducer C is 720mm from the solenoid valve. At 250mm downstream the static pressure ranges from 24% to 34

% of the reservoir pressure, with the pressure being at 3.37 bar for a 10 reservoir pressure and at 14.23 bars for a 50 bar reservoir pressure in the single valve arrangement. At 720mm downstream which is closer to the gun exit the static pressure ranges from 13 % to 18 % of the reservoir pressure, with the pressure being at 1.7 bar for a 10 bars reservoir pressure and 8.66 bars for a 50 bar pressure reservoir. The static pressure in the tube reduces as the compression waves travel downstream of the solenoid valve. The static pressure in the tube becomes important when powder has to be introduced into the tube. To prevent the powder from being pushed back into the feeder or being over fed into the shock tube the static pressure in the tube has to be known.

6.5 Flow Pressure Pulses

Section 5.2.5 shows plots for the change in flow static pressure in time for the 5, 10 and 20 Hz frequencies. Figures 49 and 50 shows the change in pressure in time at 30 bar for air and helium gas at 5 Hz valve opening frequency. At 5 Hz figure 60 shows the helium gas to be travelling through the pressure transducer at a much faster rate than air.

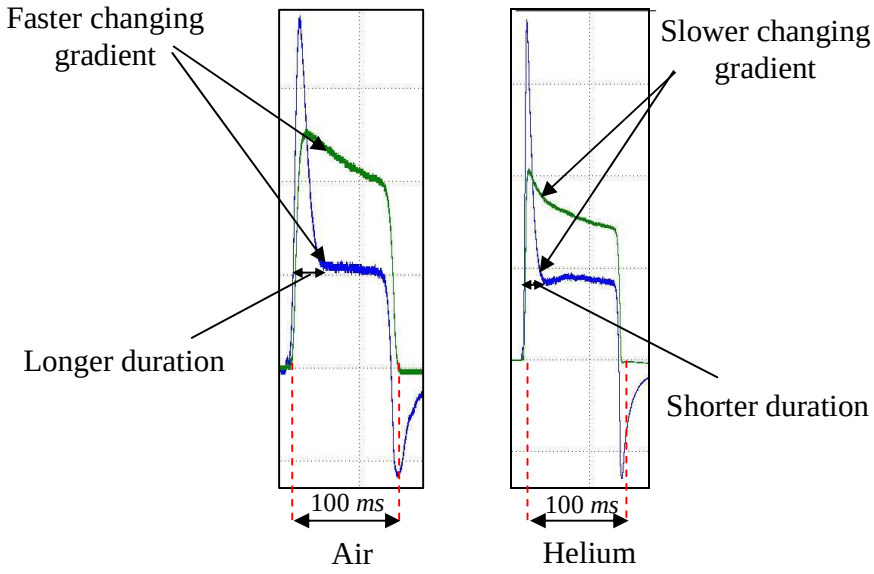

Figure 60: Air and helium static pressure pulses at 5Hz

The solenoid valves take 100 *ms* to fully open, and it is evident in the figure that the compression wave passes in less than half the valve opening time, this means that the shock

wave passes through the pressure transducers downstream of the valve before the valve is fully opened.

Figures 51 and 52 show the change in pressure in time with a valve opening frequency of 10 Hz. It can also be seen that helium travels through the transducer faster than air. The pressure of the pulses decreases with time, which means that gas is being taken out of the reservoir faster that it can be supplied. Therefore, for faster frequencies of operation an even larger reservoir will be required. Figures 53 and 54 show the change in pressure in time with a valve opening frequency of 20 Hz. A valve opening frequency of 20 Hz is too fast for air since an almost continuous line of air flow is shown. It is also observed that the static pressure recorded by the transducer reduces even further with time when the valve opening frequency is increased.

6.6 Gas Pre-heat Temperature

Figure 58 shows the change in gas flow velocity in time for different pre-heat temperatures in the single valve arrangement. The following reservoir temperatures were tested: room temperature (298 K), a pre-heat of 473 K and a pre-heat of 673 K. In the single valve arrangement case pre-heating the gas shows a reasonably increase in the gas flow velocity. The gas velocity was increased by (Table 23) 16.46% at 10 bar and 22.4% at 50 bar for helium when a pre-heating temperature of 673K was introduced. In air jets, the gas flow velocity was increased by (Table 23) 25.8% at 10 bar reservoir and 30% at 50 bar reservoir when a pre-heating temperature of 673K was introduced. The gas velocity due to pre-heating increases more for higher reservoir pressures compared to lower pressures for both air and helium.

In general air as the gas driver benefits more from gas pre-heating than helium. Air achieved a 30% velocity increase compare to the 25.8% of helium when preheated to the same temperature of 673 K at a reservoir pressure of 50 bars. For the air jets at 30 bars, increasing the temperature from room temperature to 200 ^0C increases the velocity (Table 23) from 441 m/s to 511.5 m/s (16% increase) and a further increase in temperature 400 ^0C results in an air jet with a velocity of 567.9 m/s (11% increase). This shows that the

increase in gas velocities due to the increase in temperature to reduce slightly as the temperature is increased even further, and this is the case with both air and helium gas drivers.

Figure 59 shows the change in gas flow velocity in time for different pre-heat temperatures in the double valve arrangement. With helium as the gas driver velocity increases due to pre-heating do not follow a consistent trend. There is no significant change when the reservoir temperature increases to $200\,^0C$, however significant change is observed when the temperature is further increased to $400\,^0C$. There is also a slight increase in velocity due to pre-heating for air jets; however, it also does not follow a consistent trend. There are complex wave patterns (multiple reflections) in the rig when two valves are used. This complexity could be attributing to the inconsistent gas velocity change due to pre-heating.

6.7 Process Physics

In the Kasimir simulations the variables of state are calculated on the basis of statistical mechanics with the assumptions that the flow in the shock tube is one-dimensional and that losses caused by the rupture of the diaphragm as well as the influence of the boundary layer are neglected. However, when a diaphragm is used in a shock tube, the one dimensional character of the shock tube flow tends to be destroyed. Under the initial differential pressure the diaphragm tends to bow. As soon as it shatters the gas flow has a component towards the wall of the shock tube, rather than being directed purely along the axis. This effect results in transverse waves being produced inside the shock tube.

The solenoid valves used are not full bore flow valves, but have small cavities through which flow has to travel. This curved paths result in a generation of transverse waves in the tube. The flow also incurs losses due to the curved paths. There is usually a time delay in the valve opening process, before the valve can fully open. This means that the compression wave exits the valve before it is fully opened as shown in section 6.5. The compression waves will therefore have travelled several meters down the tube before a well defined shock is formed. The properties of the solenoid valve make its flow deviate from the ideal conditions characterized by the Kasimir simulation. However, the

simulations still give a good approximation of what the flow velocity in the experimental tube will be.

Due to the relatively small slope of the pressure rise in the pressure pulses plots, the flow is modelled as strong compression waves instead of shock waves. The flow is assumed to be isentropic for modelling simplifications. For the purpose of isentropic flow the stagnation pressure is a useful reference but the conditions under which the different stagnation properties remain constant must always be considered (Skews, 2008). While the static properties are a measure of the thermodynamic state of the system, the stagnation properties are a measure of the kinetic energy as well. The difference between the two being entirely due to the kinetic energy of the fluid.

The Mach number at the leading edge of the compression wave propagates at local sound speed and is unity and the Mach number of the flow will vary through the compression. In the experiment the static pressure at two points downstream of the solenoid valve is known and the compression wave velocity between the two points is also known. The kinetic energy of the flow is approximated using the compression wave velocity. The dynamic pressure and the static pressure which give the total pressure of the flow are used to approximate the Mach number of the flow.

6.8 Particle Trajectory

Dykhuizen and Smith analysed the interactions of the carrier gas with the spray particle under the approximation of a dilute two-phase (gas + non-interacting solid particles) flow equation 10 shows how the particles relate to the gas flow.

$$\frac{d_v}{d_t} = \frac{\rho(v - v_p)^2 A_P C_D}{2m_p}$$

An analysis of the above equation shows that the ultimate particle velocity is equal to the gas velocity. The gas velocity within the tube depends on the total gas temperature and the tube geometry, but not on the gas pressure (under the condition of constant drag coefficient). However, the particle's initial acceleration is linearly dependent on the stagnation pressure but independent of the total temperature. Thus, while the stagnation

pressure does not affect the maximum particle velocity, it has to be sufficiently high to ensure that the spray-particles velocity will approach the gas velocity over a relatively short length (Grujicic et al, 2004).

In the experiment the reservoir temperature was kept at room temperature for all the tests. The gas acceleration was solely dependent on the stagnation pressure. Reasonably high gas velocities were obtained in the experiment for both air and helium jets. With preheating of the reservoir gas; gas velocities will be even higher are shown by figure 58.

6.9 Rig Performance

Significantly high jet velocities were obtained at room temperatures using the designed rig, with air as the gas driver jet velocities (Table 5) of up to 516.34 *m/s* were achieved and with helium as the gas drive jet velocities (Table 6) of up to 876.92 m/s were achieved within the tested range of 10 to 50 bars reservoir pressure. These high velocities can be achieved at a wave generation frequency of 5 Hz. The rig can generate high velocity jets even at higher frequencies of up to 20 Hz.

From the literature it is observed that most materials get deposited (have a critical velocity) at velocities ranging from 500 to 700 m/s. Using the designed rig with helium as the gas driver, some of the powder particles can be accelerated to the required critical velocity range. With air as the gas driver pre-heating can be used to significantly increase the jet velocities to values sufficient for particle deposition.

Chapter 7 Conclusions and Recommendations

7.1 Conclusions

- The air jet velocity is significantly lowered with increased valve opening and closing frequency for the tested range.
- Helium jets velocities behave similarly to each other for different valve opening and closing frequencies within the tested range, there are no drops in velocity as the frequency is increased.
- Strong compression waves (supersonic compression waves) are formed in the tube, the tube is not long enough for the compression waves to coalesce into a shock wave.
- The difference in impact velocities of air and helium is much smaller in comparison with jet flow velocity difference inside the tube.
- The flow impact velocity decreases slightly with an increase in valve opening frequency for air. The flow impact velocity for helium is almost constant for the different frequencies.
- The static pressure in the tube reduces as the compression waves travel downstream of the solenoid valve.
- The compression wave exits the solenoid valve before the valve is fully opened.
- Faster valve opening frequencies require even larger reservoirs to accommodate the higher air demand.
- Gas pre-heating has a larger effect of increasing gas velocities at higher pressure for the single valve arrangement.
- The effectiveness of increasing gas velocity with the increase in temperature reduces as the temperature is increased even further for the single valve arrangement.
- The single valve arrangement generally performs better than the double valve arrangement.

7.2 Recommendations

- A heating unit should be incorporated into the rig in order to allow for testing of pre-heated reservoir conditions.
- The reservoir should be made even bigger in order to maintain a constant pressure at high frequencies (20Hz) test.
- A double acting solenoid valve should be used for the second valve in the double valve arrangement. This is to prevent a spring having to act against shock loading. If a solenoid is made to act against the shock load, chances of unplanned opening of the valve will be significantly reduced.
- Different gas drivers should be tested, e.g. a combination of helium and air or pure nitrogen.
- Helium gas is very expensive; a mechanism to recycle the driver gas should be investigated.

Reference List

1) A. Papyrin, *Cold spray technology*, Elsevier, 2007, pages 25-36.

2) A.P. Alkhimov, V.F. Kosarev, and A.N. Papyrin, *Dokl. Akad. Nauk SSSR*, Vol. 315, 1990, pp. 1062–1065.

3)A.P Alkhimov, A.N Papyrin, V.F Kosarev, US Patent 5 302 413, (1994)

4) B. Jodoin, P. Richer, G. Berube, L. Ajdelsztjn, A. Erdi-Betchi, M. Yandouzi, *Pulsed-gas dynamic spraying: process analysis, development and select coating examples*, volume 201, 2007, pages 7544-7551.

5) T. Schmidt, F. Gartner, H. Assadi, and H. Kreye, *Development of a Generalized Parameter Window for Cold Spray Deposition*, Acta Mater. , 2006, 54, p 7544-7551.

6) X. Luo and H. Oliver, *Gas Dynamic Principles and Experimental Investigations of Shock Tunnel Produced Coatings*, ASM International, 2009, p 1059-9630.

7) J. Villfuerte, D. Vanderzwet, M. Yandouzi and B. Jodoin, *Shock Wave Induced Spraying*, Advanced Materials and Processes, March 2009.

8) B.W. Skews, *Course Notes-MECN 4001 and MECN 4004-Compressible Flow*, University of the Witwatersrand, 2008, pages 19 and 31-40.

9) J K Wright, *Shock Tubes*, London: Methuen & CO LTD, 1961,

10) J. D. Anderson, *Modern Compressible Flow*, Mcgraw-hill, 1982.

11) P. Oostehuizen, W. E. Carscallen, *Compressible fluid flow*, New York: McGraw-Hill, 1997.

12) C. Tropea, A. Yarin and J. Foss, *Springer Handbook of Experimental Fluid Mechanics*, Springer, 2007, pp 1095-1096

13) KASIMIR: Shock wave laboratory, Rwth Aachen University, Germany, accessed 9 July 2009.
http://www.swl.rwth-aachen.de/en/industry-solutions/thin-films/

14) ASCO –Joucomati, Function, terminology and construction types. Accessed: 9 October 2009.
http://www.ascojoucomatic.nl/images/site/upload/_en/pdf1/01027gb.pdf

15) V.V Sobolev, J.M. Guilemany, J.A. Calero, *Prediction of Powder Particle Behaviour During High-velocity Oxyfuel Spraying, ASM International, thermal spraying technology, 1995, vol 4(3). p 287-296*

16) K.S Han, M.K Chung, and H.J. Sung, *Application of Lumley's Drag Reduction Model to Two-phase Gas-Particle Flow in Pipe,* Trans. ASME, J. Fluids Eng. , Vol 113, 1991, p130-136

17) M. Grujicic, C.L Zhao, C. Tong, W.S DeRosset, D. Helfritch, Analysis of the impact velocity of powder particles in the cold-gas dynamic-spraying process, Material Science and Engineering, Vol A368, 2004, 222-230.

18) C.P. Donaldson, R.S. Snedeker, J. Fluid Mech. 45 (1971) 281.

19) S. A. Morsi, A.J. Alexandra, An Investigation of Particle trajectories in Two Phase Flow Systems, J. Fluid Mech. 55 (2) (1972) 193-208.

20) ASME B1.13, Process piping: ASME code for pressure piping, ASME International, 2007, Page 18

APPENDIX A

Engineering Drawings

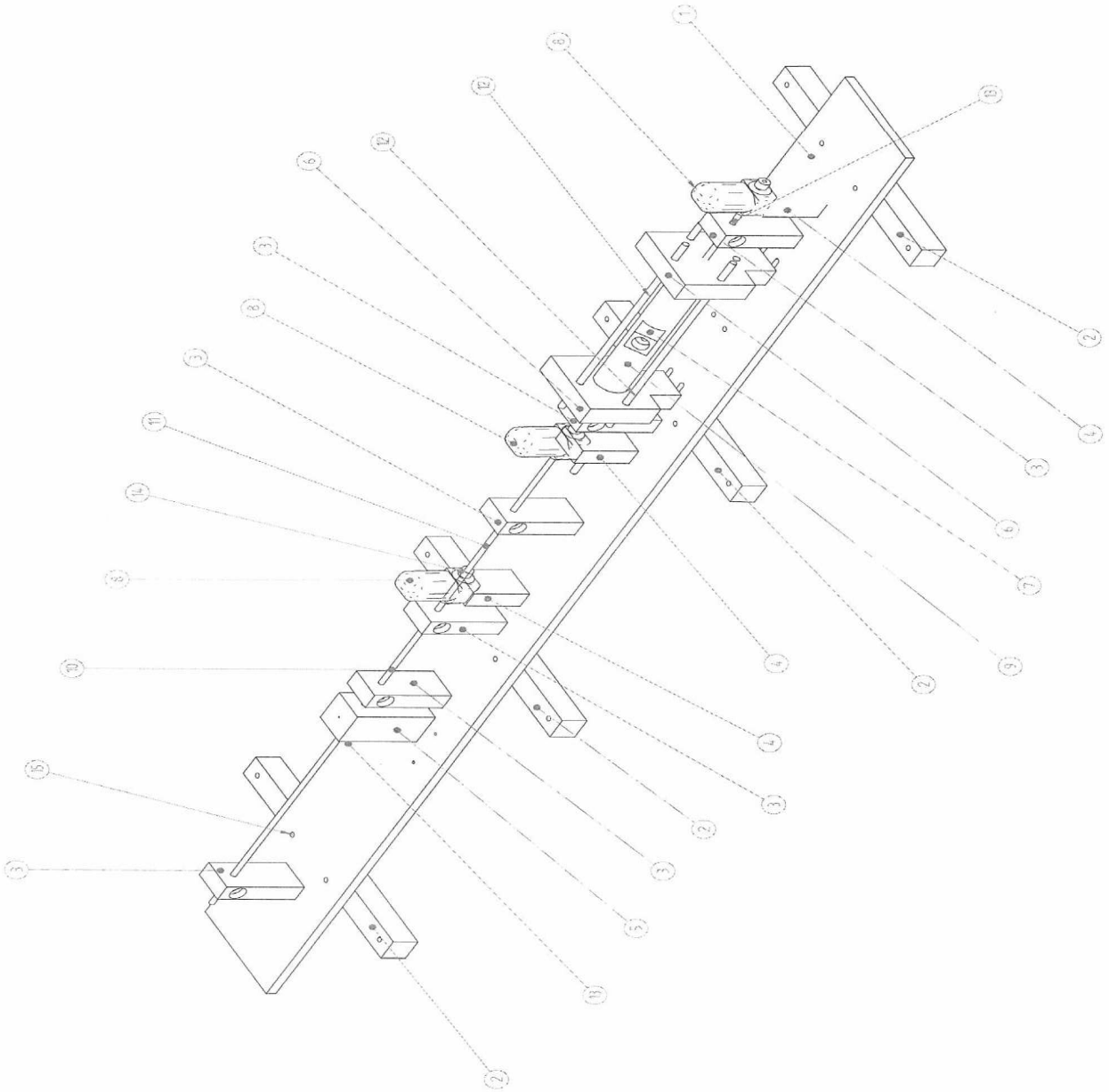

Rig Assembly

Item Number: 1
Name: Assembly Base
Material: Mild Steel
Quantity: 1

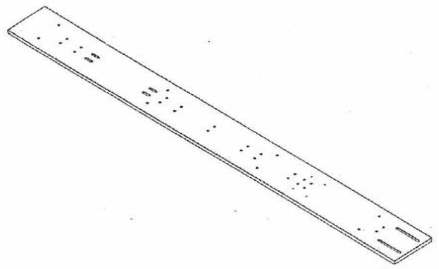



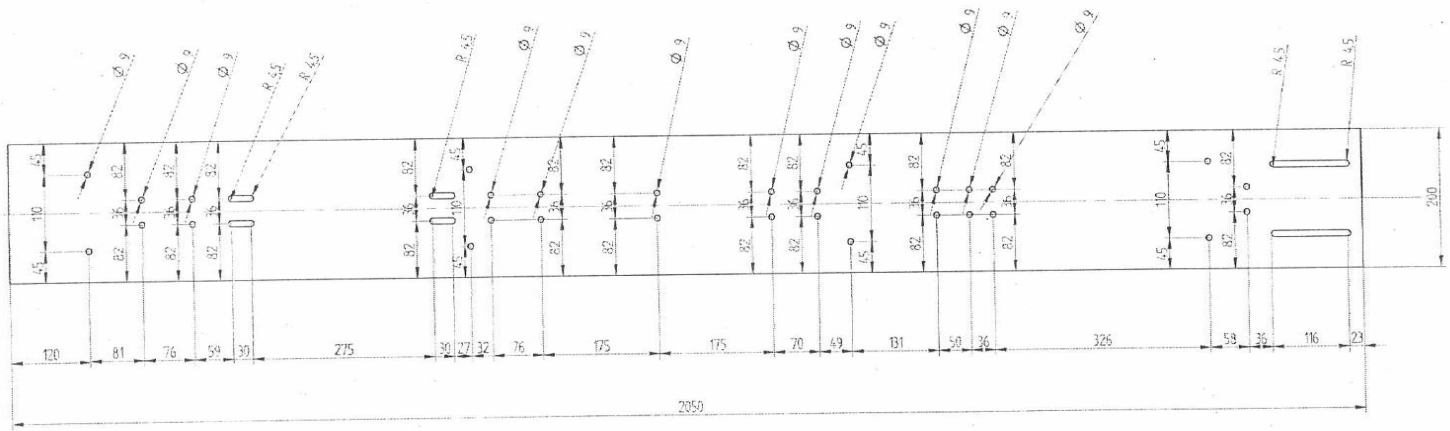

Item Number:2
Name: Base Stand
Material: Mild Steel
Quantity: 4

REVISION HISTORY			
REV	DESCRIPTION	DATE	APPROVED

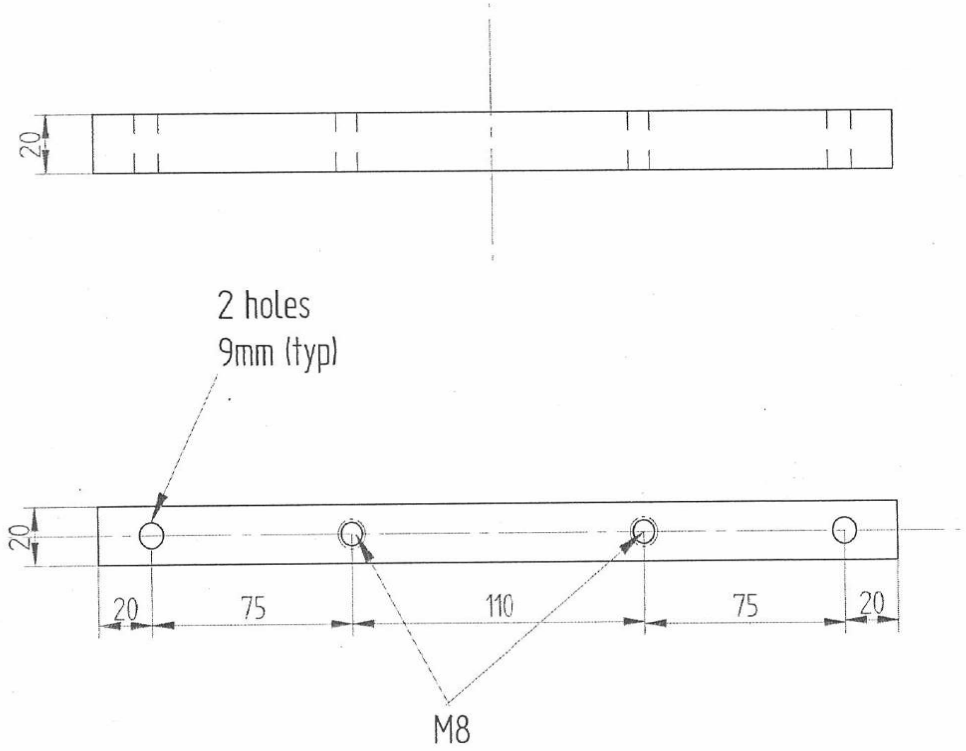

Note: Drill through together with assembly plate

	NAME	DATE
DRAWN	USERNAME	05/27/09
CHECKED		
ENG APPR.		
MGR APPR.		

UNLESS OTHERWISE SPECIFIED
DIMENSIONS ARE IN MILLIMETERS
ANGLES ±X.X°
2 PL ±XXX 3 PL ±XXXX

SOLID EDGE
UGS - The PLM Company

TITLE

SIZE A2 | DWG NO | REV

FILE NAME Base Stand.par

SCALE | WEIGHT | SHEET 1 OF 1

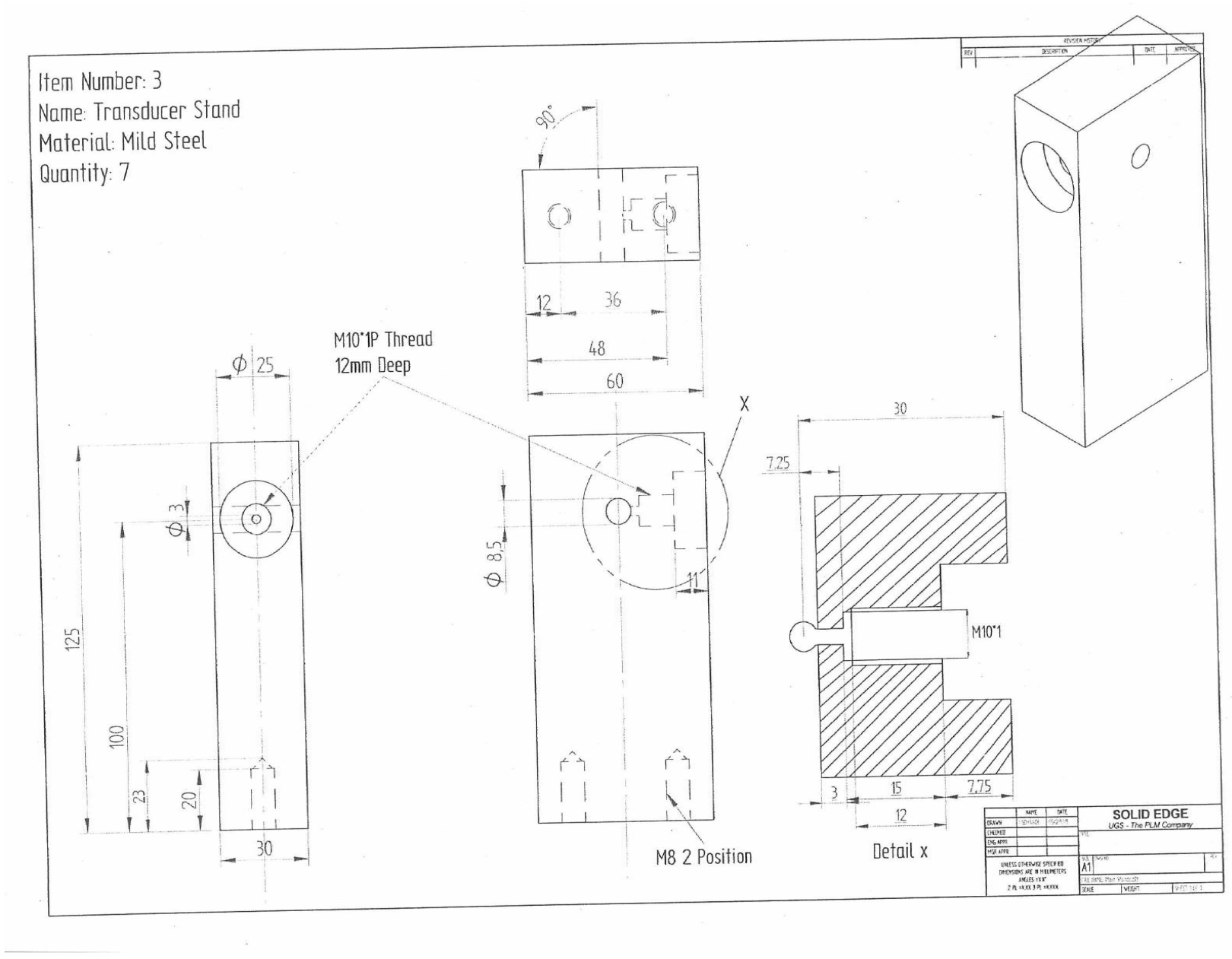
Item Number: 3
Name: Transducer Stand
Material: Mild Steel
Quantity: 7
90°
12
36
48
60
M10*1P Thread
12mm Deep
ϕ 25
ϕ 3
ϕ 8.5
X
125
100
23
20
30
11
30
7.25
M10*1
3
15
7.75
12
M8 2 Position
Detail x
SOLID EDGE
UGS - The PLM Company
A1

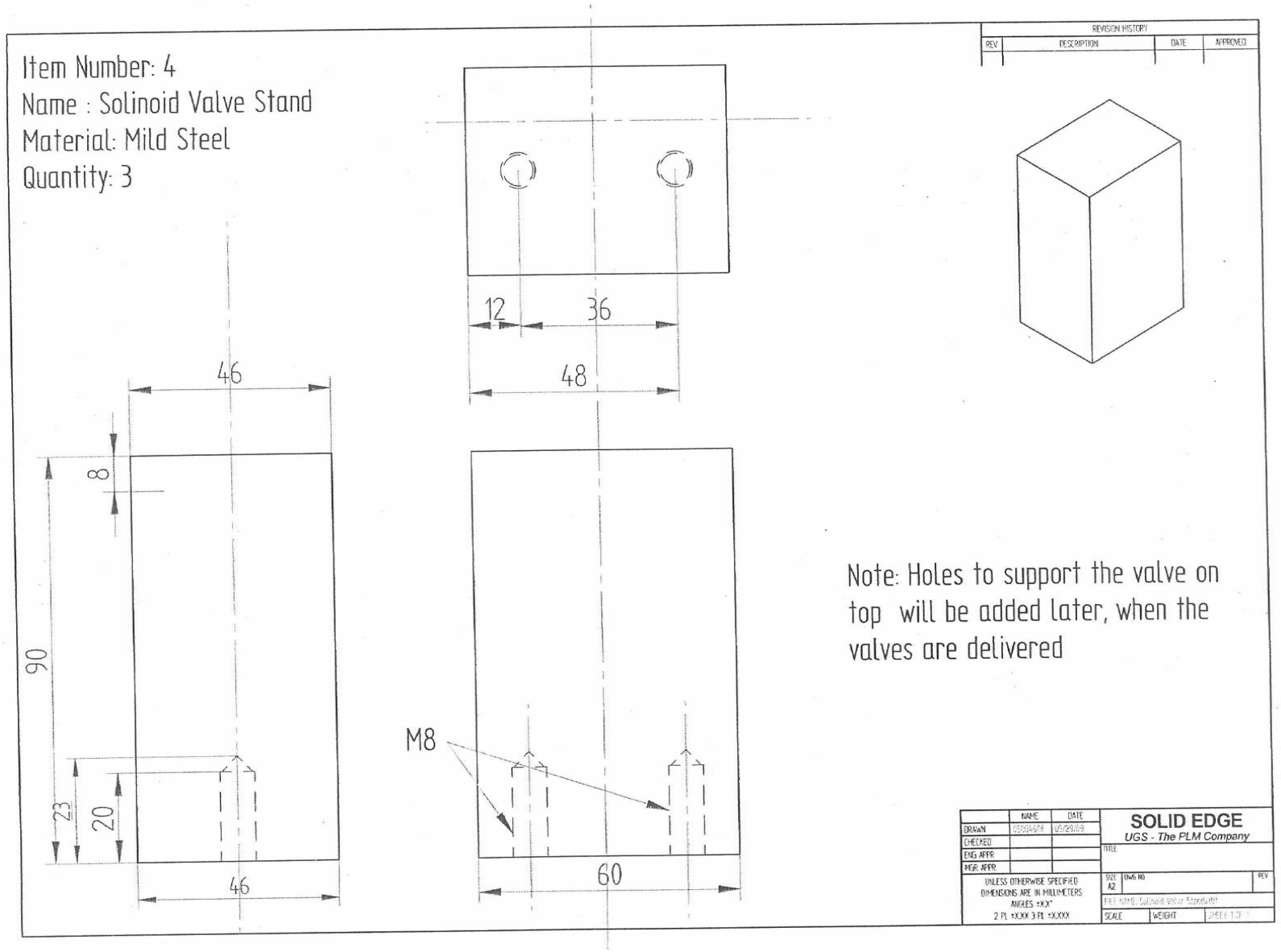
Item Number: 4
Name : Solinoid Valve Stand
Material: Mild Steel
Quantity: 3
REVISION HISTORY
REV
DESCRIPTION
DATE
APPROVED
12
36
48
46
8
90
23
20
46
M8
60
Note: Holes to support the valve on top will be added later, when the valves are delivered
NAME
DATE
DRAWN
CHECKED
ENG APPR.
MGR APPR.
UNLESS OTHERWISE SPECIFIED
DIMENSIONS ARE IN MILLIMETERS
ANGLES ±X°
2 PL ±XXX 3 PL ±XXXX
SOLID EDGE
UGS - The PLM Company
TITLE
SIZE
A2
DWG NO
REV
SCALE
WEIGHT
SHEET 1 OF 1

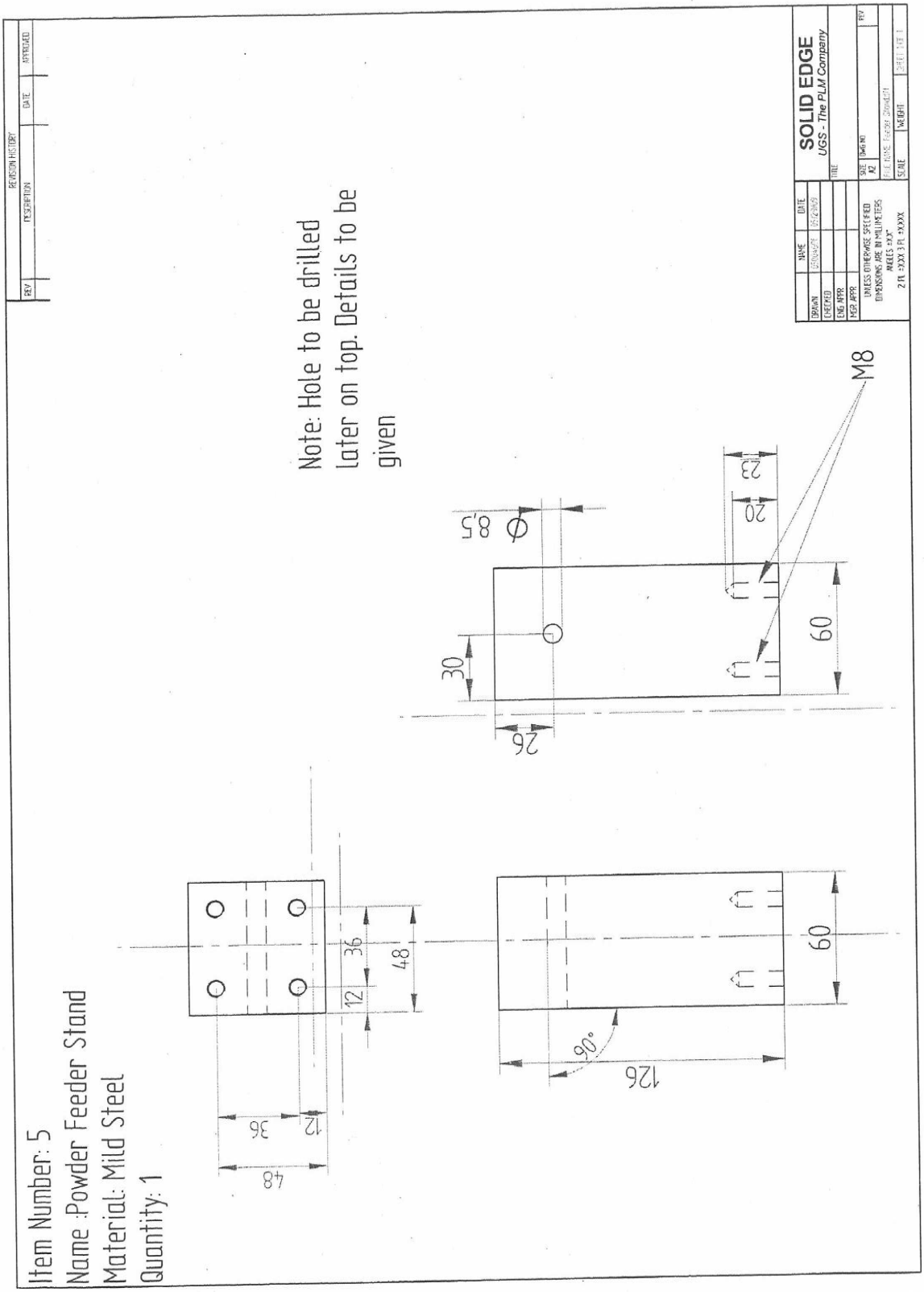
Item Number: 5
Name :Powder Feeder Stand
Material: Mild Steel
Quantity: 1
Note: Hole to be drilled later on top. Details to be given
M8
Ø 8,5
23
20
30
26
60
60
126
90°
36
48
12
36
12
48
REVISION HISTORY
REV
DESCRIPTION
DATE
APPROVED
SOLID EDGE
UGS - The PLM Company
UNLESS OTHERWISE SPECIFIED DIMENSIONS ARE IN MILLIMETERS
ANGLES ±XX°
2 PL ±XXX 3 PL ±XXXX
DRAWN
CHECKED
ENG APPR.
MGR APPR.
NAME
DATE
TITLE
SIZE
A2
DWG NO
REV
SCALE
WEIGHT
SHEET 1 OF 1

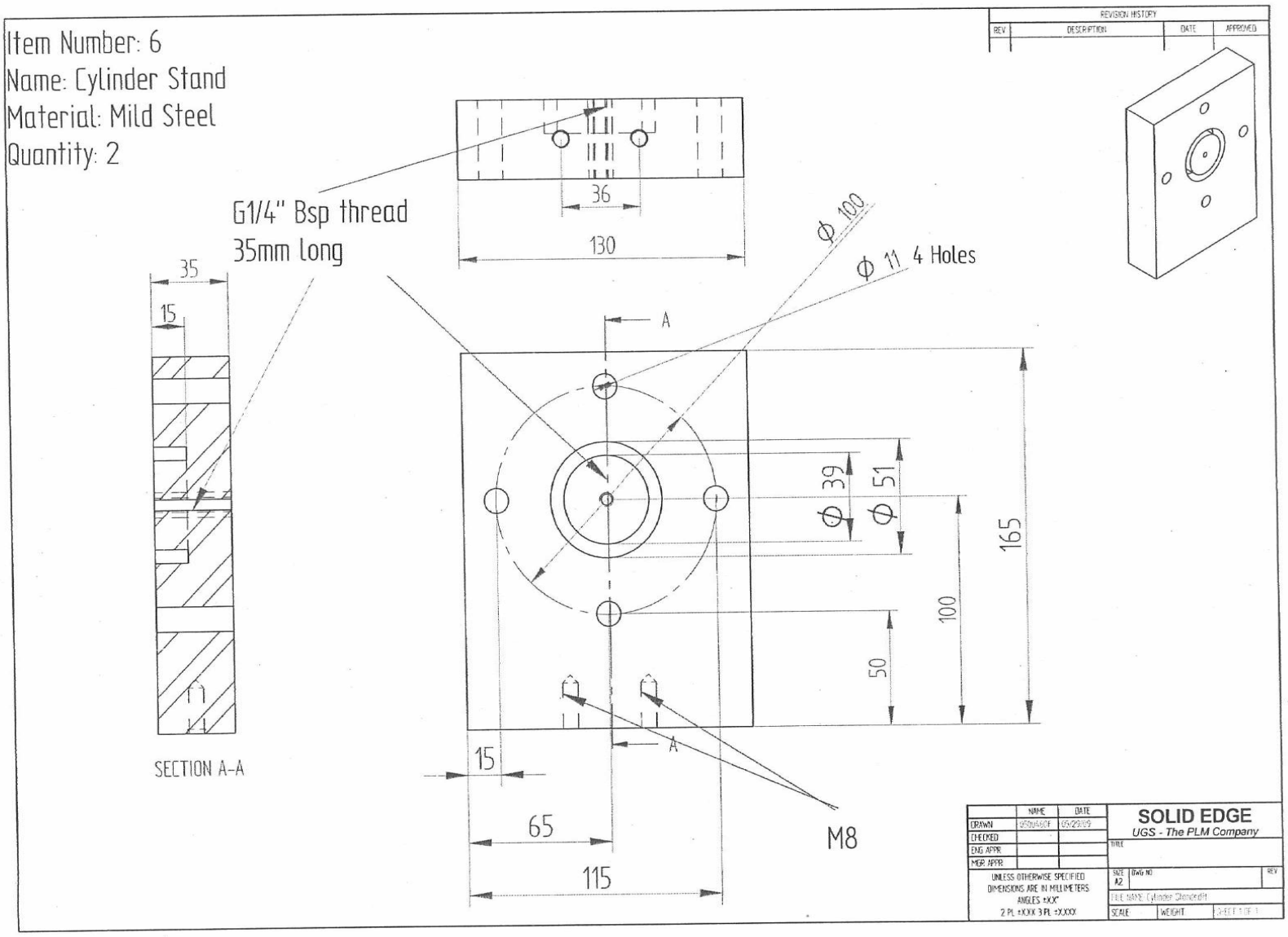
Item Number: 6
Name: Cylinder Stand
Material: Mild Steel
Quantity: 2
G1/4" Bsp thread
35mm long
Φ 100
Φ 11 4 Holes
36
130
35
15
SECTION A-A
A
Φ 39
Φ 51
165
100
50
15
65
115
M8
REVISION HISTORY
REV
DESCRIPTION
DATE
APPROVED
SOLID EDGE
UGS - The PLM Company
DRAWN
CHECKED
ENG APPR.
MGR APPR.
UNLESS OTHERWISE SPECIFIED
DIMENSIONS ARE IN MILLIMETERS
ANGLES +XX°
2 PL +XXX 3 PL +XXXX
SIZE
A2
SCALE
WEIGHT

Assembly Drawing pf
Item number 7 and 9

REVISION HISTORY			
REV	DESCRIPTION	DATE	APPROVED

Number	Component
7	Transducer Stand
9	Cylinder Tube

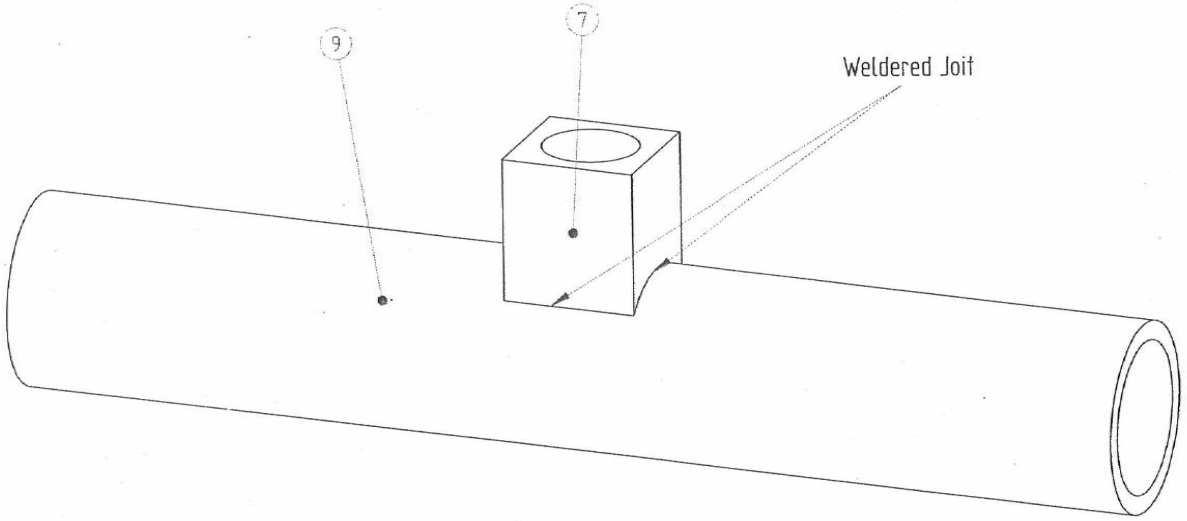

Standard Parts
Cylinder Tube (9) : Dimensions
Length: 300 mm
Internal Diameter: 40 mm
External Diameter: 50 mm
Material: Mild Steel

	NAME	DATE
DRAWN		
CHECKED		
ENG APPR.		
MFG APPR.		

UNLESS OTHERWISE SPECIFIED DIMENSIONS ARE IN MILLIMETERS
ANGLES ±0.5°
2 PL ±XXX 3 PL ±XXX

SOLID EDGE
UGS - The PLM Company

SIZE A1 | DWG NO | REV
SCALE | WEIGHT | SHEET 1 OF 1

Item Number: 7
Name: Transducer Stand
Material: Mild Steel
Quantity: 1

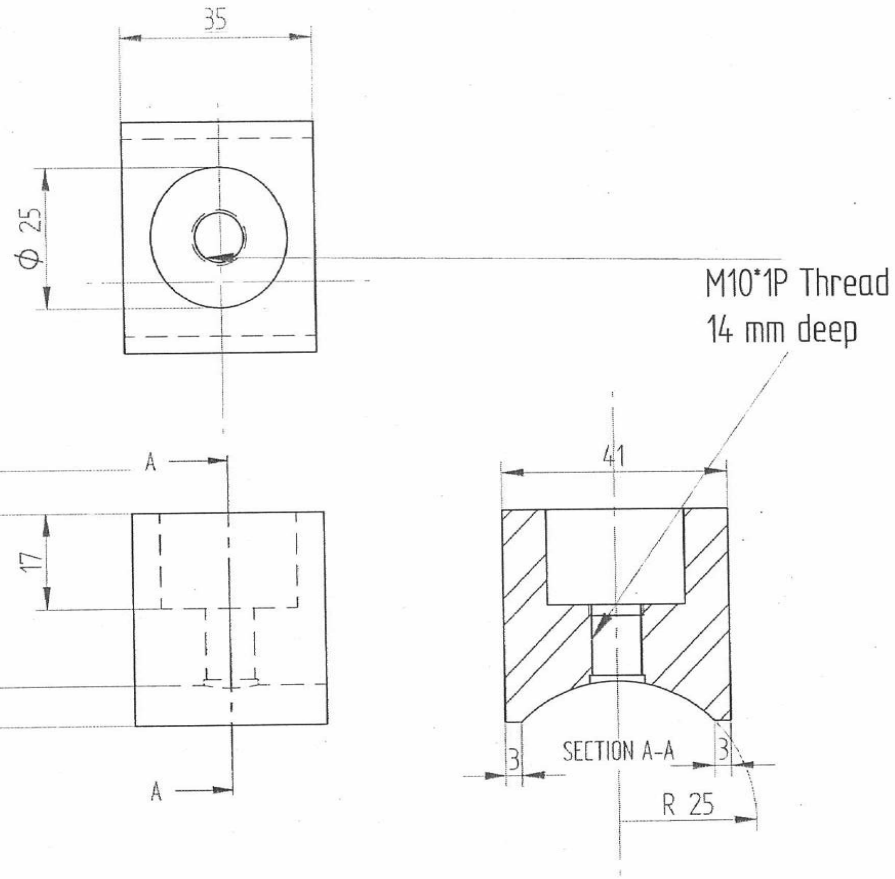

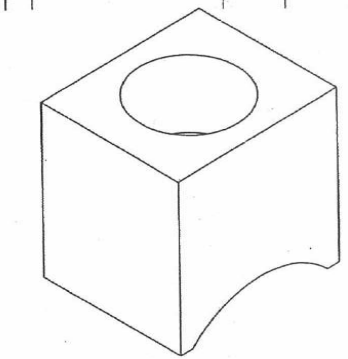

REVISION HISTORY			
REV	DESCRIPTION	DATE	APPROVED

Note: Hole to be created after welding to item number 9

	NAME	DATE
DRAWN		
CHECKED		
ENG APPR.		
MGR APPR.		

UNLESS OTHERWISE SPECIFIED
DIMENSIONS ARE IN MILLIMETERS
ANGLES ±XX°
2 PL ±XXX 3 PL ±XXXX

SOLID EDGE
UGS - The PLM Company

TITLE

SIZE A2 | DWG NO | REV

FILE NAME: Cylinder Transducer.par

SCALE | WEIGHT | SHEET 1 OF 1

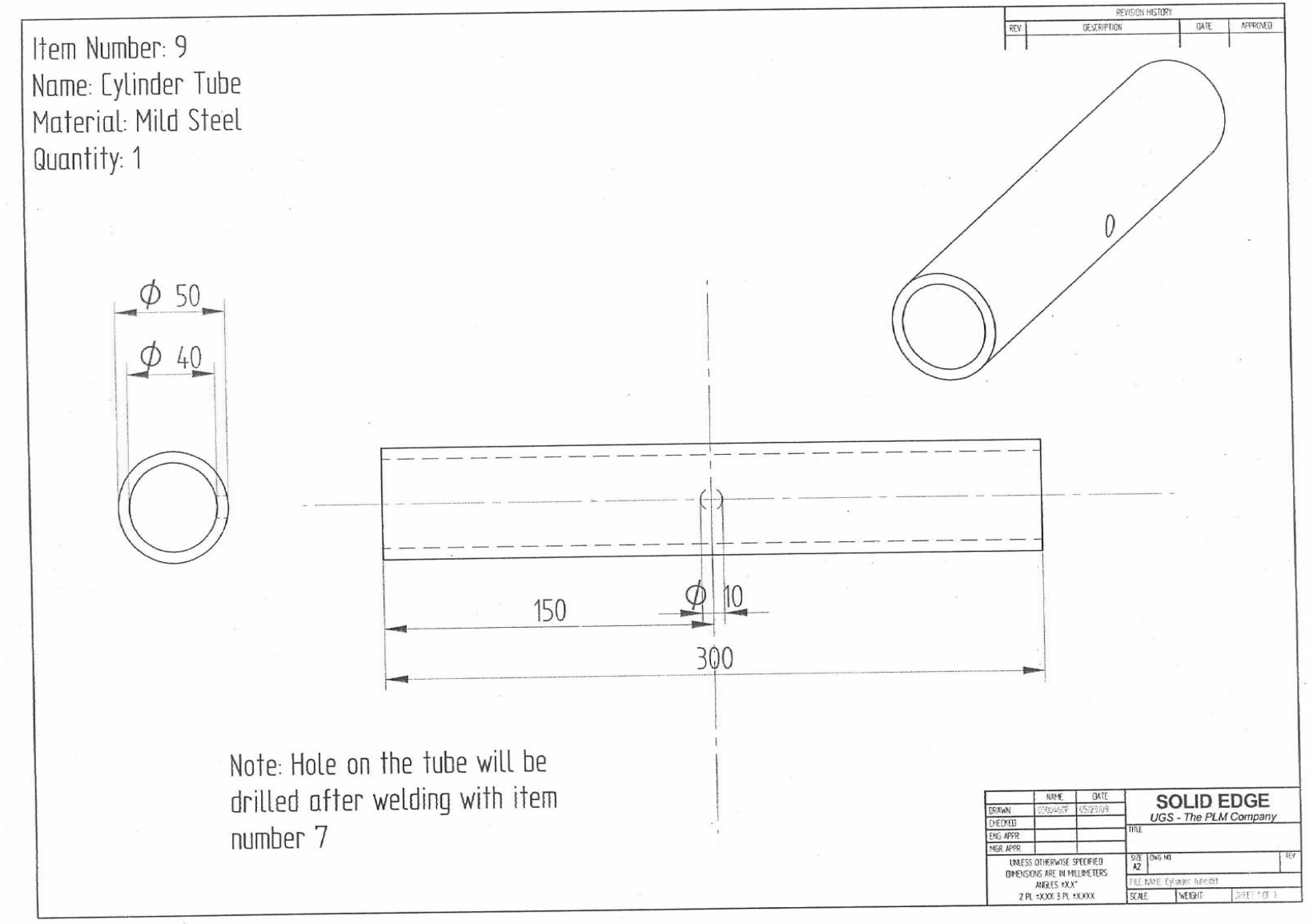
Item Number: 9
Name: Cylinder Tube
Material: Mild Steel
Quantity: 1
REVISION HISTORY
REV
DESCRIPTION
DATE
APPROVED
Ø 50
Ø 40
150
Ø 10
300
Note: Hole on the tube will be drilled after welding with item number 7
SOLID EDGE
UGS - The PLM Company
DRAWN
CHECKED
ENG APPR.
MGR APPR.
UNLESS OTHERWISE SPECIFIED
DIMENSIONS ARE IN MILLIMETERS
ANGLES ±X.X°
2 PL ±XXX 3 PL ±XXX
SIZE
A2
SCALE
WEIGHT

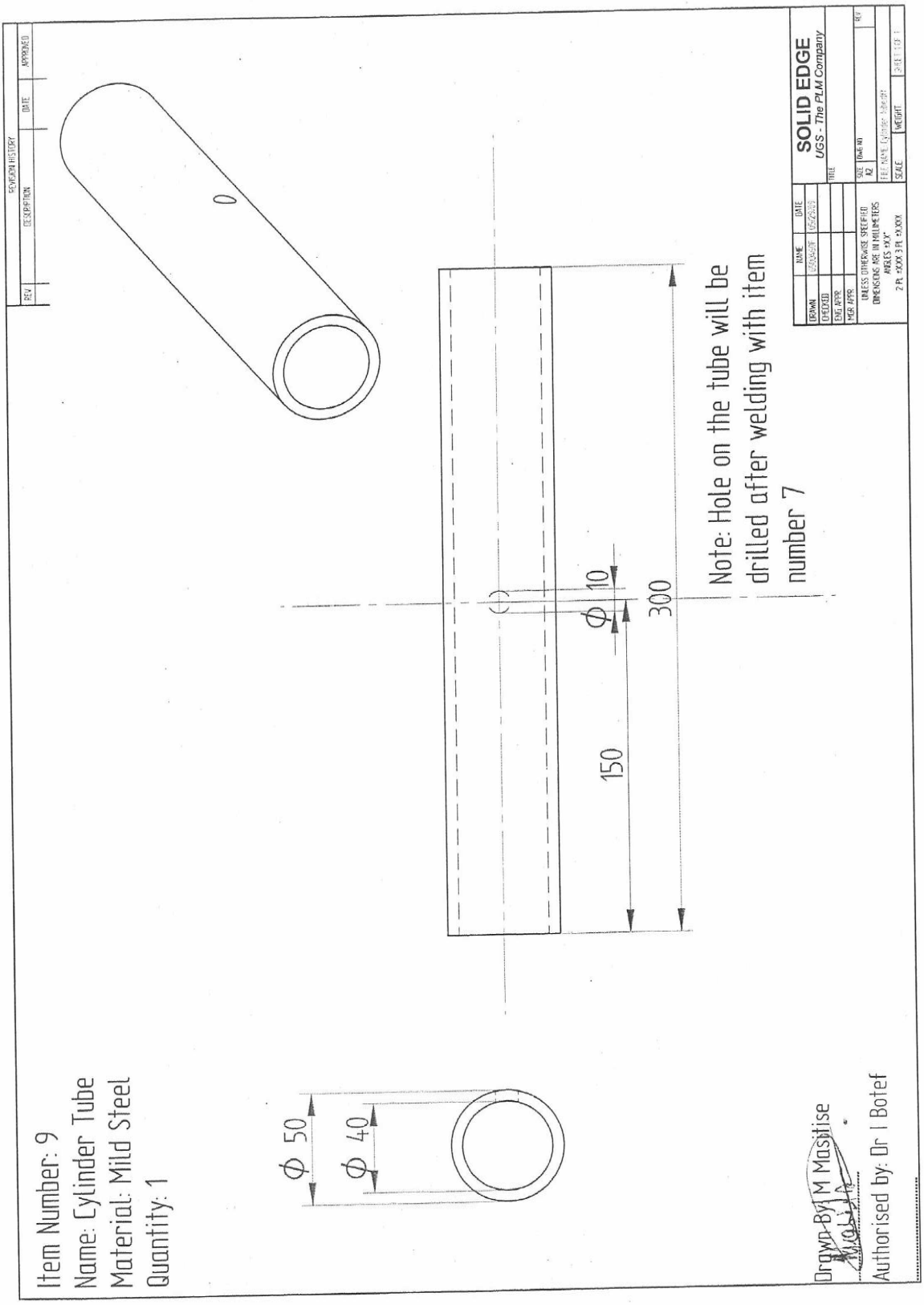
Item Number: 9
Name: Cylinder Tube
Material: Mild Steel
Quantity: 1
Ø 50
Ø 40
Ø 10
150
300
Note: Hole on the tube will be drilled after welding with item number 7
Drawn By: M Masitise
Authorised by: Dr I Botef
SOLID EDGE
UGS - The PLM Company

Item Number: 7
Name: Transducer Stand
Material: Mild Steel
Quantity: 1

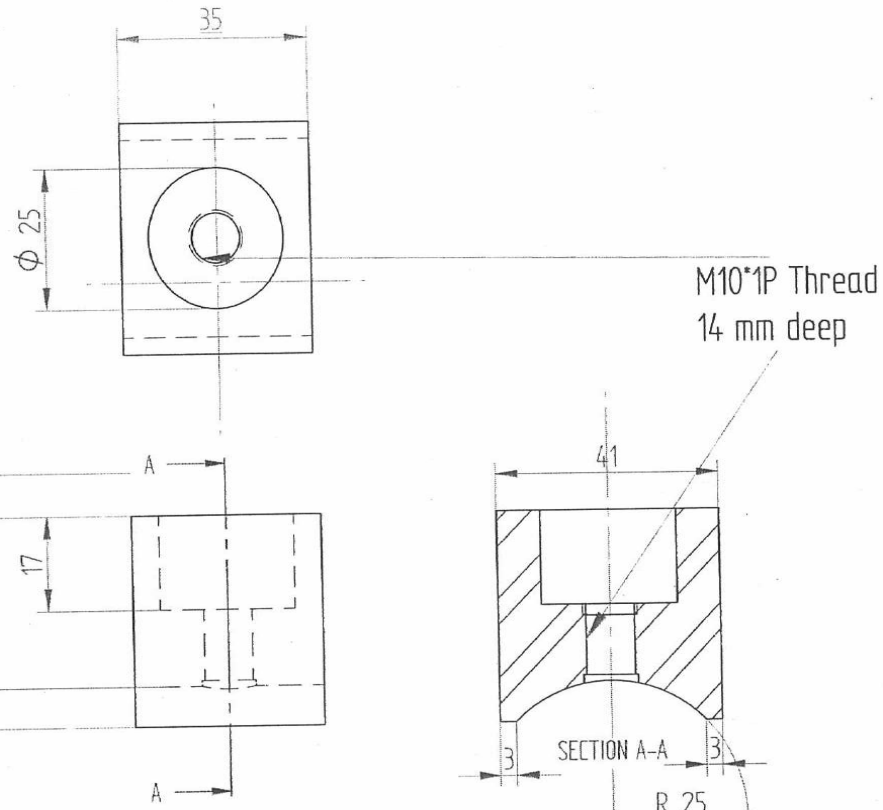

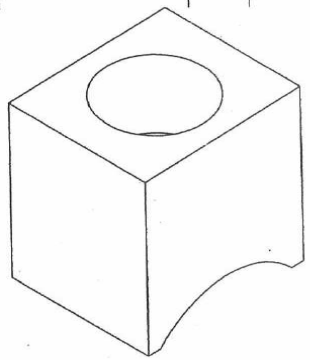

Note: Hole to be created after welding to item number 9

Drawn By: M Masitise

Authorised by: Dr I Botef

Feeder Assembly

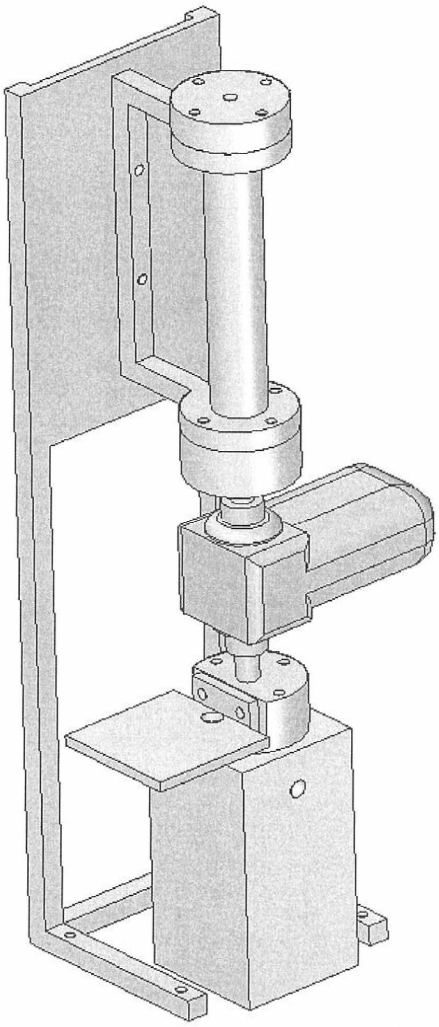

Component Name: Motor Stand
Quantity: 1
Material: Mild Steel

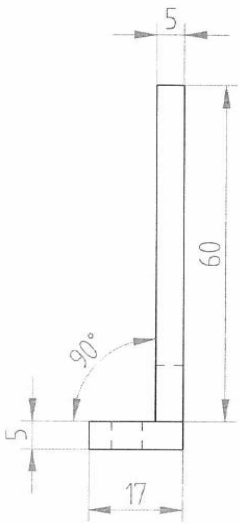

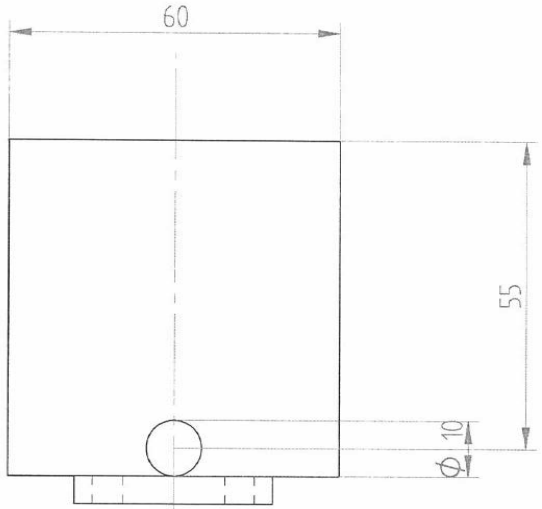

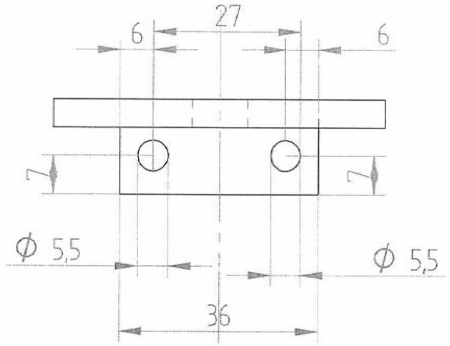

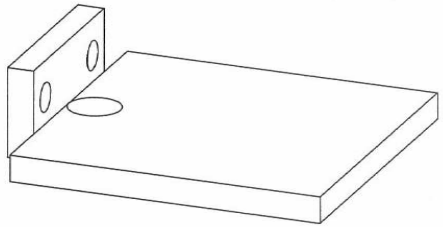

REVISION HISTORY			
REV	DESCRIPTION	DATE	APPROVED

	NAME	DATE
DRAWN		
CHECKED		
ENG APPR.		
MGR APPR.		

UNLESS OTHERWISE SPECIFIED
DIMENSIONS ARE IN MILLIMETERS
ANGLES ±X°
2 PL ±XXX 3 PL ±XXXX

SOLID EDGE
UGS - The PLM Company

TITLE

SIZE A2 | DWG NO | REV

SCALE | WEIGHT | SHEET 1 OF 1

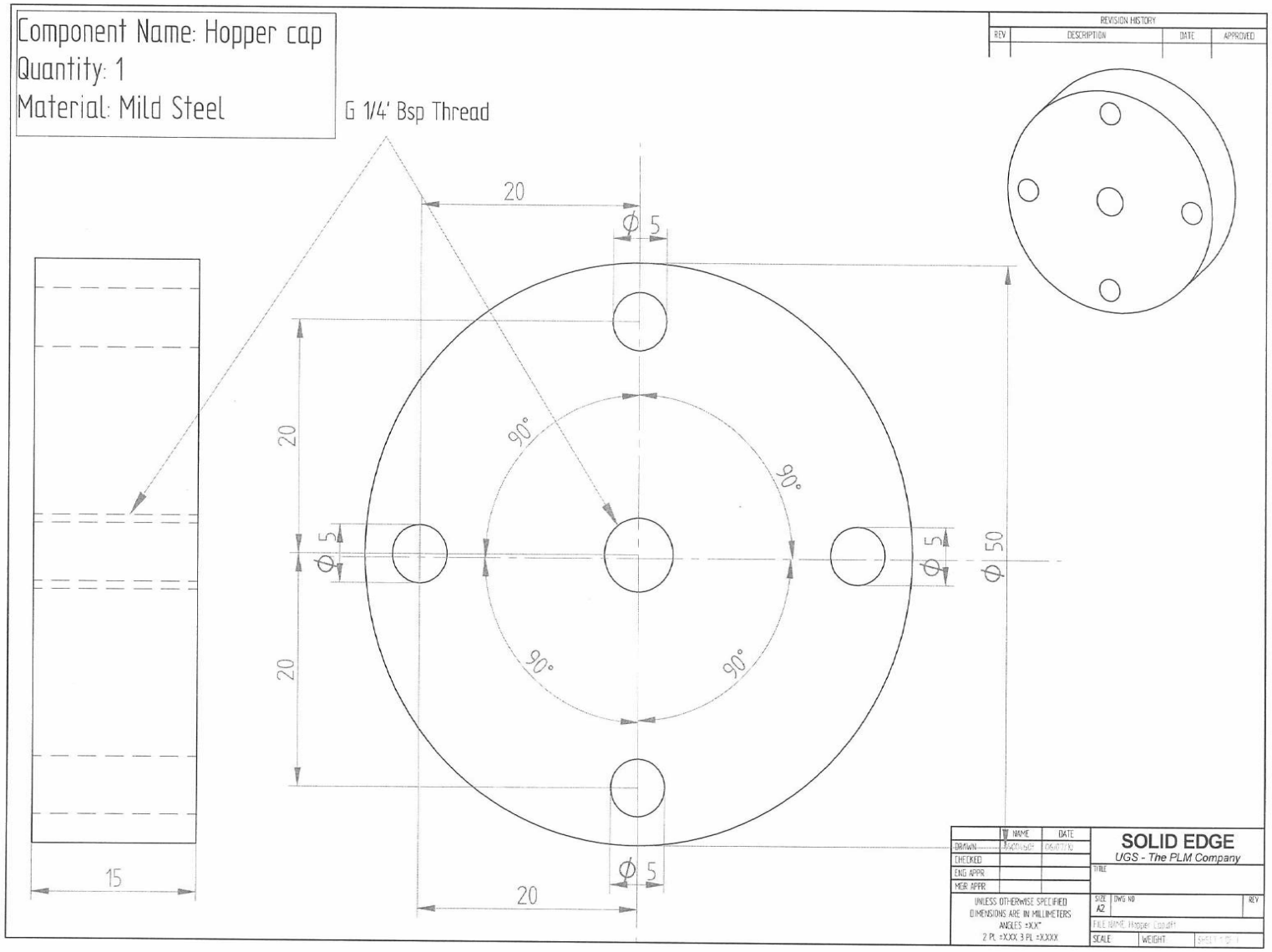
Component Name: Hopper cap
Quantity: 1
Material: Mild Steel
G 1/4' Bsp Thread
REVISION HISTORY
REV
DESCRIPTION
DATE
APPROVED
20
Ø 5
20
90°
90°
90°
90°
Ø 5
Ø 5
Ø 50
20
Ø 5
15
20
NAME
DATE
DRAWN
CHECKED
ENG APPR.
MGR APPR.
UNLESS OTHERWISE SPECIFIED
DIMENSIONS ARE IN MILLIMETERS
ANGLES ±X.X°
2 PL ±.XXX 3 PL ±.XXXX
SOLID EDGE
UGS - The PLM Company
TITLE
SIZE
A2
DWG NO
REV
SCALE
WEIGHT

Component Name: Feeder Base
Quantity: 1
Material: Mild Steel

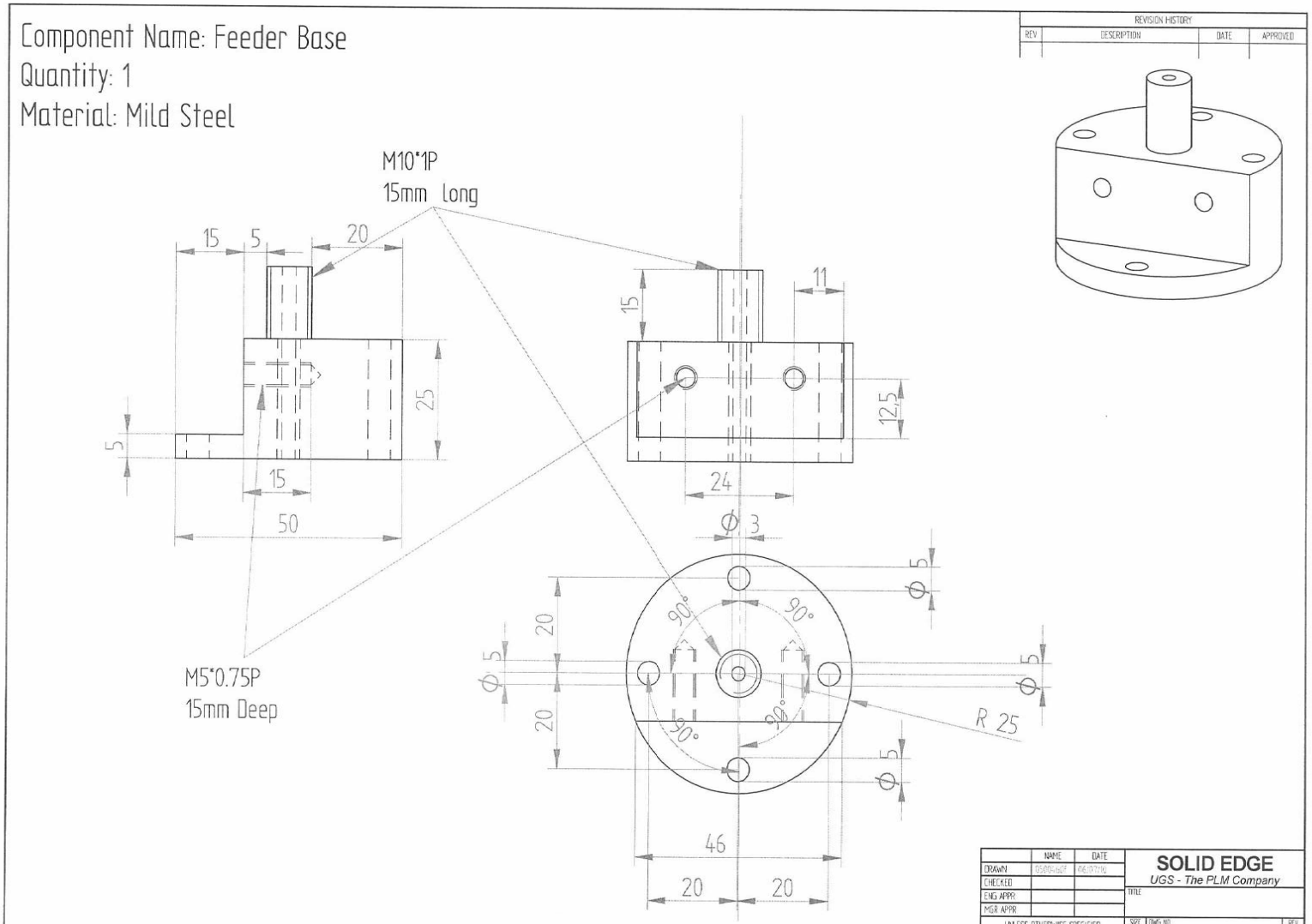

REVISION HISTORY			
REV	DESCRIPTION	DATE	APPROVED

	NAME	DATE
DRAWN		
CHECKED		
ENG APPR.		
MGR APPR.		

UNLESS OTHERWISE SPECIFIED
DIMENSIONS ARE IN MILLIMETERS
ANGLES ±X.X°
2 PL ±.XX 3 PL ±.XXX

SOLID EDGE
UGS - The PLM Company

TITLE

SIZE A2 | DWG NO | REV

F:\E NAME: Feeder Base.dft

SCALE | WEIGHT | SHEET 1 OF 1

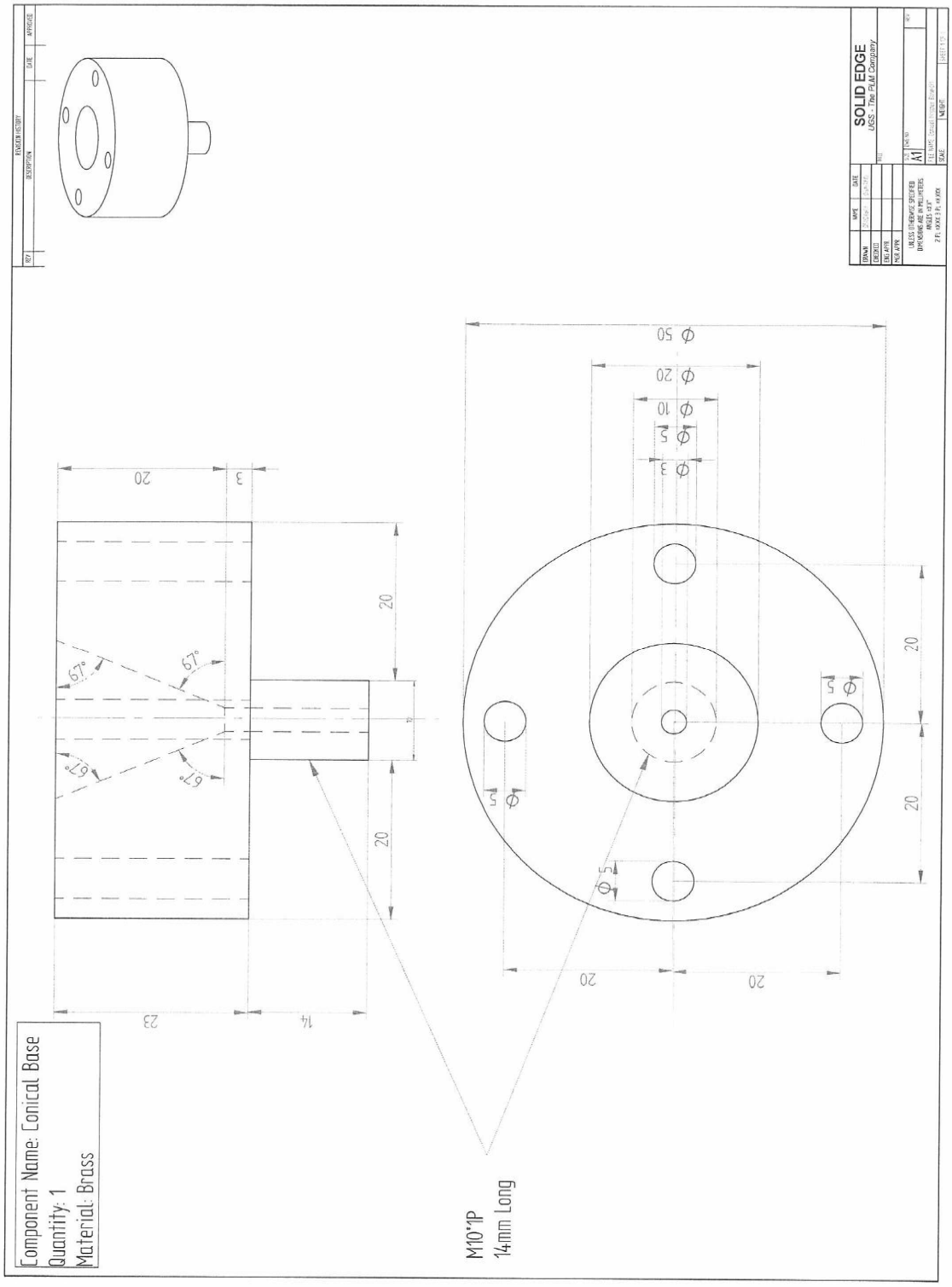
Component Name: Conical Base
Quantity: 1
Material: Brass
M10*1P
14mm Long
SOLID EDGE
UGS - The PLM Company
A1
20
3
23
14
67°
Φ 50
Φ 20
Φ 10
Φ 5
Φ 3

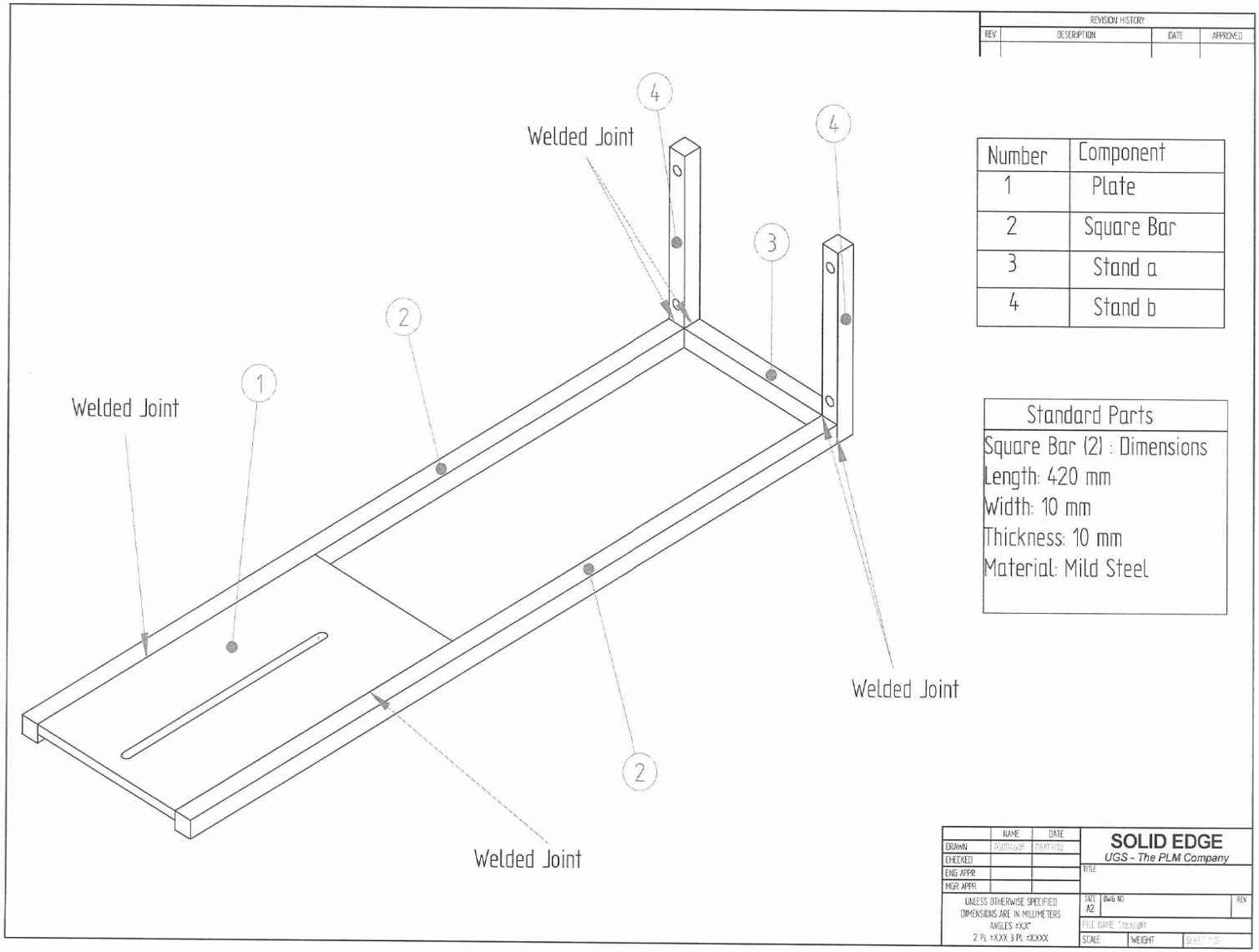
REVISION HISTORY
REV
DESCRIPTION
DATE
APPROVED
Welded Joint
Welded Joint
Welded Joint
Welded Joint
1
2
2
3
4
4
Number
Component
1
Plate
2
Square Bar
3
Stand a
4
Stand b
Standard Parts
Square Bar (2) : Dimensions
Length: 420 mm
Width: 10 mm
Thickness: 10 mm
Material: Mild Steel
NAME
DATE
DRAWN
CHECKED
ENG APPR.
MGR APPR.
UNLESS OTHERWISE SPECIFIED
DIMENSIONS ARE IN MILLIMETERS
ANGLES ±X°
2 PL ±.XXX 3 PL ±.XXXX
SOLID EDGE
UGS - The PLM Company
TITLE
SIZE
A2
DWG NO
REV
SCALE
WEIGHT
SHEET 1 OF

Component Name: Stand b
Quantity: 2
Material: Mild Steel

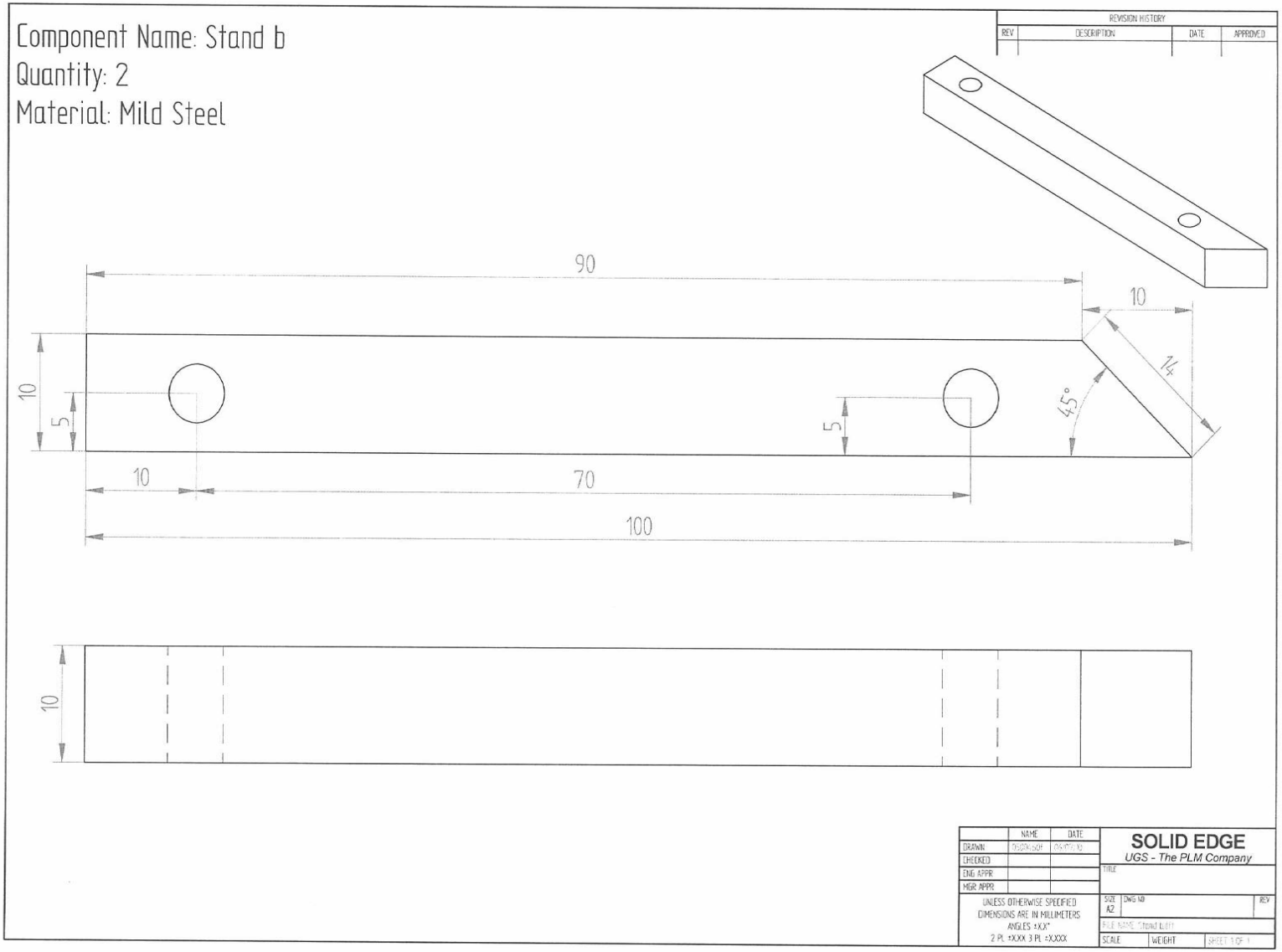

Component Name: Stand a
Quantity: 1
Material: Mild Steel

REVISION HISTORY			
REV	DESCRIPTION	DATE	APPROVED

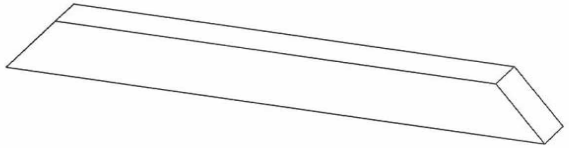

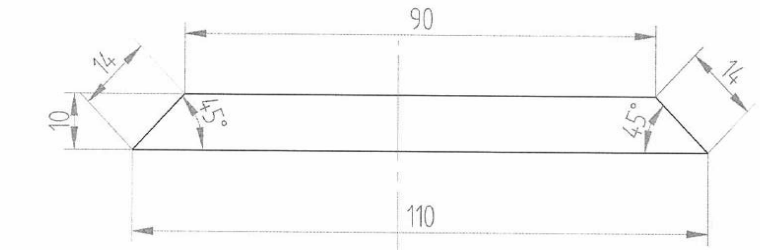

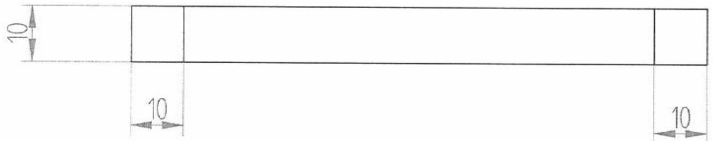

	NAME	DATE
DRAWN	[illegible]	[illegible]
CHECKED		
ENG APPR.		
MFG APPR.		

UNLESS OTHERWISE SPECIFIED
DIMENSIONS ARE IN MILLIMETERS
ANGLES ±X.X°
2 PL ±.XX 3 PL ±.XXX

SOLID EDGE
UGS - The PLM Company

TITLE

SIZE A2 | DWG NO | REV

FILE NAME [illegible]

SCALE | WEIGHT | SHEET 1 OF 1

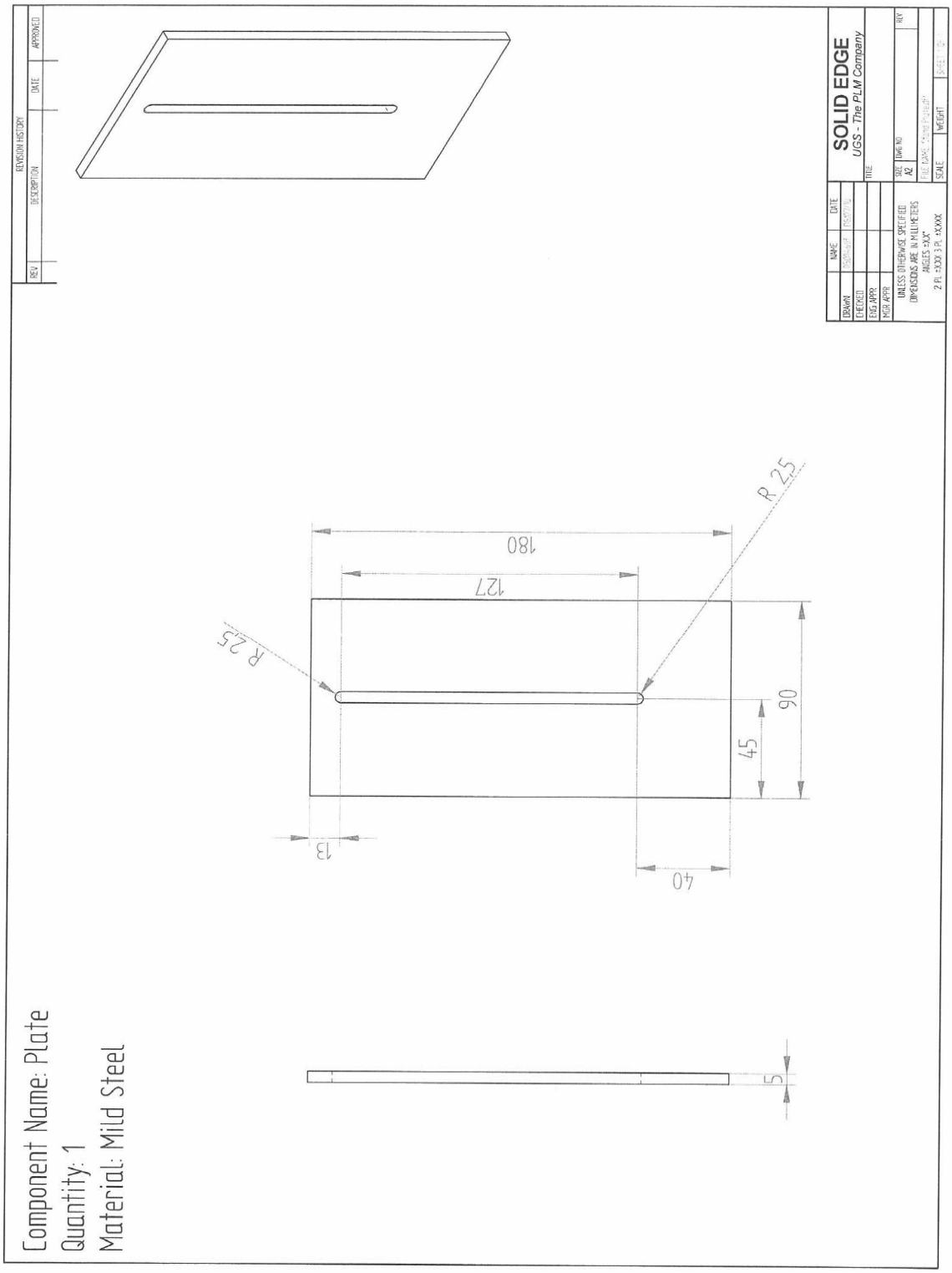
Component Name: Plate
Quantity: 1
Material: Mild Steel
180
127
R 25
R 25
90
45
13
40
5
SOLID EDGE
UGS - The PLM Company
UNLESS OTHERWISE SPECIFIED
DIMENSIONS ARE IN MILLIMETERS
ANGLES ±X.X°
2 PL ±XXX 3 PL ±X.XXX
REVISION HISTORY
REV
DESCRIPTION
DATE
APPROVED
DRAWN
CHECKED
ENG APPR
MGR APPR
NAME
DATE
TITLE
SIZE
A2
DWG NO
REV
SCALE
WEIGHT

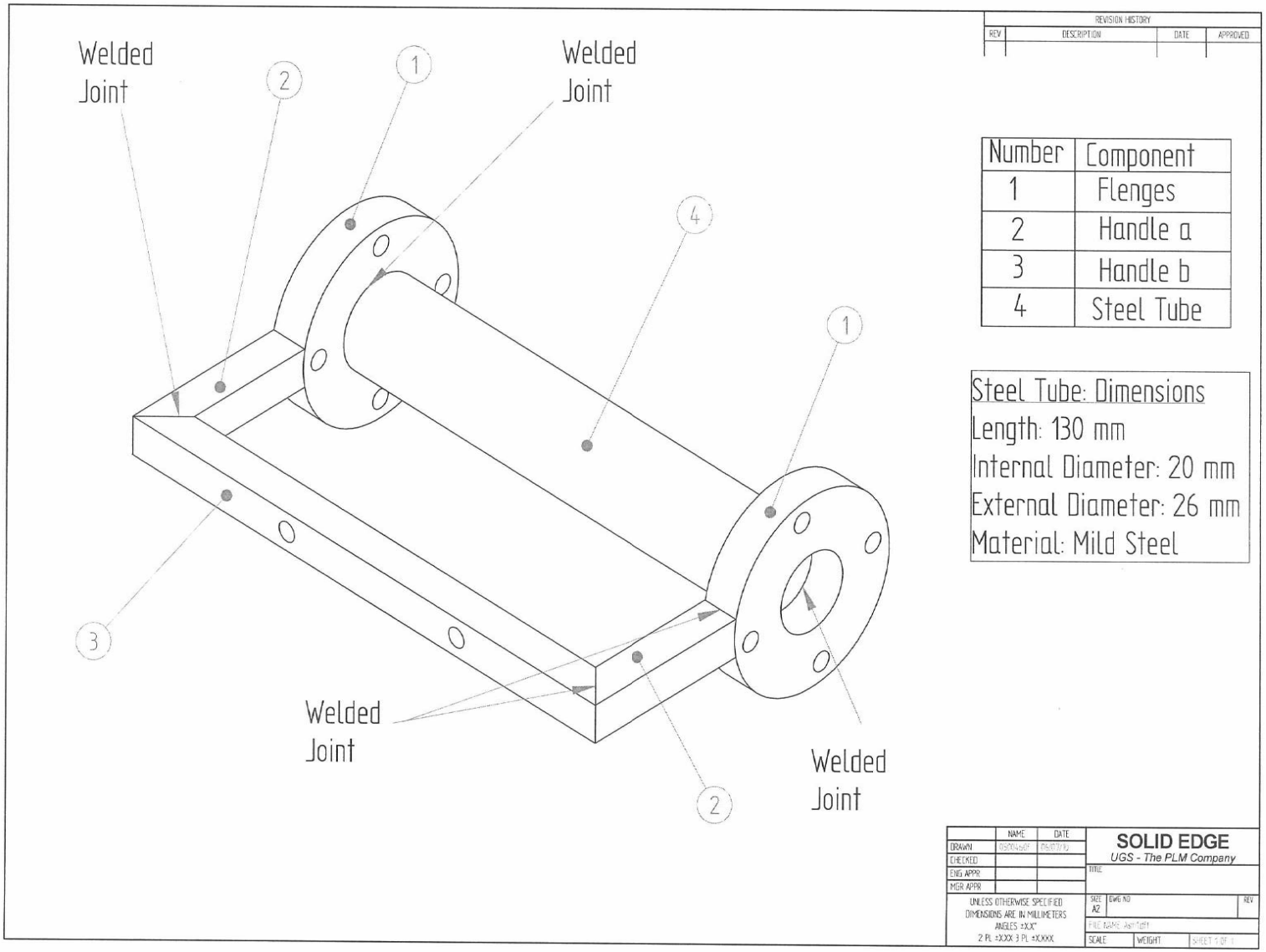
Welded Joint
Welded Joint
Welded Joint
Welded Joint
1
2
3
4
REVISION HISTORY
REV
DESCRIPTION
DATE
APPROVED
Number
Component
1
Flenges
2
Handle a
3
Handle b
4
Steel Tube
Steel Tube: Dimensions
Length: 130 mm
Internal Diameter: 20 mm
External Diameter: 26 mm
Material: Mild Steel
NAME
DATE
DRAWN
CHECKED
ENG APPR
MGR APPR
UNLESS OTHERWISE SPECIFIED
DIMENSIONS ARE IN MILLIMETERS
ANGLES ±X.X°
2 PL ±X.XX 3 PL ±X.XXX
SOLID EDGE
UGS - The PLM Company
TITLE
SIZE
A2
DWG NO
REV
SCALE
WEIGHT
SHEET 1 OF 1

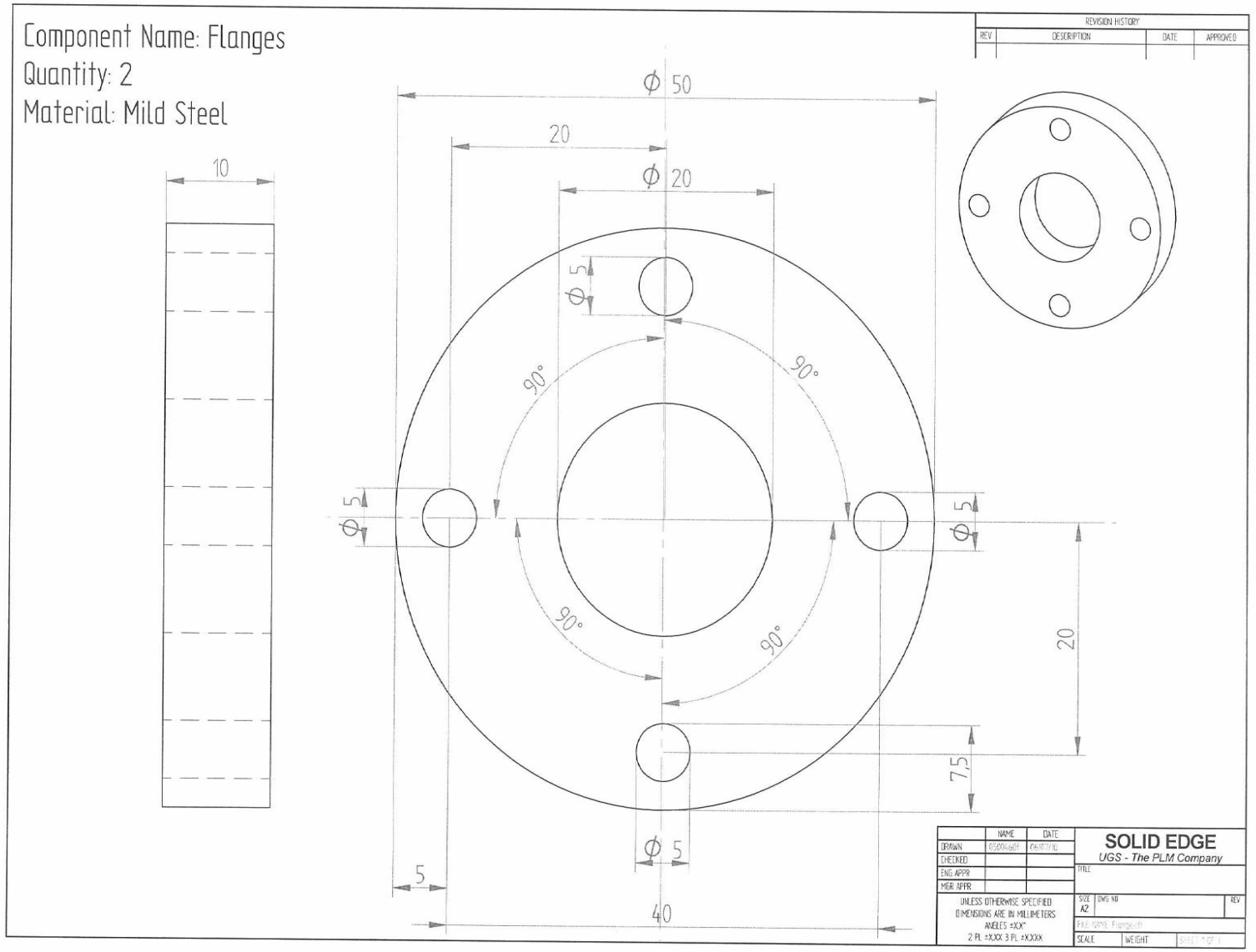
Component Name: Flanges
Quantity: 2
Material: Mild Steel
REVISION HISTORY
REV
DESCRIPTION
DATE
APPROVED
10
Φ 50
20
Φ 20
Φ 5
90°
90°
90°
90°
Φ 5
Φ 5
20
7,5
Φ 5
5
40
NAME
DATE
DRAWN
CHECKED
ENG APPR
MGR APPR
UNLESS OTHERWISE SPECIFIED
DIMENSIONS ARE IN MILLIMETERS
ANGLES ±XX°
2 PL ±XXX 3 PL ±XXXX
SOLID EDGE
UGS - The PLM Company
TITLE
SIZE
A2
DWG NO
REV
SCALE
WEIGHT

Component Name: Handle b
Quantity: 1
Material: Mild Steel

REVISION HISTORY			
REV.	DESCRIPTION	DATE	APPROVED

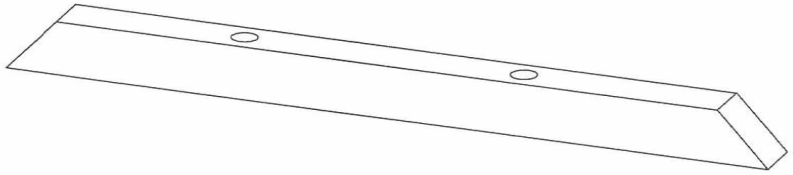

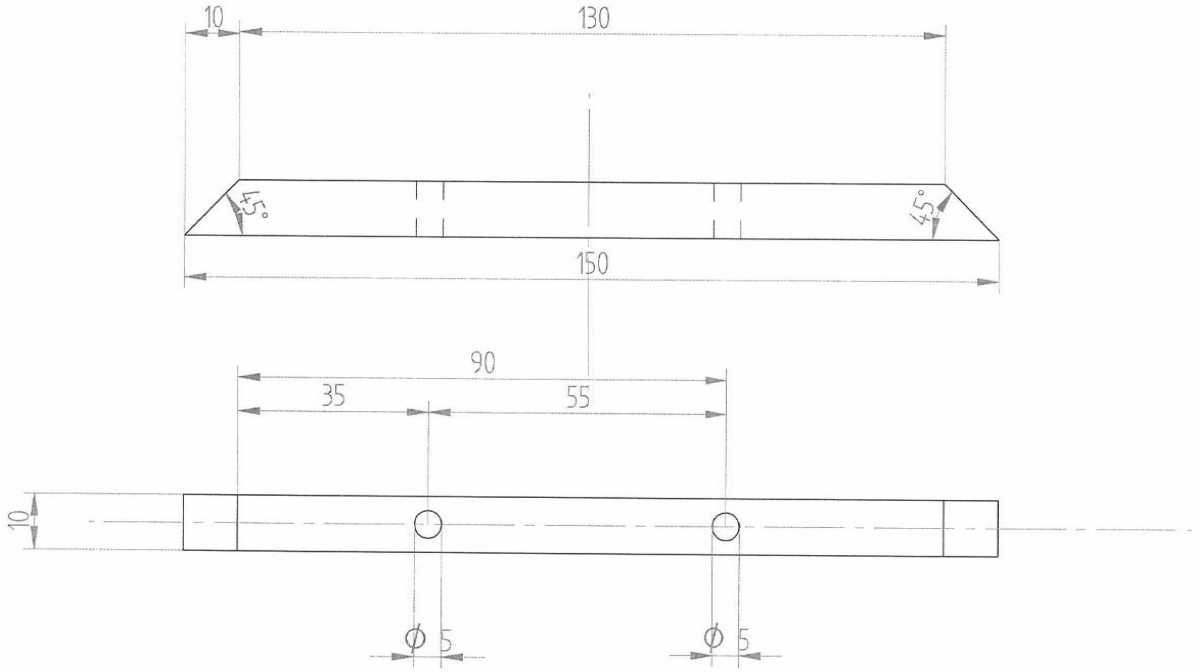

	NAME	DATE
DRAWN	[illegible]	[illegible]
CHECKED		
ENG APPR.		
MGR APPR.		

UNLESS OTHERWISE SPECIFIED
DIMENSIONS ARE IN MILLIMETERS
ANGLES ±X°
2 PL ±.XX 3 PL ±.XXX

SOLID EDGE
UGS - The PLM Company

TITLE

SIZE A2 | DWG NO | REV

FILE NAME: handle b.dft

SCALE | WEIGHT | SHEET 1 OF 1

Component Name: Handle a
Quantity: 2
Material: Mild Steel

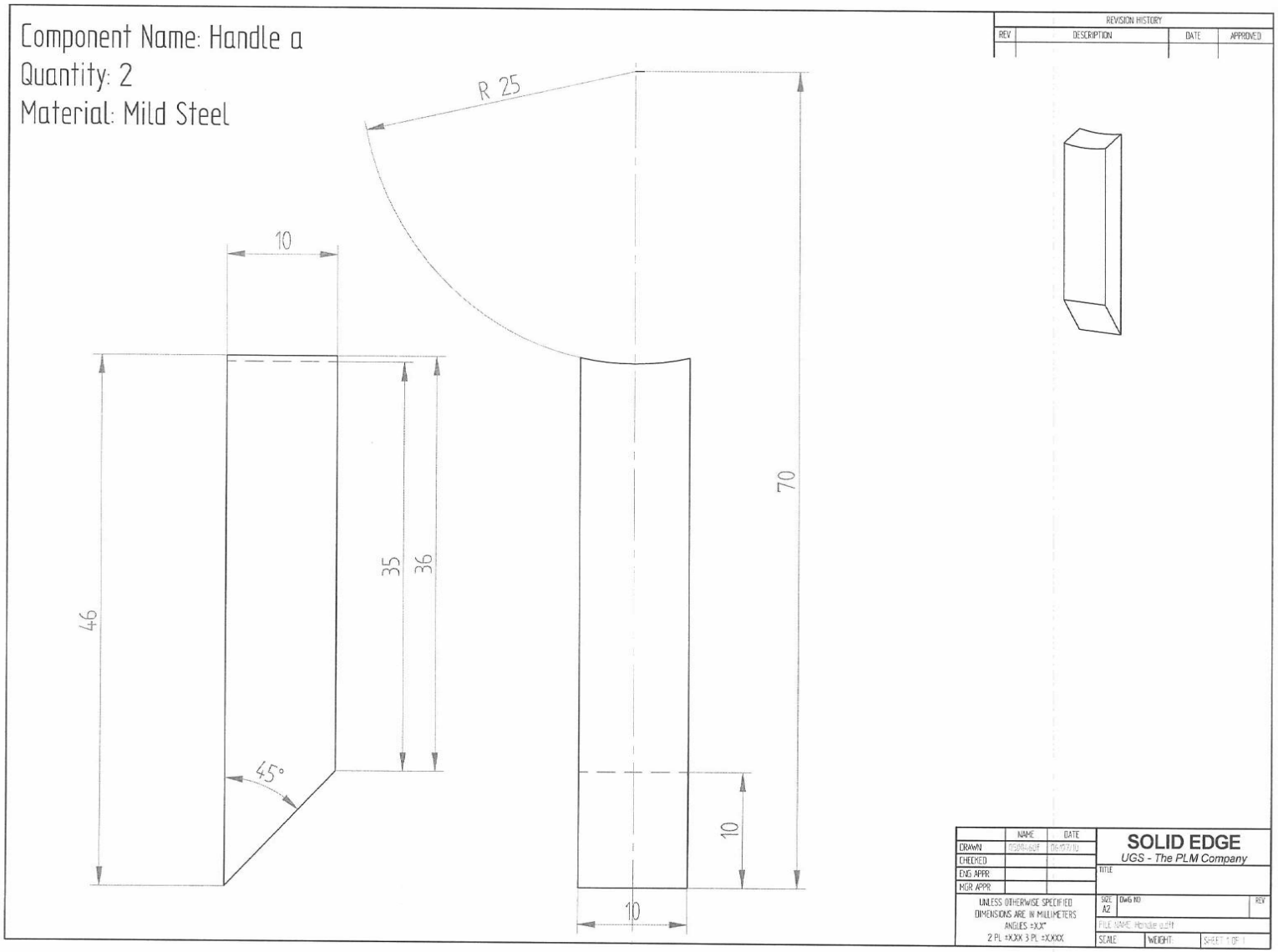

REVISION HISTORY			
REV	DESCRIPTION	DATE	APPROVED

	NAME	DATE
DRAWN		
CHECKED		
ENG APPR.		
MGR APPR.		

UNLESS OTHERWISE SPECIFIED
DIMENSIONS ARE IN MILLIMETERS
ANGLES ±X.X°
2 PL ±X.XX 3 PL ±X.XXX

SOLID EDGE
UGS - The PLM Company

TITLE

SIZE A2 | DWG NO | REV

SCALE | WEIGHT | SHEET 1 OF 1

APPENDIX B

7.3 Tables of Results

In this section the observations and results of tests on different valve arrangements and valve opening frequency changes are shown. These are the observations and results of both the experimental data and Kasimir simulations for Air and He as gas drivers.

7.3.1 Compression Wave and Flow Behind the Compression Wave Velocities

7.3.1.1 Single Valve Arrangement

The tables below show the change in shock and flow velocity behind the shock with change in reservoir pressure for a Single Valve Arrangement. B-C refers to the flow travelling duration between transducers B and C positioned 0.47m apart.

Table 4: Compression wave velocity with change in reservoir pressure: Air and He

	Air		Helium	
Reservoir pressure [Bar]	B - C Time [ms]	Compression Wave Velocity [m/s]	B - C Time [ms]	Shock velocity [m/s]
10	0.0025	188	0.00066	712.12
20	0.0019	247.37	0.00054	870.37
30	0.00085	552.94	0.0005	964.10
40	0.000775	606.45	0.00045	1044.44
50	0.00075	626.67	0.000425	1105.88

Table 5: Flow velocity behind the compression wave with change in reservoir pressure: air

Reservoir pressure [Bar]	Compression Wave Velocity	Mach Number	P_2	T_2	Flow Velocity
10	188	0.48	3.06	313.4	170.36
20	247.37	0.65	4.939	324.2	234.64
30	552.94	1.12	16.13	390.4	443.66
40	606.45	1.22	30.46	412.5	496.77
50	626.67	1.26	37.8	417.8	516.34

Table 6: Flow velocity behind the compression wave with change in reservoir pressure: He

Reservoir pressure [Bar]	Compression Wave Velocity	Mach Number	P_2	T_2	Flow Velocity
10	712.12	1.34	10	440.5	563.84
20	870.37	1.58	19.65	481.9	696.37
30	964.10	1.6	36.6	505.9	723.63
40	1044.44	1.81	71.38	526.1	832.33
50	1105.88	1.88	93.52	541.3	876.92

Table 7: Kasimir Flow Simulations for the shock velocity and flow velocity behind the shock: Air and He

	Air		Helium	
Reservoir pressure [Bar]	Shock Velocity [m/s]	Flow Velocity Behind Shock [m/s]	Shock Velocity [m/s]	Flow Velocity Behind Shock [m/s]
10	574.75	307.173	736.877	478.549
20	653.669	391.958	890.463	629.91
30	700.431	441.126	987.573	721.862
40	734.124	475.747	1059.162	788.355
50	760.477	502.421	1115.991	840.514

7.3.1.2 Double Valve Arrangement

The tables below show the change in compression and flow velocity behind the shock with change in reservoir pressure for the Double Valve Arrangement (Two stage diaphragms).

Table 8: Compression wave velocity change with change in reservoir pressure: Air and He

	Air		Helium	
Reservoir pressure [Bar]	B - C Time [ms]	Compression wave velocity [m/s]	B - C Time 1[ms]	Shock velocity [m/s]
10	0.004	117.50	0.0009	522.22
20	0.00305	154.10	0.0007	671.43
30	0.002	235.00	0.00065	723.08
40	0.0009	522.22	0.00054	870.37
50	0.0008	587.50	0.00049	959.18

Table 9: Flow velocity behind the shock change with change in reservoir pressure: air

Reservoir pressure [Bar]	Compression Wave Velocity	Mach Number	P_2	T_2	Flow Velocity
10	117.50	0.29	2.124	303.7	101.32
20	154.10	0.42	4.893	308.3	147.85
30	235.00	0.58	6.56	329.8	211.17
40	522.22	1.17	19.17	390.2	463.35
50	587.50	1.23	30.38	407.4	497.7

Table 10: Flow velocity change with change in reservoir pressure: He

Reservoir pressure [Bar]	Compression Wave Velocity	Mach Number	P_2	T_2	Flow Velocity
10	522.22	1.03	5.393	390.2	407.9
20	671.43	1.35	15.63	429.7	561.04
30	723.08	1.43	20.27	443.4	603.69
40	870.37	1.64	38.83	481.2	721.25
50	959.18	1.75	54.04	505.7	788.98

Table 11: Kasimir Flow Simulations for the shock velocity and flow velocity behind the shock: Air and He

Reservoir pressure [Bar]	**Air**		**Helium**	
	Shock Velocity	Flow Velocity	Shock Velocity	Flow Velocity
10	563.35	292.201	558.306	330.013
20	695.642	436.154	727.68	414..337
30	756.008	451.815	789.772	575.353
40	865.274	523.166	880.85	620.876
50	945.49	576.901	969.175	704.612

7.3.1.3 Effect of Valve Frequency Change on Jet Velocity: single Valve

The table below shows the flow behind the shock velocities with the change in pressure for 5, 10 and 20 Hz pulsating frequencies. Undefined wave structures were obtained for a frequency of 20 Hz with air as a driver.

Table 12: Flow velocity with change in pressure and frequency

Reservoir Pressure [Bar]	Theoretical Jet Velocity		5 Hz Frequency		10 Hz Frequency		20 Hz Frequency	
	Air	Helium	Air	Helium	Air	Helium	Air	Helium
10	307.173	478.549	170.36	563.84	144.1	578.36	-	-
20	391.958	629.91	234.64	696.37	222.98	688.02	-	738.25
30	441.126	721.862	443.66	723.63	250.1	779.2	-	757.47
40	475.747	788.355	496.77	832.33	292.3	836.9	-	832.33
50	502.421	840.514	516.34	876.92	312.03	869.7	-	870.64

7.3.2 Change in Jet Impact Velocity with Change in Pressure

The tables below show the jet flow velocity at impact on the substrate positioned 30mm away from the exit of the gun. The velocities are obtained by measuring stagnation pleasures at the position of the substrate.

7.3.2.1 Single Valve Arrangement

Table 13: Flow impact velocity on substrate downstream of gun exit: Air

Reservoir pressure [Bar]	Voltage[V]	P_0 [kPa]	$\frac{P_0}{P}$	M	$\frac{T_2}{T_1}$	**Impact Velocity**
10	0.3225	1.188	1.188	0.5	-	172.75
20	0.45	137.64	1.658	0.88	-	304.05
30	0.525	160.58	1.935	1.02	1.0132	354.74
40	0.625	191.2	2.3	1.16	1.1029	420.91
50	0.68	208	2.5	1.22	1.1405	442.52

Table 14: Flow impact velocity on substrate downstream of gun exit: He

Reservoir pressure [Bar]	Voltage[V]	P_0 [kPa]	$\frac{P_0}{P}$	M	$\frac{T_2}{T_1}$	**Impact Velocity**
10	0.3225	98.65	1.189	0.5	-	172.75
20	0.44	134.59	1.62	0.86	-	297.09
30	0.535	163.64	1.972	1.03	1.0198	359.38
40	0.73	223.29	2.69	1.28	1.1783	480.06
50	0.82	250.82	3.022	1.36	1.229	520.92

7.3.2.2 Double Valve Arrangement

Table 15: Flow impact velocity on substrate downstream of gun exit: Air

Reservoir pressure [Bar]	Voltage[V]	P_0 [kPa]	$\frac{P_0}{P}$	M	$\frac{T_2}{T_1}$	Impact Velocity
10	0.29	88.7	1.07	0.31	-	105.31
20	0.405	123.88	1.493	0.77	-	266.04
30	0.455	139.17	1.677	0.89	-	307.5
40	0.565	172.82	2.082	1.08	1.0522	382.76
50	0.69	211	2.543	1.24	1.1531	460.06

Table 16: Flow impact velocity on substrate downstream of gun exit: He

Reservoir pressure [Bar]	Voltage[V]	P_0 [kPa]	$\frac{P_0}{P}$	M	$\frac{T_2}{T_1}$	Impact Velocity
10	0.3	91.76	1.106	0.38	-	131.29
20	0.505	154.47	1.86	0.98	-	338.59
30	0.55	168.23	2.027	1.06	1.10393	384.73
40	0.66	201.88	2.43	1.2	1.128	440.35
50	0.73	223.29	2.69	1.28	1.178	480

7.3.3 Impact Velocity Change with Change in Pressure and Frequency

The tables below show the impact velocity as shown in tables 20 and 21 above. Tables 20 and 21 show impact velocities for 5Hz and the tables below show the impact velocities for 10 and 20 Hz frequencies for the single valve arrangement.

Table 17: Flow impact velocity on substrate downstream of gun exit pulsating at 10 Hz: Air

Reservoir pressure [Bar]	Voltage[V]	P_0 [kPa]	$\frac{P_0}{P}$	$\frac{T_2}{T_1}$	M	Impact Velocity
10	0.31	94.82	1.15	n/a	0.45	166.7
20	0.4	122.35	1.47	n/a	0.76	262.59
30	0.48	146.82	1.7689	1.1767	0.94	352.3
40	0.51	156	1.88	1.196	0.99	374.08
50	0.64	1.95.76	2.36	1.2785	1.18	461

Table 18: Flow impact velocity on substrate downstream of gun exit pulsating at 10 Hz: He

Reservoir pressure [Bar]	Voltage[V]	P_0 [kPa]	$\frac{P_0}{P}$	$\frac{T_2}{T_1}$	M	Impact Velocity
10	0.34	104	1.25	1.0673	0.58	200.36
20	0.44	134.59	1.62	1.1479	0.86	318.35
30	0.55	168.23	2.027	1.2247	1.06	405.3
40	0.75	229.4	2.764	1.338	1.3	519.6
50	0.825	252.35	3.04	1.3754	1.37	555.13

Table 19: Flow impact velocity on substrate downstream of gun exit pulsating at 20 Hz: He

Reservoir pressure [Bar]	Voltage [V]	P_0 [kPa]	$\frac{P_0}{P}$	$\frac{T_2}{T_1}$	M	Impact Velocity
10	Complex flow					
20	0.46	140.7	1.695	1.162	0.9	335.2
30	0.56	171.29	2.064	1.229	1.07	409.84
40	0.73	223.29	2.69	1.3277	1.28	509.58
50	0.82	250.82	3.022	1.3693	1.36	549.87

Table 20: Summarized impact velocities table for the 5, 10 and 20 Hz frequencies

Reservoir pressure [Bar]	5 Hz-Velocity		10 Hz-velocity		20 Hz-velocity	
	Air	Helium	Air	Helium	Air	Helium
10.00	172.75	172.75	166.7	200.36	Undefined waves	Undefined waves
20.00	304.05	297.09	262.59	318.35	Undefined waves	335.2
30.00	354.74	359.38	352.3	405.3	Undefined waves	409.84
40.00	420.91	480.06	374.08	519.6	Undefined waves	509.58
50.00	442.52	520.92	461	555.13	Undefined waves	549.87

7.3.4 Change in Down Stream Static Pressure with Change in Reservoir Pressure

The two transducers located downstream of the solenoid valves where also used to keep track of change in static pressure. Transducer B is located 250mm downstream of the second solenoid valve and transducer C is located 720mm downstream of the second solenoid valve. The two tables below show static pressure changes with change in reservoir pressure for the single arrangement.

Table 21: Transducer B static pressure traces

Reservoir pressure [Bar]	Air			Helium		
	Transducer Voltage[V]	Static pressure [psi]	Static pressure [Bar]	Transducer Voltage[V]	Static pressure [psi]	Static pressure [Bar]
10	0.173	34.53	2.38	0.245	48.90	3.37
20	0.4765	95.11	6.55	0.342	68.26	4.70
30	0.5325	106.29	7.32	0.525	104.79	7.22
40	0.805	160.68	11.06	0.875	174.65	12.03
50	1.035	206.59	14.23	1.035	206.59	14.23

Table 22: Transducer C static pressure traces

Reservoir pressure [Bar]	Air			Helium		
	Transducer Voltage[V]	Static pressure [psi]	Static pressure [Bar]	Transducer Voltage[V]	Static pressure [psi]	Static pressure [Bar]
10	0.1142	23.12	1.60	0.122	24.70	1.70
20	0.304	61.54	4.25	0.184	37.25	2.57
30	0.3625	73.38	5.07	0.297	60.12	4.15
40	0.555	112.35	7.76	0.52	105.26	7.27
50	0.73	147.77	10.20	0.62	125.51	8.66

7.3.5 Driver Gas Pre-heating

Kasimir simulations were run with different gas pre-heat temperature, room temperature velocities were compared to a preheat temperatures of 200 ^{o}C and 400 ^{o}C. The pre-heat tests were done for both the single and double valve arrangement.

Table 23: Gas pre-heat velocities for the single valve arrangement

Reservoir pressure [Bar]	Air – Velocities [*m/s*]			Helium – Velocities [*m/s*]		
	25 ^{o}C Room temperature	200 ^{o}C Pre-heat temperature	400 ^{o}C Pre-heat temperature	25 ^{o}C Room temperature	200 ^{o}C Pre-heat temperature	400 ^{o}C Pre-heat temperature
10	307.173	351.654	386.26	478.549	524.423	557.352
20	391.958	452.319	500.192	629.91	698.356	748.873
30	441.126	511.474	567.845	721.862	806.051	869.217
40	475.747	553.42	616.169	788.355	884.849	958.085
50	502.421	585.931	653.779	840.514	947.182	1028.852

Table 24: Gas pre-heat velocities for the double valve arrangement

Reservoir pressure [Bar]	**Air – Velocities [*m/s*]**			**Helium – Velocities [*m/s*]**		
	25 ^{o}C Room temperature	200 ^{o}C Pre-heat temperature	400 ^{o}C Pre-heat temperature	25 ^{o}C Room temperature	200 ^{o}C Pre-heat temperature	400 ^{o}C Pre-heat temperature
10	292.201	358.055	382.31	330.013	369.969	381.082
20	436.154	444.674	438.66	414..337	519.149	603.767
30	451.815	518.124	520.933	575.353	562.098	717.38
40	523.166	583.048	586.81	620.876	630.046	834.046
50	576.901	633.394	605.437	704.612	666.8	850.328

APPENDIX C

Components Specifications

Solenoid Valve :

Table 25: Solenoid valve specifications

Supplier's name:	Connexion Development Ltd
Maximum pressure:	1 to 200 Bar
Operating temperature:	-10°C to + 100°C
Orifice size:	6mm
Opening or Closing time:	100ms
Medium:	Air or Helium
Weight:	430 g
Voltage:	24V

Media: air – water – light oil
Pressure range: 1 to 200 bar max
Media temperature: 100° C max
Ambient temperature: -10° to +50°C
Media viscosity: 40 centistokes max
Mounting: vertical position, coil up
Weight (including coil): 430 g
Opening or Closing time: 100mSec Max

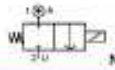

2/2 Brass
N/CLOSED

High Pressure 6mm Orifice
2 WAY SERVO ASSISTED

TYPE 206244



PRESSURE

Ø Port	Ø Orifice (mm)	Flow Rate Cv Ltr/ min	Pressure Rating (bar) Min ΔP	Max ΔP air	Max ΔP water - oil	Seals	Max Media Temp °C	Part Number	List Price
1/8 BSP or 1/4 BSP	6	5.0	1	100		NBR EPDM FKM	60 100 100	20624410 + port + voltage 20624430 + port + voltage 20624420 + port + voltage	£328.76
			1		100	NBR EPDM FKM	60 100 100	20624510 + port + voltage 20624530 + port + voltage 20624520 + port + voltage	
			1	200		NBR EPDM FKM	60 100 100	20624610 + port + voltage 20624630 + port + voltage 20624620 + port + voltage	£330.77
			1		200	NBR EPDM FKM	60 100 100	20624710 + port + voltage 20624730 + port + voltage 20624720 + port + voltage	

OPTIONS

Connector PG9 – DIN 43650 A	Included
IP65 Coil	Included
NPT thread	+£23.88
PTFE seal	+£22.55
Explosion proof enclosure: Protection II G/D EExdIICT6 ATEX	+£186.33

ELECTRICAL DATA

Voltage (-10% + 15%) Continuous duty 100%		Coil Size	Power Inrush	Power Holding	Insulation class	Enclosure	Electrical connections
~	24 - 48 - 110 - 230 (50 or 60 Hz)	40	48 VA	24 VA	F 155°C	IP 65 with connector	3 spades DIN 43650 DIN 40050 VDE 0110
⎓	12 - 24 - 48 (DC)		14 – 20 Watts				

CONSTRUCTION

Body: Brass
Tube and internal parts: Stainless steel
Seals and gaskets: NBR (Optional EPDM or FKM)
Moulded coil: Resin

REPAIR KIT

Coil	40 + voltage
Complete plunger + O' rings + piston	KIT + valve part number

OVERALL DIMENSIONS

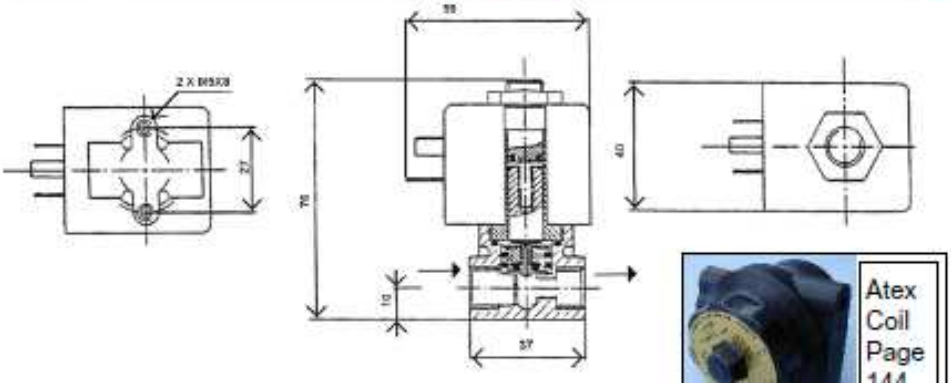

Atex Coil Page 144

Gas Cylinders:

Table 26: Helium cylinder specifications

Supplier's name:	Afrox
Available Helium pressure:	200 Bars
Specification	99.9999 to 100%
Volume	7.1 m^3
Cylinder Content Weight:	1.5 Kg

Table 27: Dry-air cylinder specifications

Specifications: Dry-Air Cylinder	
Supplier's name:	Afrox
Available air pressure:	100 Bars
Volume:	7.1 m^3
Cylinder Content Weight:	8.5 Kg

Pressure transducers:

Table 28: PCB Pressure transducer – Model 113A21

Supplier's name:	PCB Piezotronic
Measurement range:	1379 kPa
Operating temperature:	-72 to 135 ^0C
Maximum Flash Temperature:	1646 ^0C
Resonant Frequency:	500 kHz
Maximum Pressure:	6895 kPa
Weight:	6.0 gm

Table 29: PCB Pressure transducer – Model 113A23

Supplier's name:	PCB Piezotronic
Measurement range:	68 950 kPa
Operating temperature:	-73 to 135 ^0C
Maximum Flash Temperature:	1649 ^0C
Resonant Frequency:	500 kHz
Maximum Pressure:	103 420 kPa
Weight:	6.0 gm

Table 30: PCB Pressure transducer – Model 113A24

Supplier's name:	PCB Piezotronic
Measurement range:	6895 kPa
Operating temperature:	-73 to 135 ^0C
Maximum Flash Temperature:	1649 ^0C
Resonant Frequency:	500 kHz
Maximum Pressure:	68950 kPa
Weight:	6.0 gm

Controller:

Table 31: Moeller controller specifications

Supplier's name:	Moeller
Voltage supply:	24V DC
Analog output:	0 to 10 VDC/10 bits
Number of outputs:	8
Number of inputs:	4

APPENDIX D

Drag coefficients for different Reynolds numbers (Morsi et al, 1972)

$$C_D = \frac{24.0}{Re} \quad \text{for } Re < 0.1,$$

$$C_D = 3.69 + \frac{22.73}{Re} + \frac{0.0903}{Re^2} \quad \text{for } 0.1 < Re < 1,$$

$$C_D = 1.222 + \frac{29.1667}{Re} - \frac{3.8889}{Re^2} \quad \text{for } 1 < Re < 10.0,$$

$$C_D = 0.6167 + \frac{46.5}{Re} - \frac{116.67}{Re^2} \quad \text{for } 10.0 < Re < 100.0,$$

$$C_D = 0.3644 + \frac{98.33}{Re} - \frac{2778}{Re^2} \quad \text{for } 100.0 < Re < 1000.0,$$

$$C_D = 0.357 + \frac{148.62}{Re} - \frac{4.75 \times 10^4}{Re^2}$$
$$\text{for } 1000.0 < Re < 5000.0,$$

$$C_D = 0.46 - \frac{490.546}{Re} + \frac{57.87 \times 10^4}{Re^2}$$
$$\text{for } 5000.0 < Re < 10000.0,$$

$$C_D = 0.5191 - \frac{1662.5}{Re} + \frac{5.4167 \times 10^6}{Re^2}$$
$$\text{for } 10000.0 < Re < 50000.0.$$

APPENDIX E

Solenoid Valve Types

Tube pinch solenoid valve

The tube pinch solenoid valve is the only full bore flow (with no idle space) solenoid of the listed valves. The tube pinch valve provides a streamlined flow, with a high coefficient of flow; however it is limited by the fact that it has very low pressure limits and a low shut-off capability (ASCO, 2009). Therefore, this valve could not be suitable for a shock tube application, since very high pressures are involved.

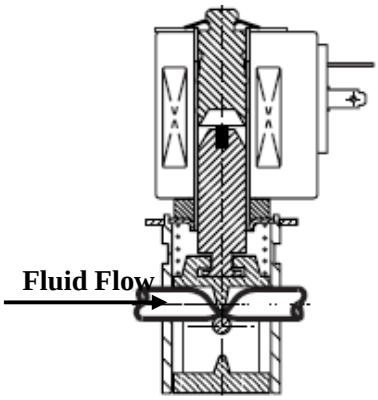

Figure 61: Sectioned view of the Tube pinch solenoid valve

Diaphragm type solenoid valve

Diaphragm valves are related to pinch valves, but they are not full bore flow. The valves have a limited idle volume. Instead of pinching the liner closed to provide shut-off, the diaphragm is pushed into contact with the bottom of the valve body. The diaphragm valves provide a very clean flow and tight shut-off. However, the valve has a very low pressure and temperature limits, and multi-turn operation limitations (ASCO, 2009).

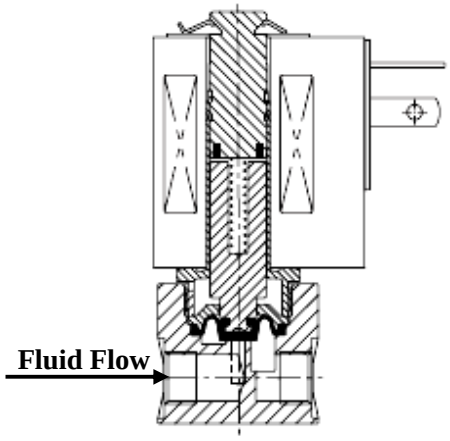

Figure 62: Sectioned view of the diaphragm solenoid valve

Direct operated 2/2 solenoid valves

The 2/2 direct operated valve is the most commonly used valve and one that is readily available. In this valve the core is mechanically connected to the disc and opens or closes the orifice, depending on whether the solenoid coil is energized or de-energized (ASCO, 2009). These types of valves can handle very high pressures compared to others and have a very fast response time which is required to generate strong shock waves. However, the valve is not a free bore flow and has an idle volume.

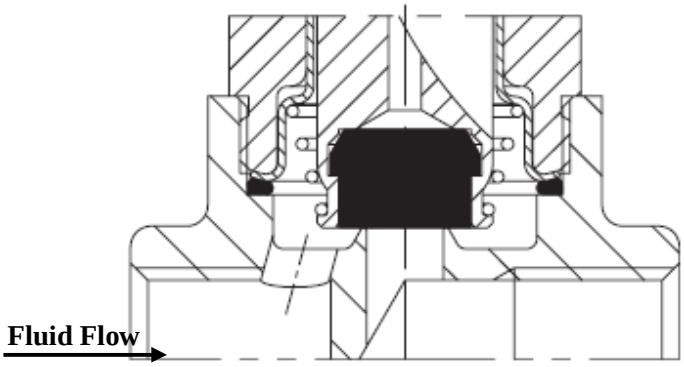

Figure 63: Sectioned view of the direct operated solenoid valve

Lever type solenoid valves

Lever type solenoid valves are designed for high differential pressures and flow rates. Heat dissipation for the electromagnetic part is optimized by separating the control system from

the valve itself (ASCO, 2009). These valves are ideally suited for high ambient temperatures. The valve is also not a free bore flow and has a huge idle volume.

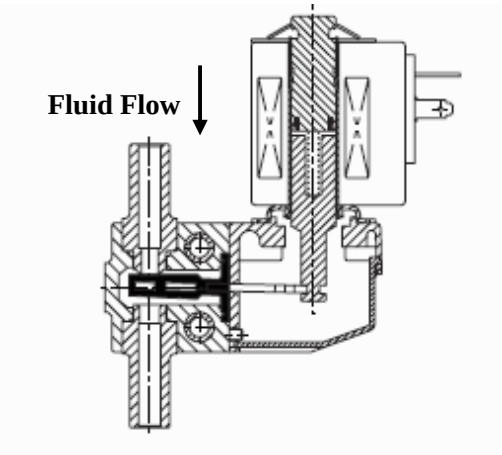

Figure 64: Sectioned view of the lever type solenoid valve

APPENDIX F

Wave Diagrams from Kasimir Simulations

The figures below show wave diagrams for both helium and air at 10, 20 and 30 bars of reservoir pressure.

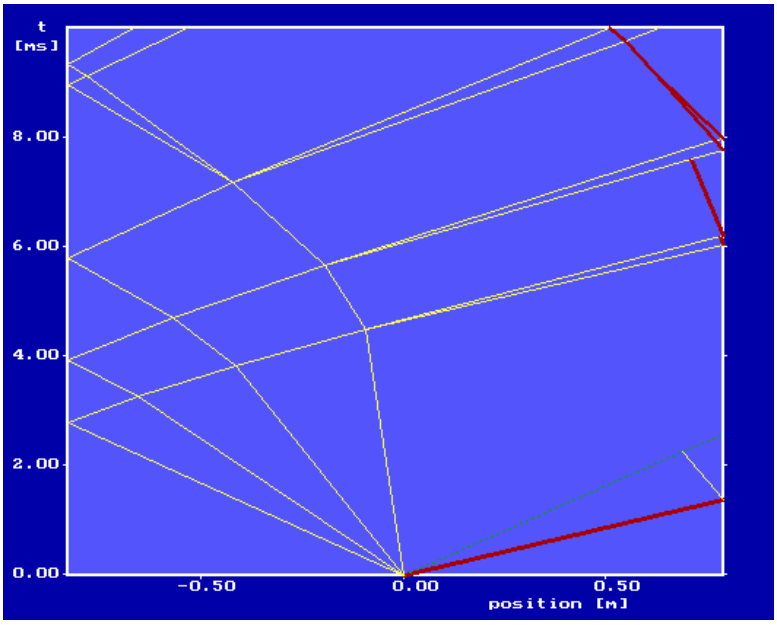

Figure 65: 10 bar reservoir pressure with air as the gas driver

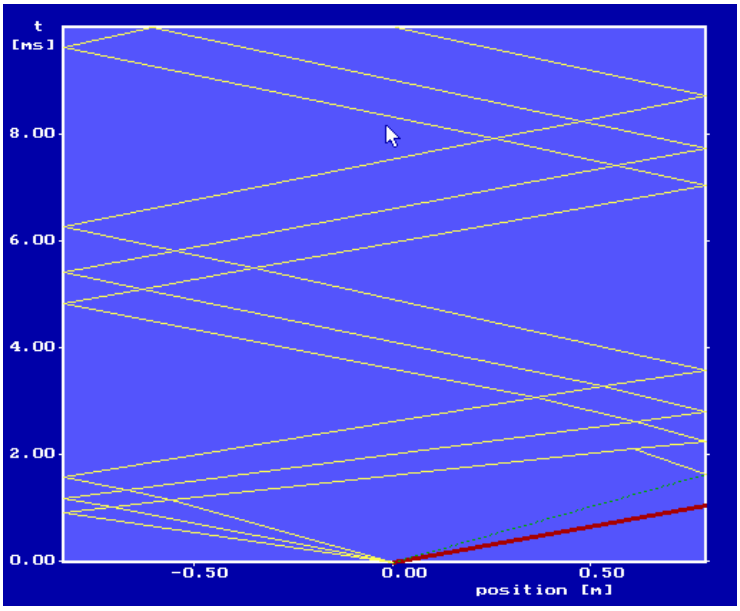

Figure 66: 10 bar reservoir pressure with helium as the gas driver

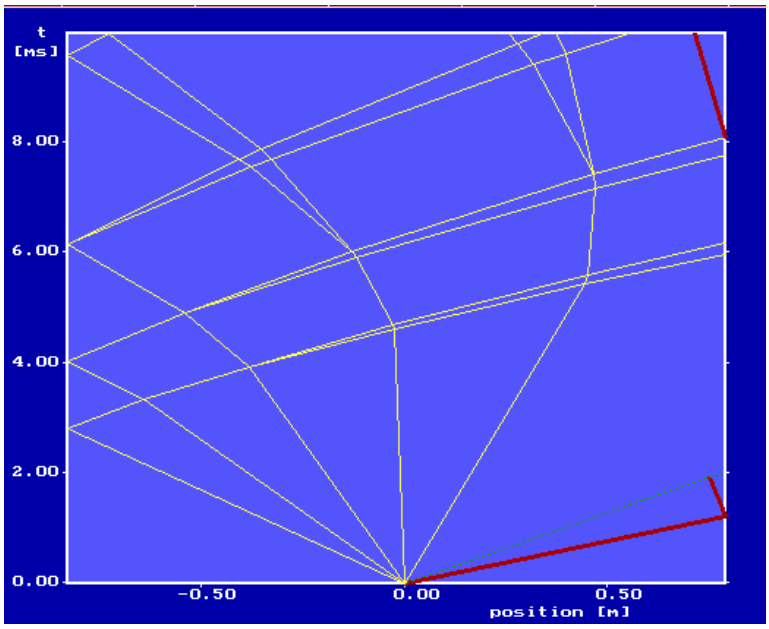

Figure 67: 20 bar reservoir pressure with air as the gas driver

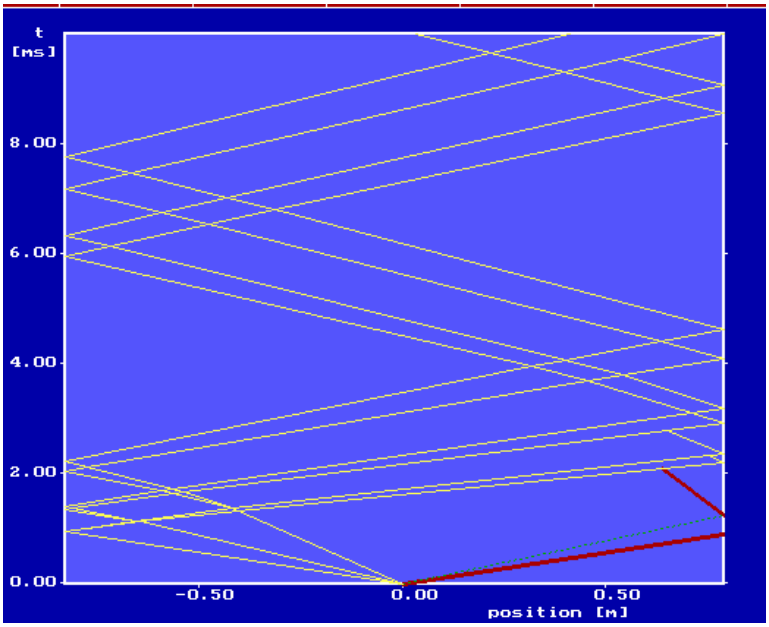

Figure 68: 20 bar reservoir pressure with helium as the gas driver

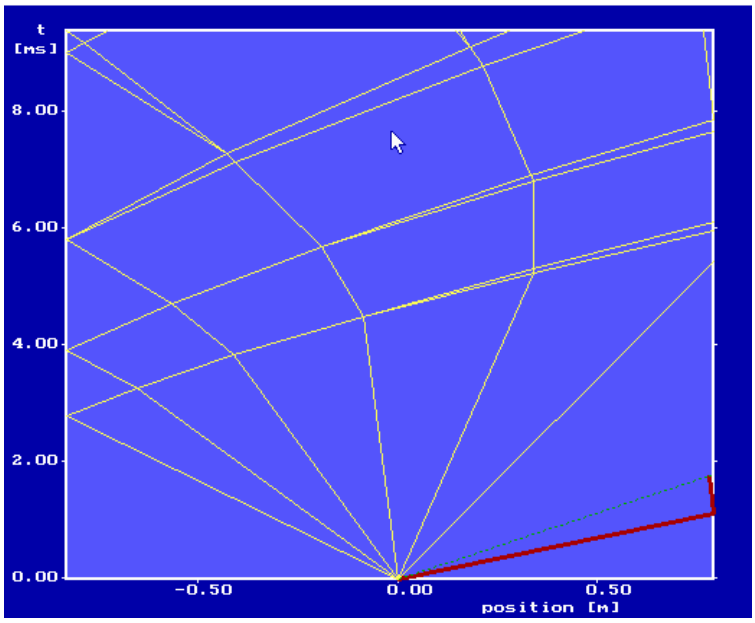

Figure 69: 30 bar reservoir pressure with air as the gas driver

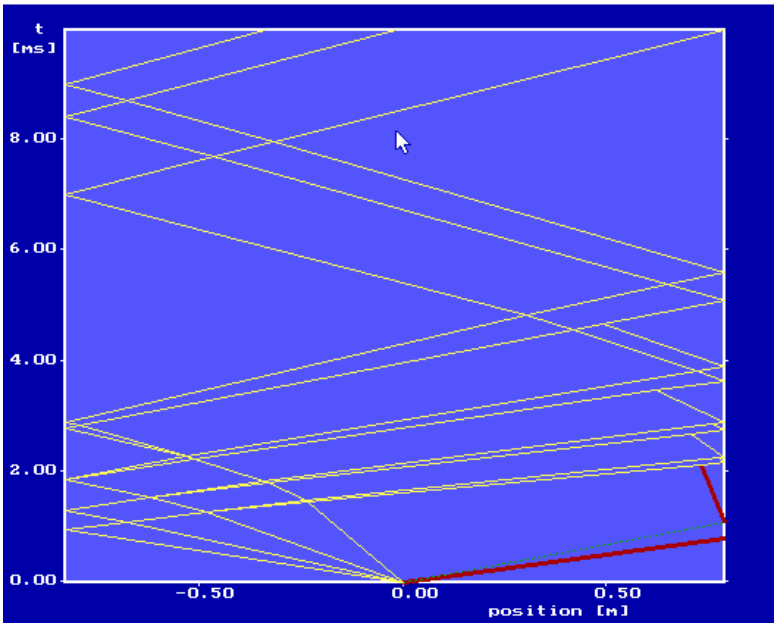

Figure 70: 30 bar reservoir pressure with air as the gas driver

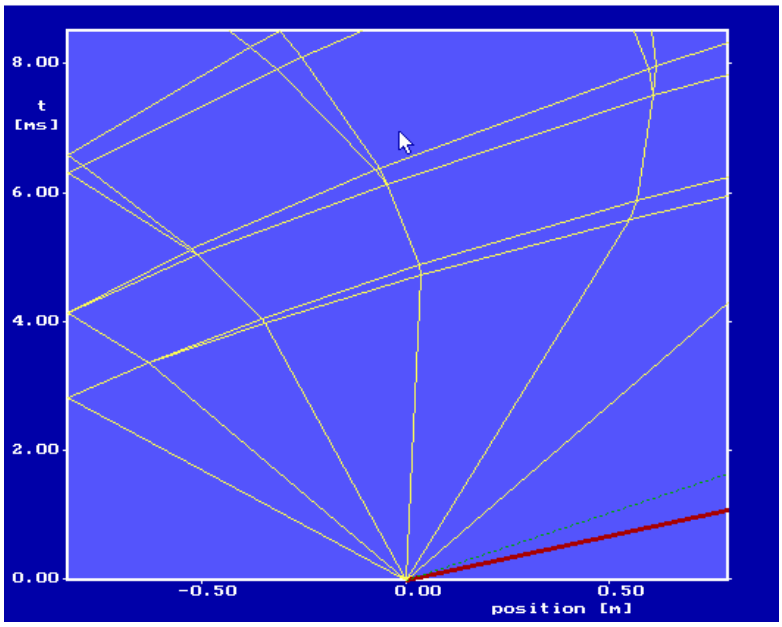

Figure 71: 40 bar reservoir pressure with air as the gas driver

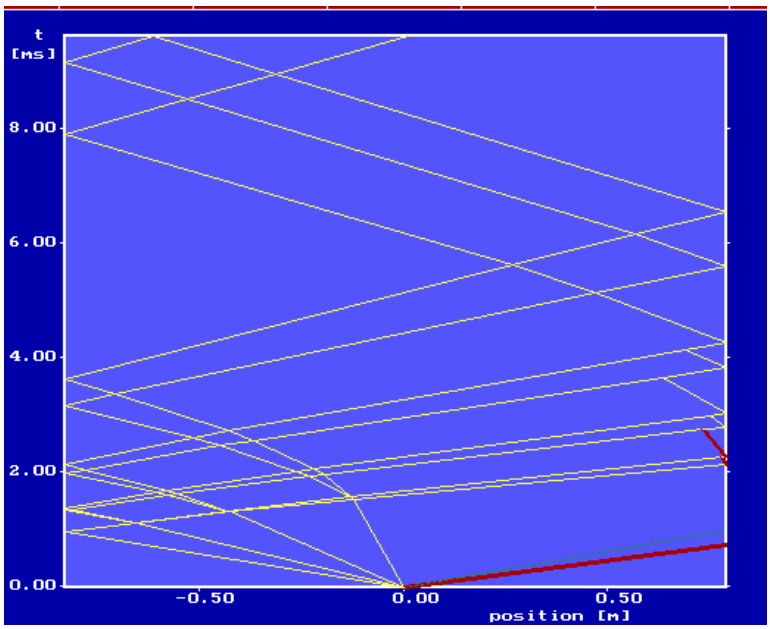

Figure 72: 40 bar reservoir pressure with helium as the gas driver

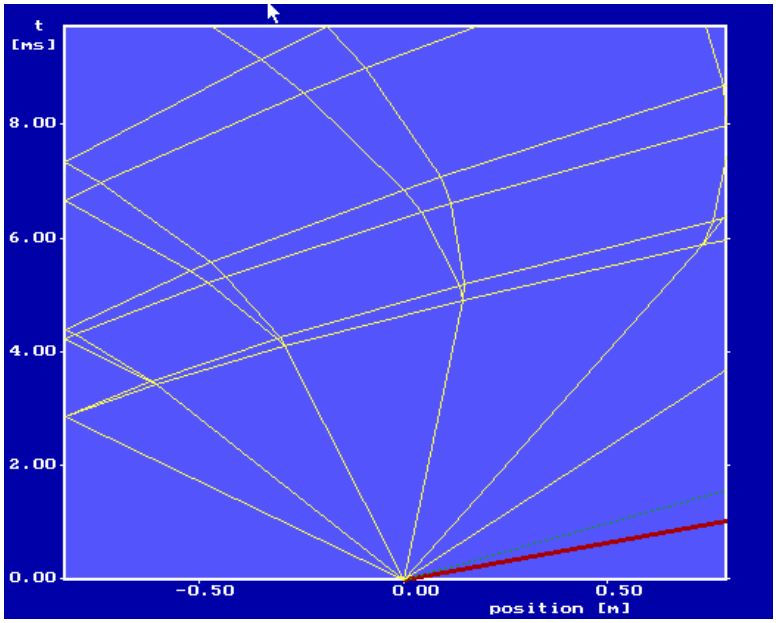

Figure 73: 50 bar reservoir pressure with air as the gas driver

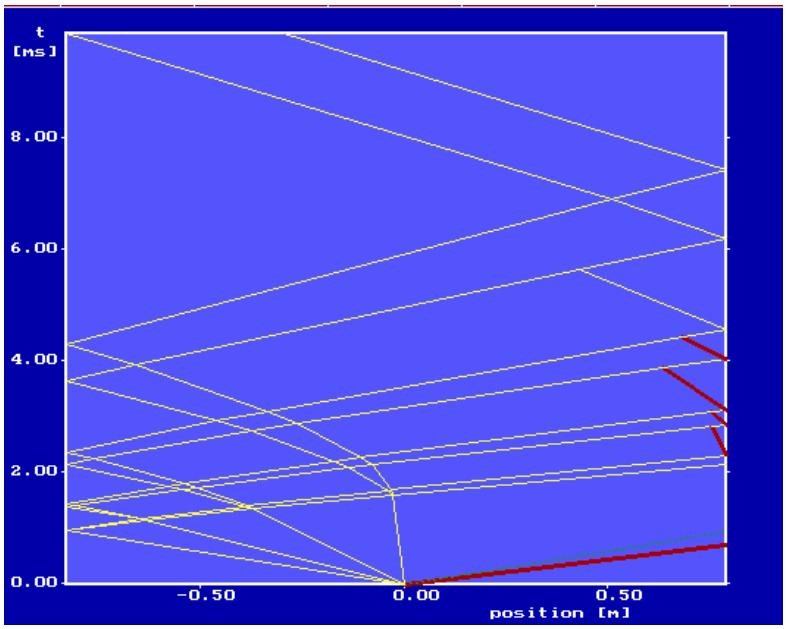

Figure 74: 50 bar reservoir pressure with helium as the gas driver

Appendix G

Validation of the shock tube length selection

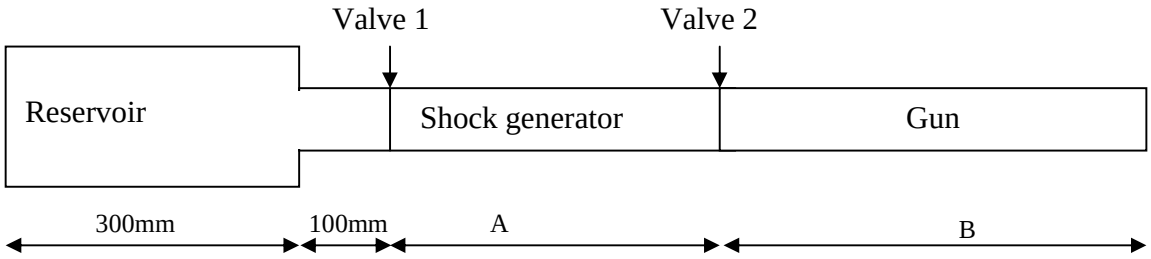

In the length simulation the reservoir size is kept constant, the shock generator and gun diameters are also kept constant at 5mm. Different shock generator and gun lengths are simulated and the shock exit velocities as well as the flow velocities behind the shock wave were compared.

The tests are performed for a single valve arrangement where valve 1 is kept constantly opened and valve 2 is opened and closed (acting as a diaphragm) to generate shock waves. All the simulations were run at a constant reservoir pressure of 30 bar, with helium as the gas driver at a temperature of 294K.

The simulation results are shown in figures 75 to 80 below, and a summary of results is shown in table 32. Six different cases were simulated, and the results show a shock wave to be formed in all the cases. The shock wave velocity is not affected by the length of the tube within the tested range. This can be attributed to the fact that in the simulation program the diaphragm ruptures instantly and shock waves get formed over a very short length. In a case where solenoid valves are used as diaphragms it will take slightly longer (longer length tube) for a shock wave to be generated, and the lower cases (smaller length tubes) might not suffice. It is also necessary to create enough space (enough tube length) to allow for pressure transducer attachments on various points on the rig. On the other hand the shock tube should not be made too long unnecessarily. Due to the above mentioned reasons the shock tube dimensions in case D was selected.

Table 32: Simulation results summary

	Shock generator length (A) m	Gun length (B) m	Shock exit velocity	Flow behind the shock velocity at exit
Case A	0.05	0.15	982.572	718.207
Case B	0.1	0.25	982.572	718.207
Case C	0.2	0.5	982.572	718.207
Case D	0.35	0.75	982.572	718.207
Case E	0.5	1	982.572	718.207
Case F	0.75	1.5	982.572	718.207

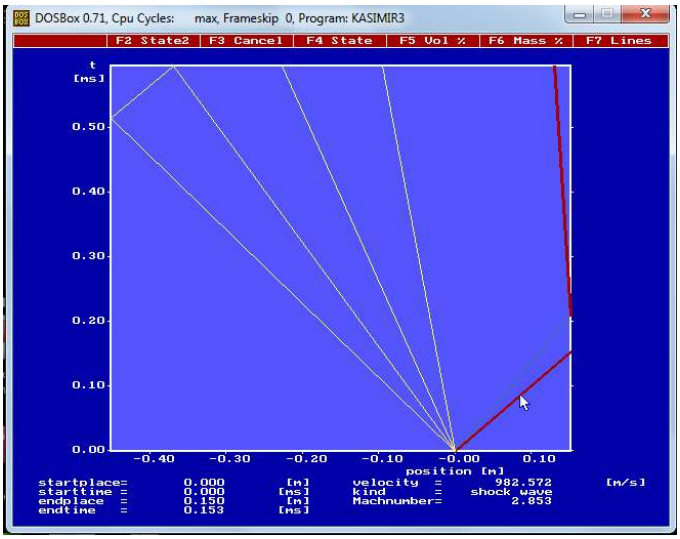

Figure 75: Case A Shock wave diagram

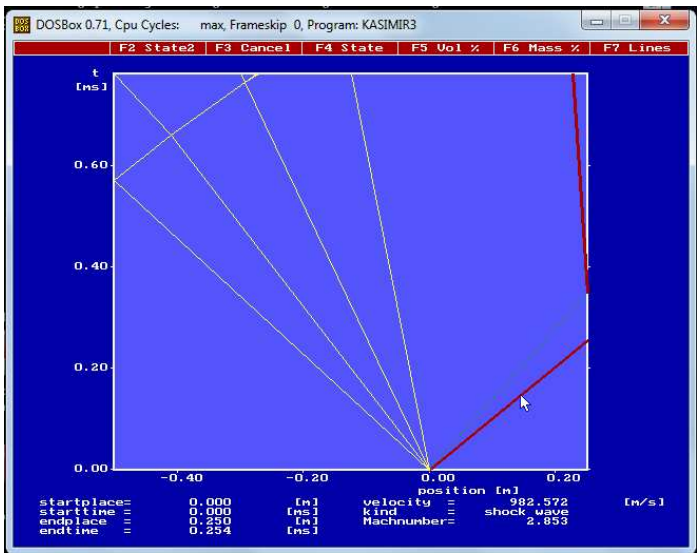

Figure 76: Case B Shock wave diagram

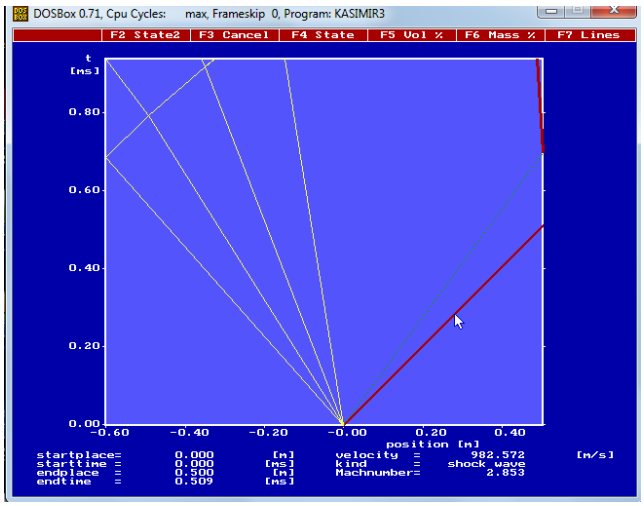

Figure 77: Case C Shock wave diagram

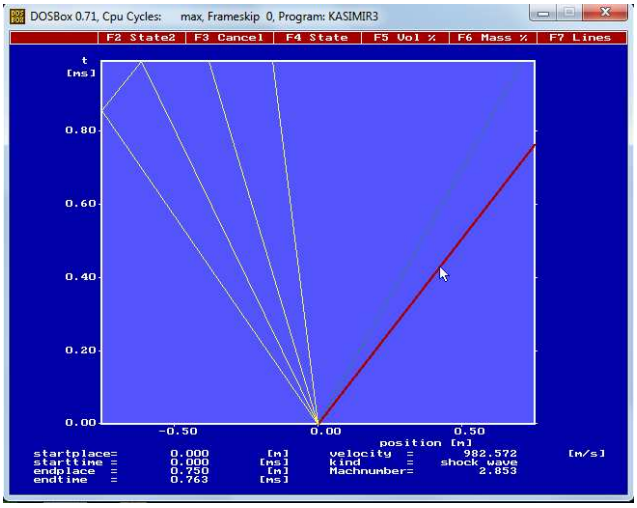

Figure 78: Case D Shock wave diagram

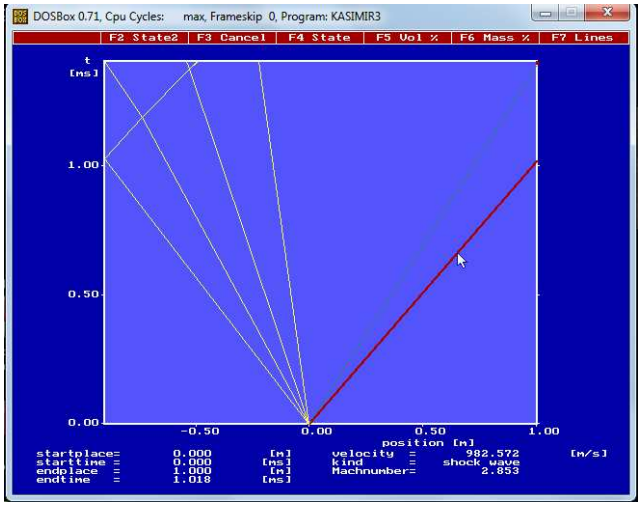

Figure 79: Case E Shock wave diagram

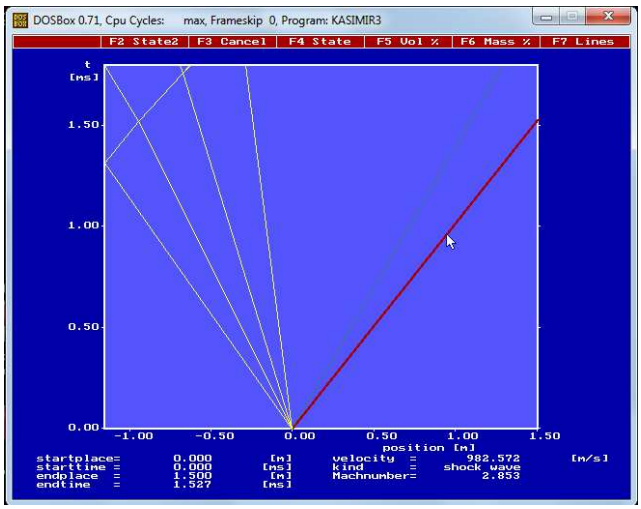

Figure 80: Case F Shock wave diagram